A MULTIPLE-VIEW VISUAL STUDY OF THE INNER/OUTER REGION INTERACTIONS OF COHERENT MOTIONS IN A TURBULENT BOUNDARY LAYER

By

Kue Pan

A DISSERTATION

Submitted to
Michigan State University
in partial fulfillment of the requirements
for the degree of

DOCTOR OF PHILOSOPHY

Department of Mechanical Engineering

1992

ABSTRACT

A MULTIPLE-VIEW VISUAL STUDY OF THE INNER/OUTER REGION INTERACTIONS OF COHERENT MOTIONS IN A TURBULENT BOUNDARY LAYER

By

Kue Pan

A time resolved multiple-view laser sheet and multiple location, multicolor dye injection flow visualization technique has been used to observe the interactions between sublayer motions and the coherent motions above the wall in a turbulent flat-plate flow at $R_\theta \approx 805$. Pairs of low-speed streaks were observed to form and evolve underneath passing typical eddies in the log region and lower portion of the outer region. The pairs of streaks were also found to be associated with the formation of a pocket between the streaks near their downstream end. Statistical characteristics of the observed coherent features and their interactions are presented. The streak pair spacing was found to be on average $l^+ \sim 75$. Observations in laser sheets perpendicular to the flow direction consistently showed counter-rotating vortex pairs. Because of the highly resolved temporal record and the complementary spatial information, it was determined that the streamwise extent of these pairs was similar to the length characteristic of the typical eddies. Thus, they were not long axial vortices, or stretched hairpin legs. Instead they were identified as typical eddies. This was confirmed both by the dye with which they were colored, which indicated they were not connected to the wall, and by visual identification in the side view laser sheet of the typical eddy pattern. Correlations of the concurrent occurrence of the typical eddies and the sublayer features, pockets and streak pairs, below them were examined. Results show that average sizes of these coherent motions are similar, and that the dimensions of both sublayer features increase as the spanwise diameter of the typical eddy increases. The sampling of low-speed streaks using a classical counting method was also performed to confirm the universal mean streak spacing. An argument utilizing the statistical results of the typical eddy spanwise distribution spacing and the streak pair spacing, enables one to recover the result that the overall streaky structure has a spacing of $\lambda^+ \sim 100$ at this Reynolds number. An overall picture of the inner/outer region interactions and the pinch-off phenomena of hairpin vortices at low Reynolds numbers is also presented.

To

My Parents

ACKNOWLEDGEMENTS

I would like to express my sincere gratitude to my wife, Linda, whose moral support and patience have carried me through difficult time when I was discouraged; without her this work could never have been completed.

I wish to thank Professor Robert E. Falco for his motivation, guidance, and advice for this experimental investigation. I also appreciate Drs. J. Foss, D. Yen, and M. Koochesfahani who reviewed the manuscript and provided many valuable comments. Additionally, I gratefully acknowledge my colleagues and friends S.-C. Yoo, J. Klewicki, S. Buchner, B. Slider, C. Olbrich, M. DeFilippis, M. Gieselmann, A. Folz, F. Cummings, T. Stuecken, and C. Gendrich for assistance and friendship they have provided. Finally, I must also thank the financial support of U.S. Air Force Office of Scientific Research under contract 87-0047.

TABLE OF CONTENTS

Page

CHAPTER

LIST OF TABLES

LIST OF FIGURES

FIGURE Page

Page

Page

Page

LIST OF SYMBOLS

$(\ )^+$	Quantity normalized by wall layer variables, ν/u_τ or ν/u_τ^2
$\overline{(\ )}$	Mean quantity
C_x	Streamwise length scale of typical eddy
C_y	Diameter of vortex core of typical eddy in y direction
C_z	Diameter (maximum dimension) of typical eddy in the y-z plane
c_f	Skin friction coefficient, $2\nu(\partial u / \partial y)_{wall} / U_\infty^2$
D	Diameter of ring vortex in the physical simulations
d	Distance of typical eddy center from the wall
d^*	Normalized distance, $d^+ - 0.5C_z^+$
F	Flatness (fourth central moment, i.e Kurtosis) coefficient, $\overline{(\ )^4}/\sigma^4$
g	Gravity, 32.2 ft/sec^2
H	Boundary layer shape factor, δ_d/θ
h	Pressure differential normal to the horizontal, $P_t - P_s = \ell \text{ Sin } \beta$
N	Number of samples
P	Probability density
P_s	Static pressure
P_t	Total pressure
Re_x	Reynolds number based on the streamwise distance from the tripping, $U_\infty x/\nu$
Re_y	Reynolds number based on the distance from the wall, $U_\infty y/\nu$
R_θ	Reynolds number based on momentum thickness, $U_\infty\theta/\nu$
r	Radius of typical eddy, equivalent to $C_z/2$

r_O	Initial radius of typical eddy as it is formed
S	Skewness (third central moment) coefficient, $\overline{(\ )^3}/\sigma^3$
s	Streamwise spacing between two measuring stations in surface float measurements, which is 4 feet
T	Temperature
t	Time
t_P	Period of occurrences of pockets
t_{TE}	Period of occurrences of typical eddies
Δt	Period of occurrences of correlated interaction events
U_∞	Free stream (surface) velocity
u,v,w	Velocity components in x, y, and z directions respectively
u_τ	Friction velocity, $\sqrt{\nu(\partial u / \partial y)_{wall}}$
v_{TE}	Vertical convection velocity of typical eddy
w	Spanwise dimension of pocket-like depression
x,y,z	Spatial coordinates
β	Angle between pressure tubes and the horizontal, which is 30 degrees
θ	Momentum thickness
ϕ	Angle between positive y axis and typical eddy axis in the y-z plane
l	Streak-pair spacing
ℓ	Pressure differential along the direction of pressure tubes
λ	Streak spacing
ξ	Center-to-center spacing between two neighboring typical eddies in spanwise direction
ψ	Coefficient of variation, $\sigma/\overline{(\ )}$
ν	Kinematic viscosity
ρ	Density
σ	Standard deviation

δ_{99}	Boundary layer thickness based upon 99% of free stream velocity
δ_d	Displacement thickness

CHAPTER 1

INTRODUCTION

1.1 Random Turbulence to Organized Turbulence

For many years a concept of turbulence had been accepted as random motions with no organized structural feature and therefore led to the exploration of its behavior predominantly by means of statistical approaches. During this period, most statistical properties of turbulence were obtained by using hot wires or other single-point alternatives, which were not capable of revealing the existence of organized flow motions owing to the high degree of variation in size, orientation, and occurrence of these three-dimensional motions. Over the past three decades, the aspects of turbulence have been reconsidered since experimental investigators such as Kline, Reynolds, Schraub, and Runstadler (1967), and Kovasznay, Kibens, and Blackwelder (1970) documented the existence of wall region streaky structures and large scale coherent motions (bulges) in turbulent boundary layers respectively. Although these investigations may have not been necessarily the first to discover the respective features, they are surely the ones who ignited the numerous subsequent studies concerning the structure of turbulent boundary layers. Since then, the objective of many research efforts have been focused upon finding the recognizable outer layer motions, wall region flow structures, as well as the correlations between outer layer and wall layer structural features. As a result, both large scale motions and inner region have been extensively studied. Various types of small to intermediate scale coherent structural elements have been observed or deduced.

However, the three-dimensional, unsteady, strongly varying convection velocity has made understanding the inner/outer region interaction a most difficult problem.

It is necessary to mention that the intent of this chapter is not to present a survey of contributions to the understanding of turbulent boundary layer structure. Nevertheless, the pieces of knowledge gained from an extensive review of the past literature, which provide an excellent background as well as motivation for the current study, will be briefly described, with particular emphasis on the wall region events and the motions associated with their occurrence. The phrase "wall region" used here is referred to as being the zone adjacent to the wall comprising viscous sublayer and the buffer region (i.e. $y^+<15$). The "inner region" ($y^+<70$) is roughly defined as the combination of the wall region and lower portion of the logarithmic region, whereas the "outer region" ($70\leq y^+<400$) is the region beyond the inner region and bounded by the mean edge of the boundary layer thickness.

It is also important to note here that turbulent boundary layers at low Reynolds numbers can be computed by direct numerical simulation (i.e. DNS). Kim, Moin, and Moser (1987) simulated a turbulent channel flow using unsteady Navier-Stokes equations and compared the computed results with experimental results at comparably low Reynolds numbers. It was found that the general characteristics of the computed turbulence statistics were in good agreement with the experimental results. However the detailed comparison revealed consistent discrepancies, particularly in the wall region. Computations by Moser and Moin (1984) and Spalart (1985) also resulted in similar problems. Zang (1991) pointed out that although current DNS of turbulent flows have been proven to be able to provide reliable long-time statistics, they may not adequately capture the instantaneous shapes and dynamics of turbulent structures even at low Reynolds number flows (also see Robinson, Kline, and Spalart 1989). Zang, Krist, and Hussaini (1989) presented evidence suggesting that reliable computational simulation of the near-wall turbulent structures required a considerably higher resolution level than those presently used for the high-fidelity DNS. A consequence of the present state of uncertainty is that experimental investigations are needed to provide both new structural information as well as a data base to check the accuracy of computed turbulent structures.

1.2 Important Coherent Structural Motions Recognized in the Wall Region of Turbulent Flows

Kline et al. (1967) observed the redistribution of a series of arrays of hydrogen-bubble markers into elongated streamwise oriented streaks, moving roughly one half of the local mean velocity, in the wall region of turbulent boundary flows. They proposed that these low-speed streaks were the signature feature of wall-bounded turbulent flows and that their spanwise characteristic spacing constituted an universal feature in the inner layer (also see Kim, Kline, and Reynolds 1971). Later, extended studies by Smith and Metzler (1983) characterized the low-speed streaks for a Reynolds-number range of $740 \leq R_\theta < 5830$. They concluded that the probability density function of the spanwise spacing was approximately a log-normal distribution (i.e. the logarithm of the streak spacing is normally distributed) with mean value of about 100 wall layer units and invariant with Reynolds number over the range studied. It was also noted that the streamwise extent of the streaks varied over a vast range, from 50 to greater than 2,000 wall layer units.

In a visual investigation of smoke contaminant turbulent boundary layers, Falco (1974) found an identifiable family of motions which occurred over both inner and outer regions. This family of motions was recognizable by their vortex-ring-like shapes and similar evolutions. He called them the "typical eddies" (also referenced as "compact vortical flow structures" or "Falco eddies" by some others). The diameter of the typical eddies was found to be of the order of Taylor micro-scale, typically between 50 and 150 viscous units. They have also been shown to contribute significantly to the Reynolds stress in the outer part of the turbulent boundary layer, and exhibit a considerable Reynolds number dependence (see Falco 1977 and 1983).

Experiments conducted by Falco (1978a, 1979) using combined simultaneous visual/hot-wire anemometry revealed that, other than the well-known low-speed streaky structure, a much more energetic flow module also existed in the viscous sublayer of wall bounded turbulent flows. The flow module was created as one result of the frequent rearrangement of existing wall region vorticity, by outer region interactions. It was characterized by the initial movement of marker away from a local region, leaving a scoured area of low marker concentration. Because of its nature, appearance, and intermediate scale, he called the flow pattern a "pocket". More detailed observation showed that the pocket flow module was characterized by having spanwise widths typically between 50 and 150 wall layer units and lengths about 30% greater than its lateral dimension. Analogous to the low-speed streaks, the presence of pocket flow motions is arguably a sufficient condition to distinguish a given boundary-layer flow as laminar or turbulent transitional, since pockets were observed to form in the transitional flows, in the upstream edge of the arrowhead-shaped turbulent spots as well as under spots (see for example, figure 111 of Van Dyke 1982), and in all turbulent regions downstream. Some investigators felt that the pockets were merely visual artifacts with no dynamical importance. Falco (1980) showed that it is necessary to have both the correct visual technique and the quantifiable results to investigate pockets. The numerical calculation of a turbulent channel flow using DNS by Kim et al. (1987) revealed that different flow patterns were emphasized by different visualization techniques. Their results illustrated that the formation of low-speed streaks was well presented using hydrogen-bubble time lines parallel to the wall, whereas the pockets were clearly shown by the illumination of smoke-filled boundary layer. The simultaneous visual/hot-wire results of Falco (1980) and Lovett (1982) documented the kinematic signature of the pocket flow module.

Using inclined laser planes to study flow characteristics of turbulent boundary layers at modest Reynolds numbers, Head and Bandyopadhyay (1981) proposed that turbulent boundary layer was filled almost exclusively with vortex loops or hairpin-like vortices of a variety of scales originating in the wall region and extending outwards at a characteristic angle of about 45 degrees to the flow direction. Their assertion led to the controversy concerning the coherent shape of the important vortical motions existing across the outer region of the boundary layer. Are the typical eddies best characterized as ring-like or hairpin-like motions? Using flow visualization recorded in two mutually orthogonal laser sheets by Falco (1979) indicated that the coherent feature was indeed ring-like vortical motion (also see Falco and Signor 1982). Stanislas and Hoyez (1990) also visualized mushroom-shaped coherent motions existing close to the wall in oil-smoke filled turbulent boundary layers at modest Reynolds numbers. They pointed out that these motions seemed to be produced near the wall and needed to be taken into account in the wall-region dynamics. Falco (1991) noted that the disagreement is primarily in the outer portion of boundary layer. He postulated that hairpin vortices are dynamically important only in the near wall region, and are the dominant flow feature solely in transitional flows and downstream of tripping devices around which the flow is separated. This physical picture was given further support by the studies of Lu and Smith (1988), who indicated that hairpin heads were observed most probably in the range of $28<y^+<32$. In addition, computational data base of Jiménez, Moin, Moser, and Keefe (1988) suggested that the tip portion of the elevated sheet-like shear layers tended to level-off at $y^+\approx35$.

The origin of wall region hairpin vortices has also been investigated by a number of researchers. Falco (1982, 1983) observed the sublayer vorticity re-organizing into hairpins in the downstream end of pocket flows. Acarlar and Smith (1984, 1987a,b) produced evidence showing that the shear layer instability of long low-speed streaks was responsible for the formation of hairpin vortices. Experiments involving the interaction of a laminar ring vortex with a laminar Stokes' layer by Chu (1987, also see Chu and Falco 1988) clearly showed that both of the mechanisms described above could create hairpins near the wall. In addition, Falco, Klewicki, and Pan (1989a) also witnessed the evolution of hairpin flows with their legs straddling the long streaks in a low Reynolds number turbulent boundary layer.

The existence of other important structural features such as longitudinal streamwise vortices has also been addressed (see, for example, Bakewell and Lumley 1967, Lee, Eckelman, and Hanratty 1974). Many proposed that pairs of long counter-rotating axial vortices existing in the wall region provided a natural cause for the formation of long low-speed streaks. The high-speed streaks, which were occasionally observed to form for short extent very close to the hydrogen bubble wires, would be the result of high momentum fluid being induced towards the wall between these vortex pairs. However, this conjecture has not been proven since the streamwise vortices in the wall region found were all of short extent (see, for example, Praturi and Brodkey 1978, Falco 1979, Smith 1982, and Nishino, Kasagi, and Hirata 1987). In contrast to the hypothesis regarding the existence of counter-rotating vortex pairs, there are also investigators reporting that solitary vortices are more prominent than vortex pairs in the vicinity of the wall (see, for example, Moser and Moin 1984, and Nishino et al. 1987).

The kinematic signatures of the various structural features observed have been studied by means of visualizations, quantitative measurements with conditional sampling process, or computational simulations by a number of investigators. The dynamical significance of these motions have been put forth in many differing inferences. Although many results have suggested that these characteristic features were, more or less, associated with the production of Reynolds stress, an overall relationship existing between these motions, which leads to a chain of events that can be labelled the turbulence production process, has yet been fully established.

1.3 The Production of Turbulence in the Near-Wall Region

Since Prandtl proposed the boundary layer theory in the early years of the twentieth century, attention has been drawn to the thin layer of fluid adjacent to the wall which has been found to be strongly influenced via viscous effects. In turbulent boundary layers the nature of the wall region is not completely understood, but the importance of this thin layer regarding the generation, transport, and maintenance of turbulence has been sufficiently documented. Laufer (1954) presented turbulence data from a fully developed flow in a smooth pipe, indicating that the peak production of turbulence occurs just outside the viscous sublayer, in the buffer region. If we integrate the energy production outwards from the wall, it can be shown that nearly 80% (qualitative estimate) of the net production takes place within the first 50 wall layer units, well inside the lower portion of the log region. Therefore, flow motions in the inner and log region play an extremely important role in the production of turbulence near a wall.

The question could be raised : What is the importance of understanding the turbulence production process? The answer is simple, since energy consumption has been - and continues to be - a crucial factor in the world economy, the reduction of drag and the associated savings in energy consumption in the innumerable devices of our modern technologically based world has been the subject of intensive and numerous studies for many engineers. Much work has been done (see, for example, Wilkinson and Balasubramanian 1985, Falco 1989, Moin, Kim, and Choi 1989) in seeking the mechanisms which are responsible for the bursts of turbulence production in boundary layers, in the hope that substantial drag reduction could be achieved through modifications of the processes. The philosophy has been that learning the underlying process provides the best way to understand how to interact with the process so as to affect a control. Thus, understanding the production process is essential to drag reduction studies.

1.4 Proposed Models of Turbulence Production in the Wall Region

The search for mechanisms responsible for the turbulence production process in the near wall region has resulted in a number of hypotheses. Attention has been focused upon the wall region breakup described by Kline et al. (1967), who observed that the sublayer streaky motions lifted up, oscillated, and eventually broke down. A similar observation was reported by Corino and Brodkey (1969), who used suspended solid particles of colloidal size in a pipe flow to create physical pictures very near the wall. This sequence was later collectively called the 'bursting' phenomena (Kim et al. 1971). They also reported that all the net turbulence production within the first 100 wall layer units of the flat-plate flow occurred during times that involved lifting of the low-speed streaks and ejection processes. Many investigators, who believe the streaky structure in the near wall region is dynamically significant, have proposed different models to describe the event as though its formation and the subsequent instability were the essential cause of the turbulence production near the wall. However, there are also many others that feel the streaks are passive and thus not a factor of the near-wall-region dynamics. Kline (1988) clarified the view by pointing out that the low-speed streaks, when lying on the wall, appeared to be passive, but they were certainly involved in much of the turbulence production in the layer above the wall region as they were lifted away from the wall interacting with the outer part of the flow. The important question of why they lifted up was not answered.

Early attempts were made by Lee et al. (1974), Townsend (1976), Blackwelder and Eckelmann (1979), and many others to explicitly model the longer time scale events, which were pairs of streamwise oriented vortices that were attached to the wall. The models were primarily deduced from statistical correlation measurements. Their conjecture suggested that the ensuing rapid breakdown of the wall region flow was a result of the evolution of these motions which instantaneously inflected the mean velocity profile. Some investigators attributed the origin of these streamwise vortices to a Taylor-Görtler type instability in which the centrifugal force was supplied by the motion of large scale structure in the outer boundary layer. The suggestions that conditions for onset of the turbulent boundary instability remains questionable because they are based upon a homogeneous steady-state stability analysis of Taylor and Görtler, which may not be applicable to the unsteady flows in the wall region.

A model proposed by Offen and Kline (1974, 1975) suggested that the rapid breakdown of the sublayer flow was a result of local adverse pressure gradients that occurred near the wall due to the presence of a transverse vortex with rotation of the same sign as that of the mean vorticity in the boundary layer. Laufer (1975) and Oldaker and Tiederman (1977) also proposed models to interpret the events. Oldaker and Tiederman suggested that pairs of sublayer streaks were created as a result of the response to a sequence of local high speed outer region eddies convecting over the wall. Laufer attributed to a relatively larger scale sweep containing regions of small scale vorticity that had the size of streak formation events.

Smith and Metzler (1983) suggested that the low-speed streak merging process often observed in the region of buffer layer ($10<y^+<20$) could be closely related to the turbulence production. They also postulated that the small stretched and lifted hairpin vortices near the wall were responsible for the merging behavior and the streak persistence. Head and Bandyopadhyay (1981) suggested that streak was formed between the legs of a lifted hairpin. However, the ability of the proposed mechanism to provide the persisting time for a streak of length in the order of x^+=1,000 is suspicious. This problem was later resolved by the modification of Smith and his co-workers (1984, 1987b), who described that the formation of long sublayer streaks was due to a series of lifted hairpins forming in roughly a longitudinal chain, building up the necessary persistence time for long streaks to develop. Falco (1979) observed that the long streaks could be formed as a result of the joining of a staggered array of the streaks that bound pockets, which provided an explanation of the persistence time of long streaks. Although there is some rationale for each physical assertion mentioned above, the apparent mechanism for long streak formation and its subsequent bursting is not completely understood because it has not yet been confirmed by an objective statistical analysis.

Other models such as vortex induced ejection of wall region fluid (see, for example, Willmarth and Tu 1967, Nychas, Hershey, and Brodkey 1973), as well as high-speed inflows and continuity (see, for example, Eckelman, Nychas, Brodkey, and Wallace 1977, Praturi and Brodkey 1978) have also been put forth. Despite many detailed differences in these proposed models, it was overwhelmingly clear that they support the hypothesis that the sublayer instability occurred as a result of the interaction between the outer and the inner region motions. These differed from older models in which the inflows relied solely upon the law of continuity.

Research focused on the formation and evolution of pocket flow modules has been led by Falco and co-workers (1978-1980). He presented experimental evidence showing that the most intense ejection of sublayer fluid occurred at the downstream end of the pocket in which a hairpin-like vortex filament could be readily observed. He also classified the evolution of pockets, with average lifetime in the order of 30 viscous units, into five stages of development. The physical processes, that were phased to the evolution stages were closely associated with the sweeping event and bursting sequence.

In addition, he advanced a hypothesis for the cause of the pocket creations. He proposed that they were the footprints of vortical sweeps whose vorticity was organized in ring configurations as suggested by the scale of pockets and the existence of counter-rotating vortices. This constructed a model which coupled both the inner and the outer region known coherent features through the interactions of typical eddies and the existing wall region vorticity distribution. However, the relative importance regarding the contribution to the Reynolds stress in the near wall region, of pocket related bursting seen by Falco and the long streaky structure related bursting observed by Kline and his co-workers apparently exists.

In a visualization experiment, Falco (1983) found that the wall region vortex filaments could evolve into typical eddies. Therefore, he hypothesized a cyclic turbulence production process in which ejected fluid evolved into typical eddies and many of them returned to the proximity of the wall as sweeps to create wall region disturbances as well as new ejections. Nevertheless, he pointed out that most of the ejected fluid from the downstream end of pockets was not directly observed to form new typical eddies. Although a computational work using the Biot-Savart law by Moin, Leonard, and Kim (1985) also clearly showed that the tip region of an elongated hairpin vortex evolved into a vortex ring in turbulent shear flows, additional evidence is needed to support the model which suggested a closed cycle.

In order to examine the typical eddy/wall layer interaction hypothesis, physical simulations of the interaction between a laminar ring vortex and Stokes layer were performed to model the process (Chu 1987, Chu and Falco 1988). The simulations enabled an uninterrupted environment in which important structural features associated with the production process could be distinguished. The adjustable parameters in the physical simulations were optimized to match the observations in fully turbulent wall flows. As a result, the simulations successfully exhibited <u>all</u> of the known structural features and their evolutions in turbulent boundary layers. With a Galilean transformation on the velocity field, the simulation clearly indicated that a pair of long streaks was created, normally accompanied by a pocket formed near its downstream end, as a ring-like vortex impinged the wall layer with a shallow incident angle.

Motivated by these findings, subsequent experiments by Falco, Klewicki, and Pan (1989a) presented data of long time averaged two-point spanwise vorticity correlations, with a fixed probe at the edge of the viscous sublayer and an upper probe at various positions between 15 and 125 Δy^+ above the fixed probe, in order to statistically characterize the spatial interactions of inner/outer layer distinct vortical motions (also see Klewicki 1989). Results showed that the negative vorticity fluctuation correlation was consistent with the presence of typical eddy at the upper probe (which would result in positive total vorticity during its passage), and a strong negative vorticity fluctuation at the fixed probe (which could be either the pocket vortex or the hairpin vortex at its downstream end). Note that the mean shear had vorticity of negative sign. The joint probability density function also showed the counter-rotating contributions to the correlation occurred only when total vorticity measured at the upper probe was positive. This statistical result reinforced the hypothesized relationships of the known inner and outer region coherent motions. An Overall Production Module (OPM), which integrated the details of the production model developed through years (Falco 1977-1983), was put forth accordingly (Falco et al. 1989a, Falco 1991).

1.5 The Overall Production Module (OPM)

The OPM is composed of two major subsets. These two subsets complimentarily account for all the dynamically significant motions found in both the inner and outer regions of turbulent boundary layers. They are briefly described as follows.

Log/Outer Region Subset : motions initiating the near wall region response

An essential feature of the OPM dynamics is the initiation of near wall region response through the interaction with highly vortical microscale typical eddies propagating over the wall. Figure 1.1 shows a sketch illustrating the spatial relationships between typical eddies and the large scale motions (LSMs). This phasing results in the typical eddies being brought to the close proximity of the wall. The intrusion of these outer region perturbations is proposed to be responsible for the onset of the near wall region subset of the OPM. An important feature behind this inner/outer region interaction is the LSMs, which provide or induce the instantaneous wallward momentum carrying the typical eddies towards the wall to trigger the wall region responses.

Wall Region Subset : evolution and transport in the near wall region

Being excited through the outer region perturbation, the existing near wall region vorticity undergoes rearrangements as well as specific spatial/temporal interactions, which comprise the wall region subset of the OPM. Figure 1.2 illustrates a conceptual model showing four sequential stages of the wall-region evolution in the plan view. The evolution proceeds as follows. First, a pair of long sublayer streaks is formed. Then, a pocket is created at the downstream end of the streak pair, in between the streaks. The deformed upstream sublayer vortices, which actually form the upstream boundary of the pocket observed in visualization, are called the pocket vortices. In the downstream side of the pocket, the elevated vortex loop is called the primary hairpin vortex. In the evolution of the streak pair, a certain time period is necessary for the growth of an instability that often results in the formation of hairpin vortices over the streaks. These vortices are called the secondary hairpin vortices.

During the evolution of the various coherent features, each feature contributes a portion to the total turbulence created by the production module. However, the proposed

OPM encompasses a complete spatial/temporal interaction, which is seldom seen in highly perturbed environment of turbulent flows. A significant number of the observed turbulent wall-flow evolutions appeared to consist of only fractions of the wall region subset.

1.6 The Motivation

Based upon our survey of investigations of the wall-region dynamics, results suggest that two aspects are most important (There are, of course, some grey cases, but on the basis, the distinction is clear). The first one emphasizes the formation and the subsequent bursting of the wall-region streaky structures that were first observed by Kline and his co-workers as the mechanism of turbulence production, whereas the second attributes turbulence production mainly to the typical eddy/wall layer interactions leading to the pocket evolutions, interactions with the streaks, and breakdown (Falco and his co-workers). It is obvious that the former has so far drawn much of the attention of researchers. In spite of the fact that there are about as many differing inferences as the researchers involved in the investigations of this topic, the input of views are fruitful and often unassailably rational. It seems that more research focused on the evolution of the individual coherent motions is not what is primarily needed at this moment. Research focused on interactions that can help explain the initiation of the events as well as their evolution and phasing is of primary importance. The Overall Production Module proposed by Falco et al. (1989a) and Falco (1991) rationally links essentially all structural features found in the turbulent boundary layer, including typical eddies, long sublayer streaks, hairpins, pockets, LSMs, and streamwise vortices. It provides a frame work and overall interaction model. On the surface, it appears to contradict a number of view points held by other investigators. Thus it appears worth doing further research to statistically investigate the precepts of the model.

1.7 Subject of the Current Study

On the basis of mounting experimental evidence, it is increasingly apparent that the interactions between Taylor micro-scale typical eddies and the existing sublayer vorticity distribution is a crucial process concerning the production of turbulence in wall bounded shear flows. On the other hand, when it comes to understanding how various structural elements relate to and/or interact with each other, and what the parameters are governing this important event, our knowledge is still very limited. Hence, searching for reliable data characterizing the important spatial/temporal inter-relationships associated with the occurrence, formation and alignment of these coherent features, that participate in the near-wall production process, is very desirable.

The subject of my dissertation is to investigate a turbulent boundary layer flow, with particular emphasis on the fluid motions near a smooth wall, and to gain insights into the physical picture of the coherent structure interactions that are embodied in the OPM. In so doing, a conditional sampling procedure has been employed with the aim that it will most directly extract statistically significant features of the correlated coherent motions and their interactions. The intent is to provide statistically reliable quantitative data. In addition, we have coupled this with qualitative long time boundary layer observations to get a better understanding of the interaction process between the inner/outer region distinct vortical motions. Special emphasis has been placed on uncovering the underlying mechanism that is responsible for the formation of long low-speed streaks and pockets. The visual data base for the inner/outer region interactions has been constructed in both two and three dimensions. This enables us to observe the coherent motions in all complementary views. Furthermore, the description of the interactions in terms of the probability for the simultaneous occurrence of the correlated structural elements will be made. The results would serve as a measure of the importance of the interaction in the production of turbulence near walls. We will also present visual evidence that supports the conceptual description of the OPM.

CHAPTER 2

EXPERIMENTAL TECHNIQUES

2.1 The Water Tunnel Facility

Experiments were performed in a recirculating water tunnel in the Turbulence Structure Laboratory at Michigan State University. The tunnel, which was made of plexiglass, was 15.2 cm high by 91.4 cm wide by 6.4 meter long. It was part of the closed flow system. Figure 2.1 shows the top view and side view of the flow facility which basically consisted of the tunnel, a driving motor with shaft, two reservoirs, a honeycomb screen, a contraction, and a 15.2 cm radius back flow pipe which was installed underneath the tunnel. Fresh water could be filled in the flow system from the top of the main reservoir as indicated in the figure. The maximum capacity of the flow facility was approximately 4500 liters. The main reservoir contained a sheet metal elbow which was attached to two fixed plywood boards to ensure that the circulating flow stream would have a fairly smooth 180 degree route to invert its direction. The corner effects in the main reservoir such as the secondary vortices were able to be isolated from the main stream since the reservoir was divided into three chambers by the presence of the two plywood boards.

Care was also taken in the design of the inlet and outlet configurations of the tunnel to avoid any possible influence upon the flow in the observation section due to the return circuit arrangement. A honeycomb screen was inserted in the conjunction of the main reservoir and the contraction (also in between the downstream end of the back flow pipe and the main reservoir). This fine honeycomb screen was designed to diminish any vorticity that might have existed in the flow before entering the tunnel, especially for the large scale vortical flow structures created by the redirection of the flow in the main reservoir. After the water had passed through the honeycomb screen, it would be gradually increased in speed with the aid of the 1.14 meter long contraction, whose area ratio was 5.2 to 1, before flowing into the constant cross-section tunnel. At a point about 28 cm downstream of the tunnel inlet, 6.4 mm diameter threaded rods were attached to both the lower and upper surfaces to trip the flow. Tripping the flow was not necessary to ensure a fully developed turbulent flow at the measuring station, but did serve to localize transition as well as to achieve spanwise uniformity.

The downstream end of the tunnel and the back flow pipe was connected via a secondary reservoir. A flat plexiglass plate with varying diameter holes was placed on the top of this reservoir and aligned with the lower surface of the tunnel. Since the diameter of the holes was designed to grow with distance downstream, the resistance for the water to be delivered into the lower secondary reservoir decreased as the distance downstream increased. This could extend the area for water to fall so that the sudden hydraulic head loss, which might result in a very stirred stream in the entrance of the back flow pipe as well as a possible disturbance back to the upstream observation zone, was prevented.

The flow driving assembly was mounted on vibration absorbers and located in the lower part of the secondary reservoir. At the inlet of the back flow pipe, a shaft with a propeller blade at one end was installed coaxially with the center of the pipe. The diameter of the propeller was selected to fit the inside diameter of the back flow pipe. The other end of the shaft was extended to the outside of the reservoir and driven by a 300 Volt 5.8 ampere Reliance Super 'T' D-C motor with an adjustable-speed power supply. A V-shaped belt (not shown in the picture) was provided to transmit the power from motor rotor to the axle of the shaft. The water was then pumped back to the main reservoir through the return pipe to continue the recycling process. Furthermore, a 91.4 cm long wooden cross was inserted in the end of the return pipe in order to nominally regulate the flow direction before the fluid streamed into the main reservoir. A drain was located near the bottom of the main reservoir.

It is emphasized that the flow system was originally built for developing a channel flow in the constant cross-section tunnel. However, in the present work the flow facility was employed to deliver a turbulent shear flow along the lower surface of the tunnel with other side of the flow un-sheared (i.e. an open channel flow or flat-plate flow). No modification of the flow system was required in order to run a flat-plate flow. Nevertheless, a 76.2 cm by 43.2 cm window was constructed on the top of the observation area to gain a better access of adjusting the optical setup of the cross-stream view. The advantage of using a flat-plate flow instead of a two-dimensional dual boundary layer channel flow in this investigation was that the clarity of the plan view and the cross-stream view was considerably improved by directly viewing through the water surface without crossing the upper plexiglass wall. In addition, the laser sheets were able to illuminate the flow in full strength without being interfered by the presence of the plexiglass wall.

The observation section was a 10.2 cm wide by 10.2 cm long by 3.6 cm high volume of space that started at the wall 3.2 meters downstream from the trip wire. A 61 cm wide by 15.2 cm long hatch was fabricated on the lower plexiglass wall for installing experimental apparatus such as wall slits, Pitot tube and wall taps, or hot film probe.

2.2 Mean Velocity Acquisition

In addition to the advantages mentioned above, the employment of an open channel flow tended to reduce the physical scale of the coherent motions in the turbulent boundary layer. This is because that, for constant power input, the shear stress at the wall of an open channel flow is substantially greater than that of a channel flow. Accordingly, u_τ is also greater for the open channel flow, which would allow structural features characterized on wall variables to reduce their physical magnitude. Since the flow visualization of smaller coherent features would be difficult, compromise must have been made to set the flow speed as low as possible, but not too low so that the Reynolds number could be kept in the order of 1000. As a result, a low speed flow has been employed throughout the present study. The speed dial (scaled from 0 to 4.0) of the motor was set at 1.5, which provided the power to drive the shaft at approximately 122 RPM. The decision of choosing a low Reynolds number flow was also affected by another factor, which will be addressed in Section 2.5.

Hot film anemometry was supposed to be the ideal method of obtaining the velocity profile in a liquid flow. However, the attempt did not succeed in our experiment because the design of the flow facility made it impossible to keep the circulating water clean enough. The water contained small particles that stuck on the hot film probe and caused false voltage readouts. The damage of the hot-film equipment led us to utilize an alternative approach for the measurement of the mean velocity profile. The pressure measurements of Pitot tube and wall taps just provided the necessary mean.

Figure 2.2 shows the setup for the pressure measurements. The pressure readings were taken with one Pitot tube and two wall taps. The nose of the Pitot tube was flattened to a 4.1 mm wide and 0.8 mm high opening. The elbow was also bent towards the wall approximately 15 degree enabling the probe to reach the wall as close as possible. Note that the tip portion of the Pitot tube was still kept parallel to the flow direction. The Pitot tube was then mounted to a vertical traverse mechanism, which was capable of positioning within ±0.025 mm backlash, to allow the probe to move over the entire boundary layer. The closest point could be measured was 1 mm above the wall. Two 3.2 mm diameter wall taps were located symmetrically at the same cross-stream plane as the nose of the Pitot tube and 2.54 cm separation at its both sides. The pressure hoses connected to the wall taps were merged into one hose and hence provided the mean static pressure at the measuring station.

Since no micromanometer was necessary to display the readouts, special arrangement was taken to ensure accurate pressure readings. Two glass tubes placed side by side along with a ruler were fastened to a board to show the distinction of pressure levels. The board was painted in black to provide a background that allowed the water surfaces in the tubes more visible. Flexible plastic tubing was used as the intermediate connection between the pressure probes and the glass tubing. Glass tubing was chosen to display the pressure readings simply because it was clean, straight, and easy to read. In addition, the tendency of (electrical) static buildup was low compared to that of plastic tubing.

One advantage of this velocity measurement setup was its simplicity, which enabled the velocity to be measured directly without the application of a correction factor or a calibration process. With these pressure probes, the mean velocity in the streamwise direction could be computed by the equation,

$$\bar{u} = \sqrt{2gh}$$

where, h is the pressure differential (P_t-P_s), and g is the gravity.

Since the water was flowing at a low speed, the pressure difference, P_t-P_S, was expected to be small. This would make the measurement difficult and allow small velocity variation undetected. In order to decrease the sensitivity of the measuring scheme, the anemometer board was rotated to a position in which the angle between the glass tubing and horizontal was 30 degrees (the analysis of the relative uncertainty and sensitivity for this mean velocity measuring scheme is described in Appendix C). This rearrangement resulted in that the reading scale of the pressure differential along the side of the glass tubing was doubled as illustrated in the Figure 2.2. The meniscus in the glass tubing caused by the water surface tension could also create difficulty for pressure reading. However, the only measurement needed to calculate the velocity was the pressure difference. To rid of the meniscus problem, we chose the upper edge of the meniscuses as the reference points and carefully measured the pressure difference based upon the reference points. To avoid false readouts, care must be taken to ensure no air bubble existing in any segment of the tubing.

The time needed to complete the velocity measurements was about two hours. During this time period, the static pressure decreased slowly with time owing to small leaks in the flow system. In order to minimize the effects of this pressure loss, water was added to the reservoir from time to time for keeping the pressure head constant. Since only pressure differential was of interest, this pressure fluctuation should have negligible influence upon our measurements.

The mean velocity on the free surface was determined approximately by the use of surface floats. Two measuring stations were chosen for observing and timing the drifting floats. One was located 61 cm upstream from the position of the Pitot tube, and the other was 122 cm downstream of the first measuring station. Styrofoam of about 5 mm diameter was used as the floats. In order to collect a sufficient number of data, we had repeated the experiment 15 times. Since the free-stream surface was free of eddies and waves, this method should have given a fairly close estimate of the surface velocity. More importantly, this measurement provided a matching condition for the data obtained from the pressure probes and hence helped us to evaluate the accuracy of the pressure measurements.

2.3 Flow Visualization Setup

In the experiments, the boundary layer motions were made visible by using two (and at times three) orthogonal views of two or more differently colored dyes being emitted from the wall slits. The setup of the experimental apparatus employed is schematically sketched in Figure 2.3. A special parallel wall slit was fabricated that allowed the introduction of two colors of dye through slits separated by 5.1 cm (about 440 wall layer units) in the streamwise direction. Figure 2.4 shows the diagram illustrating the design of the double-dye slit. The slits had openings of 10.2 cm wide and one tenth of a millimeter long in the streamwise direction. They fit flush with the wall so that the dye was emanated tangentially, and hence the flow would not be disturbed. In the past, flow visualization studies of the wall region were complicated by the "history" of the flow. The concentration of the markers (dye or oil droplets) was diluted or dissipated rapidly after several hundred wall layer units downstream of the wall slit, and thus was unable to provide reliable information in determining the temporal evolutions and/or the instantaneous spatial correlations for events that had length scales longer than the order of a hundred wall layer units. In the present set of experiments, the double-dye slit enabled a "refresh" of the visual information. This allowed the separation of old and new events, and put undisturbed markers a position downstream of events that redistributed markers from the upstream slit. We thus minimized the "history" effect as well as gaining the capability of observing some longer-time sequencing of wall region evolutions. For convenience, hereafter we name the upstream slit of the double-dye slit the "first slit" and the downstream slit the "second slit". A 3.2 mm diameter dye injection nozzle, which was covered by a manifold with a 25.4 cm wide and 2.54 mm high opening allowing dye to be emitted parallel to the flow, was located 22.9 cm (about 2000 wall layer units) upstream from the first slit.

The illumination of the dyed fluid in the boundary layer was provided by a laser light which was spread into sheets that could be placed parallel to the flow and perpendicular to the wall (side view), or perpendicular to the flow and the wall (cross-stream view or end view), or both. The plan view was illuminated by two 300 watt flood lights. The laser light was supplied from a Plasma Kinetics Model 451 Copper Vapor Laser. The 40 watt laser beam was divided, by a 50/50 beam splitter at 45 degree inclination, into two orthogonal beams that were eventually transformed into laser light sheets that mutually intersected at 2.42 cm (about 210 wall layer units) downstream from the second slit. The excess brightness in the plan and side views caused by the laser sheets was partially blocked using black filter strips allowing the flow motions in the neighborhood of the bright spots more visible.

The dye suppling system included three reservoirs from which fluids, which could be dyed, passed through the adjustable valves, whose openings could be varied, to the inlets of double-dye slit as well as the upstream injection nozzle. The volume rate of dye emitted depended upon both the height of the dye reservoir and the opening of the adjustable valve. The dye reservoir connected to the upstream injection nozzle was filled with a mixture of 20 ppm (part per million) fluorescent Sodium Salt Sigma No. F-6377 green dye and water solution. As the valve opened, the mixture was released from the upstream injection nozzle by the pressure head. This resulted in that the dye marked fluid rolled away from the wall as it drifted towards downstream, and thus enabled the fluoresced flow motions in the log and outer regions of the boundary layer to be delineated by the laser sheets in the observation section. On the other hand, the fluid emanating from the first slit was a mixture of 20 ppm fluorescent Exciton Kiton No. 620 red dye, red food coloring, and water solution. This allowed the formation/evolution of the dynamical structures in the sublayer to be visualized via the illumination of the flood lighting as well as the laser sheets. The second slit emitted a mixture of 20 ppm fluorescent green dye, green food coloring, and water solution. This was designed to extend the visual information further downstream. Care was taken to ensure that the mass and momentum flux of the dyed fluid, injected through the slits in the wall, was small compared to the flux in the viscous sublayer. It is important that the latter needed to be essentially undisturbed. It is also worth noting that the dye coloring combination used in the experiments offered the best visual effects (provided that the stainless steel surface of the double-dye slit gave a white background) among many combinations that we had tested preliminarily. Furthermore, the additive of food coloring to the dye solutions used in the wall slits was of particular value in showing the sublayer structures in the plan view under the flood lighting.

With the aid of mirrors, three mutually orthogonal views were directed to a collecting mirror, in which the images could be filmed by a camera, mounted over the top of the window. A 7.6 cm wide by 6.1 cm high front-silvered cross-stream mirror was placed on the wall inclining to the flow direction in the middle of the channel (to assure the symmetry of the flow field). It reflected the images of the cross-stream plane up to the collecting mirror. The inclination angle of the mirror was optimized at 45 degrees, which was the result of the compromise between the blockage effects and the reflection angle. The presence of the cross-stream mirror would, however, have complicated the flow field in the regions of interest if the mirror had been positioned without sufficient distance from the observation area. Preliminary experiments were conducted at a series of locations upstream of the mirror in determining its position so that the mirror imparts would have minimum influence on the flow and virtually no effect on the visual (qualitative) information presented in the observation area. As a result, the cross-stream mirror was located at a point where the distance between the second slit and the leading edge of the mirror was 19.3 cm (about 1670 wall layer units). This resulted in that the downstream end of the observation section (i.e. the position of transverse laser plane) was approximately 1520 wall layer units upstream from the mirror.

2.4 Data Recording

The primary visual data consisted of simultaneous plan view, side view, and cross-stream view of time resolved images which were recorded using 35 mm and/or 16 mm high speed cameras. In order to acquaint visual information with acceptable clarity as well as tractable temporal relationships between the orthogonal views, three methods have been employed.

Method 1 : Dumped all the information in a single film (i.e. one camera with split field). Theoretically, this should have been the simplest and best way because all the data stored in one frame was automatically synchronized and the temporal relationships for events of interest could be easily quantified by manipulating the known framing rate. Nevertheless, this method required the path lengths (i.e. the length between the object and the camera) for all three views to be approximately identical. The path lengths for side and plan views were able to be set equal by simply adjusting the positions of the mirrors. Since the path length for the cross-stream view was much longer than that of the side and plan view, a combination of one concave lens with 150 mm focal length and one convex lens with 200 mm focal length was installed along the path as shown in Figure 2.3 to virtually eliminate the excess length. The cross-stream images could be enlarged, if needed, by increasing the distance between the two lenses. However, cautions must be taken to do this because it would degrade the clarity of the visual data as well as distort the images in the corners of the cross-stream view. The method had been carried out using a Photo-Sonics Series 2000 35 mm-4ML camera with 135 mm telelens as well as an 1.4 teleconverter. A 122 meter Kodak No. 5294 high speed color film was exposed at 1/500 seconds and 100 frames per second.

Method 2 : Stored the plan and side view information in one film, and the cross-stream data in another film. In doing so, a clock was required to provide the time information so that the two data sets could be related for later analysis. To use this method, the installation of the extra concave and convex lenses became unnecessary. This enabled the transverse view information to be taken directly by shooting at the cross-stream mirror. The main advantage of using this method was that the gains of higher resolution for all three views (especially for cross-stream view) allowed a more detailed picture of the flow to be studied. In addition, the possible image distortion in the cross-stream view caused by the extra lenses was avoided. This method had been employed using the 35 mm-4ML camera with 58 mm lens and two teleconverters (1.4X & 2X) for the plan and side views, and a Locam Model 50-0002 16 mm camera with 135 mm telelens for the cross-stream view. The film used in the 16 mm camera was a 61 meter Kodak No. 7250 high speed color reversal film. The film for the 35 mm camera was the same as used in *method 1*. The exposure times were 1/500 seconds and 1/900 seconds for 35 mm and 16 mm cameras respectively. The framing rate was set at 200 frames per second for both cameras.

Method 3 : In order to exclusively examine the wall region evolutions, a third method that only plan view was filmed has also been employed. Experiments have been carried out by directly shooting at the wall plane with flood lighting as the illumination. Laser light and upstream dye injection were not used for these experiments. Utilizing this method, we lost the correlation information with the structural features above the wall region, but we gained pictures of much higher clarity. This enabled the wall-region events of fine scale, particularly for flow motions of Kolmogorov scales (less than 10 viscous units) such as vortex filaments of hairpin vortices, to be possibly seen. The 35 mm camera and films used were the same to those used in *method 1*. The exposure time and framing rate were set at 1/500 seconds and 50 frames per second respectively.

Experiments utilizing *method 1* were carried out with some degree of success. However, in order to have flow pictures with sufficient details so that human eyes were able to easily identify the micro-scale coherent structures, higher resolution for images in the cross-stream plane was required. Therefore, the visual information collected using *method 2* provided the major data base for our statistical study. The pictures obtained using *method 1* and *method 3* provided good illustrations of sequential evolutions that revealed some important features of the interaction in the wall region.

2.5 Data Reduction and Principles of Conditional Sampling

Since the major purpose of the current study was to statistically characterize the structural features, which are involved in the wall-region interaction process, and their spatial/temporal inter-relationships, the extraction of the events of interest from the bulk raw data via a conditional selection process was necessary. Only the behavior of the principal flow motions such as typical eddies, pockets, and long sublayer streaks have been investigated. The characteristics of the hairpin vortices (primary and secondary) were not put in analysis because the resolution of our correlation data was incapable of showing flow details with sizes in the order of Kolmogorov scale consistently. Forcing the analysis will simply result in unreliable or false statistics. Additionally, since the formations of the primary and secondary hairpin vortices are often accompanied by the formations of pockets and long sublayer streaks respectively, their occurrence was deducible and thus was not the best interest regarding to the purpose of this study although they might be important in the contribution to the Reynolds stress near the wall.

The principles of the conditional sampling process were constructed based upon the objective of quantifying the correlation between major coherent motions that participated the inner/outer region interactions. In order to fulfill the need to study the phase relationship of these correlated events, we setup a designated area in the wall plane of the observation zone as our sampling reference. This designated area started from the second wall slit and ended at the streamwise location of the cross-stream laser sheet. The reason for setting up the designated area was also closely coupled with the utilization of the double dye slit. It is explained as follow.

It is understood that the wall dye injection is capable of detecting pockets near the injector. However, the formation of long sublayer streaks cannot be observed within the short duration and space over which the maker remains uniform enough to see the pockets. In regions further downstream from the injector, the dye will primarily be collected to form long low-speed streaks which usually have a longer lifetime compared to that of the pockets. As a result, diluted dye will be no longer able to outline pockets in these regions. Therefore, it is almost impossible to tell whether or not a pocket will form near the downstream end, and in between a long streak pairs if only one wall slit is used. This will severely inhibit the investigation of spatial phasing between pockets and sublayer streaks, particularly the long streaks. Thus, in order to make the entire version of the interaction and evolution visible, we employed the double dye slit. The basic idea is that we seep the red dye from the first wall slit enabling the development of long streaks to be visualized. Then, in the second wall slit, a different color dye is seeped in to continue (refresh) the visualization of the long streak formation and, more importantly, to provide an opportunity for the formation of the pockets to be observed in the designated area while the long streaks are still visible. In the downstream end of the designated area, a cross-stream laser plane was setup to observe the spanwise geometry of structural features. We were particularly interested in events in the log region and lower portion of the outer region, which might be associated with the initiation of the wall region evolution. The spatial arrangement of the designated area and the cross-stream laser sheet was set up according to the assumption that the pockets are produced right beneath the typical eddies impinging the wall as suggested by previous observations. This spatial arrangement enables the typical eddies, which are responsible for the formation of the sublayer features in the designated area, to be identified right after the onset of the interactions, and before they become unidentifiable due to the interactions that lead to significant distortion. Note that a special effort was also made to see if any other Taylor micro-scale coherent motions appeared in the cross-stream laser plane when pockets were forming in the designated area. We did not find other Taylor micro-scale coherent motions.

Figure 2.5 shows an isometric view of our interaction studies illustrating the general flow field, as well as the spatial phasing between the designated area, the observation arrangement and the multi-color dye system. It shows that the typical eddies delineated by upstream green dye convect downstream. Some of them will interact with the existing wall region vorticity field in the vicinity of the designated area. The principle of the sampling is simple, only sublayer features -- pockets and/or long streak pairs --

which are associated with the interactions are sampled. All typical eddies identified in the transverse laser plane within the first 300 wall layer units are also sampled. The simultaneous occurrence of a typical eddy in the transverse plane and the sublayer feature(s) in the designated area (they must be approximately aligned vertically) is labelled as a correlated (interaction) event. Samples containing typical eddies which occur in the transverse plane without sublayer features formed in the designated area underneath them are considered as events with no interaction. Based upon the principle, the rules of the conditional sampling procedure are described in details as follow.

1. *Pocket Sampling* : A pocket was recorded and measured only if it was observed to form in the designated area of the plan view. Note that, if any portion of a pocket was located inside the designated area while it was still evolving, the pocket would be sampled.

2. *Typical Eddy Sampling* : A typical eddy was sampled if it was identified and located between $y^+=300$ and the wall in the cross-stream and/or side view. If sampled from the side view, it must be identifiable when crossing the transverse laser plane. In order to avoid mistakenly recognizing some strong hairpin vortices as typical eddies (since the visual impression of their spanwise geometry was, at times, similar to that of typical eddies), only images that were dyed with green dye, that was introduced upstream, were chosen. Since hairpins would be dyed red, because they were lifted wall layer fluid from the immediate upstream wall region. This extra degree of discrimination is gained because of the multi-color dye system.

3. *Long Sublayer Streak Pair Sampling* : A long low-speed streak was identified as a well-defined streamwise concentration of dyed fluid marking an extended region of low-speed motion. Its streamwise extent must have been greater than 100 wall layer

units. A pair of the long streaks was recorded and measured only if at least one of the following conditions was met:

(i) In the plan view, a streak pair was sampled when a pocket in the designated area was formed between the streaks, and in the neighborhood of the downstream end of the streak pair.

(ii) In the cross-stream view, a streak pair was sampled when the center of an identified typical eddy was approximately aligned over the center of the streak pair whose downstream end was also in the vicinity of the line intersected by the transverse laser sheet and the wall. Under this condition, only the streak pairs whose downstream ends located inside the designated area or did not exceed 100 viscous units downstream of the intersection were sampled.

4. *Criteria for the Correlated Interaction Events* : As mentioned earlier, a streak pair and/or a pocket were considered to be correlated with a typical eddy if the sublayer feature(s) were observed to form underneath the passing typical eddy. In a couple of occasions, the words "approximately aligned" were used in this section to describe the spatial phasing between the typical eddies and the sublayer features. Here, a criterion is constructed to quantify the definition of the vertical alignment of coherent features. That is, the spanwise spacing between the centers of the typical eddy and the sublayer feature must have been less than a quarter of the spanwise dimension of the sublayer feature in order that they were accepted as a correlated interaction event. If both the sublayer features were formed, the comparison was made with the pocket width (because the streak pair was usually well aligned with the pocket). It is also important to note that no correlation between a typical eddy and a sublayer feature was considered to exist if the difference of their spanwise dimension was two times greater than either dimension. This

constraint would have automatically rejected the cases, in which irrational size differences of coherent features occurred, as correlated interaction events.

With regard to the sampling of typical eddies from the transverse view, a question to be answered is : Were all the observed vortex pairs dyed with green dye simply connected vortex loops? It is believed that our samples do not contain vortex loops that had "legs" attached to the wall because of our spatial arrangement of dye emission. The distance between the first slit and cross-stream laser plane was approximately 7.6 cm ($\approx 650\ x^+$). This constraint could probably eliminate the possibility that the hairpin vortices, created in the wall region between the upstream injector and the first slit, were able to elongate in the streamwise direction for the necessary distance to appear in the transverse laser plane. It is more convincing if one realizes that the distance between the origination of hairpins at the upstream dye injector and the transverse laser plane was about 2650 viscous units. It is very hard to believe how hairpin legs could stretch this far without severe re-orientation of their vorticity field. This inference is reinforced by the findings of Head and Bandyopadhyay (1981). They reported that the hairpin vortices were very much less elongated in the streamwise direction at low Reynolds numbers ($R_\theta \leq 800$) and were better described as vortex loops or horseshoe vortices. Accordingly, at current flow condition ($R_\theta \approx 800$), the identified typical eddies dyed with green dye in the cross-stream laser plane are more likely to be vortex loops than hairpins with legs that connected to the wall. This was the another reason why we chose a low Reynolds number flow to conduct the investigation.

Figure 2.6 illustrates the on/off conditions for the sampling process employed in the present study. Fourteen conditions are shown to represent the most often seen combinations between plan and cross-stream views. Based upon the rules described above, all the observed typical eddies were sampled, and the chosen samples of the sublayer structures correspond to conditions 1, 2, 3, 11 and 13. Note that, for condition 13, only a pocket was chosen.

The visual data were analyzed on a Nac Model PH-350B Film Motion Analyzer with a X-Y calibrated scale for 35 mm films, and/or a Nac Model DF-16C Analysis Projector for 16 mm films. The images of latter were displayed on a ground glass screen and read from the reverse side of the screen to eliminate the parallax errors associated with using a standard movie screen and viewing from an angle. The visual analysis of the movies consisted of observing the individual events, identifying the events in a number of runs, making a thorough study of each of the events and their relationships with other simultaneous events, and quantifying, if possible, the characteristic features of statistical importance. The reduced data were statistically manipulated and displayed by using a Sun 4/260 computer workstation and its peripheral devices.

CHAPTER 3

RESULTS

3.1 Mean Velocity Profile and Flow Parameters

A velocity traverse was carried out at about 3.3 meters downstream from the trip (i.e. $Re_x \approx 5.72\times10^5$), which was exactly the streamwise location that the first slit was placed in the visualization experiments. The measured velocity profile was used to indicate the internal consistency of the measurements as well as to obtain the flow parameters at the measuring station. Figure 3.1 shows the dimensional velocity profile plotted as the mean streamwise velocity versus the distance from the wall. The momentum thickness was computed using trapezoidal rule of integration. Since obtaining data very close to the wall was constrained by the physical size of the probe, the shear stress at the wall was unable to be estimated reliably from the slope of the sublayer profile. Therefore, determination of the friction velocity was made using the Clauser plot technique (1954), in conjunction with Coles (1968) law of the wall. This technique is good to ±5% based upon the comparison of drag balance measurements and the Clauser plot.

Examination of Figure 3.1 indicates that two measurements near the intermittent region of the boundary layer appeared not to be in good agreement with the overall profile. The cause of this inconsistency is, however, not well understood. Since the positions of these two data points are well beyond the log region, they definitely have very little effects in the decision of the skin friction coefficient from the Clauser plot. Figure 3.2 shows the utilization of Clauser plot in determining the skin friction coefficient. Using friction velocity based upon the chosen skin friction coefficient, the universal logarithmic mean velocity profile is presented in Figure 3.3. It shows that the flow at the measuring station satisfactorily complied with the behavior of a normal turbulent boundary layer flow over a smooth wall. A summary of the principal characteristics of the flow at the measuring station is given in Table 3.1. As we can see, the shape factor of our boundary layer flow ($H \cong 1.27$) was very close to the theoretical value ($H=1.3$) for turbulent flat-plate flows at low Reynolds numbers as suggested by White (1986). Note that the thickness of the viscous sublayer was approximately 0.7 mm.

The accuracy of the measurements was checked using the matching condition at the free surface. By comparing the mean value of the measurements using surface floats and the mean value of the measurements for $y>\delta_{99}$ using pressure probes, we found that the relative difference between them was about 5.1% of the average free stream velocity based upon the pressure measurements. Calculations are described in Appendix A.

3.2 Statistical Results

3.2.1 Limitation of What Our Data Can Tell

Before the statistical results are presented, it is important to know what information our visual data are able to provide. The experiment is designed to measure the following :

--- physical size and spatial relationships of coherent motions.

--- velocity of a coherent motion as a whole.

--- frequency of occurrence and temporal relationships between coherent features.

Because a passive dye technique was employed, we will not be able to obtain quantitative information about the :

--- vorticity or pressure field (however, in some cases their relative intensity can be qualitatively deduced).

--- fluctuations in any direction.

In addition to the time-space measurements that can directly reveal important physics, there are few hypotheses (inferences or suggestions) that will be made, mainly presented in next chapter, based upon piecing together the visual evidence and statistical results. Note that a statistics concerning the creation and the evolution of hairpin vortices has not been compiled, partially because the insufficient resolution of our visual data is incapable of consistently showing small hairpins with vortex filament of Kolmogorov scale. More importantly, its formation is not the major interest of this study as mentioned earlier.

3.2.2 Typical Eddies

The statistical characteristics of typical eddies will be presented in this section. Regarding the observation of the typical eddies, one should bear in mind that the formation and evolution of the typical eddies were occurring in a highly perturbed environment, thus it is unrealistic to expect that typical eddy with idealized shape, such as an undistorted laminar vortex ring, could constantly be seen. Particularly in the cross-stream view (y-z plane) study, not only are typical eddies with unperturbed shapes rare, but also are they not easy to be distinguished as they are in the side view (x-y plane). In order that we could correctly identify typical eddies from the cross-stream view, preliminary exercise had been made. That is, we had repeatedly practiced viewing the typical eddies in the simultaneous laser sheets parallel and normal to the mean flow direction as the eddies passed the intersection of both laser sheets.

According to the rules of conditional sampling described in Section 2.5, the typical eddies were essentially sampled unconditionally (i.e. a typical eddy was sampled as long as it was visually identified) except that the eddy must have occurred within the first 300 wall layer units.

3.2.2.1 *Magnitude*

Dimensions of typical eddies in the outer intermittent region have been measured over a wide range of Reynolds numbers by Falco (1991). Figure 3.4 shows the average length scale of the diameter of the vortex core in dimensionless form (see the definition sketch in the figure) as a function of Reynolds number. Figure 3.5 shows two similar plots as the mean dimensions of typical eddies are normalized by the momentum thickness and wall variables. Observation of both figures indicates that the magnitude of typical eddies decreases as Reynolds number increases when non-dimensionalized by boundary-layer thickness or momentum thickness, and increases with Reynolds number when scaled on wall variables. However, no one has ever revealed the length characteristic of typical eddy at its cross-stream section (i.e. y-z plane). Finding the characteristics of this dimension is very desirable because important sublayer features such as pockets and low-speed streaks are normally characterized by their spanwise dimensions, thus, for consistency, to describe their relationships with the typical eddy using its spanwise dimension is more adequate than using C_y or C_x.

For the current work, a significant number of samples have been gathered to compute the typical-eddy diameter (maximum dimension) in the cross-stream section at $R_\theta \approx 805$. For convenience, we will denote this length scale as C_z hereafter. In the experiments, the most common coherent motions with size of Taylor micro scale observed in the cross-stream laser plane were counter-rotating vortex pairs and crescent-shaped features in the dye. The sampled vortex pairs and crescent-shaped features are considered as ring-like vortices (i.e. typical eddies). An explanation for this will be made later when the streamwise extent (C_x) of the samples is examined. Figure 3.6 shows the definition sketch as well as the probability density distribution of the spanwise diameter of the typical eddies in wall layer units. The probability density functions of the log-normal and the normal distributions based upon the statistical parameters of the data set are also shown. In the present study, the probability density functions of various distributions for discrete random variables are given in Appendix D. The statistically significant properties of C_z^+ distribution, such as the sample size, mean, mode, standard deviation, variation coefficient, as well as skewness and flatness coefficients are tabulated in Table 3.2 as shown below. It appears that the log-normal distribution, with a typical dense range from 60 to 170 wall layer units, represents the overall data better than the normal distribution.

Table 3.2 Characteristics of C_z^+ distribution as shown in Figure 3.6

Characteristic	N	Mean	Mode	σ	ψ	S	F
Value	417	101.3	87.5	24.9	0.25	1.32	6.56

The streamwise length scale (C_x) of the typical eddy is also estimated by counting the number of frames that the typical eddy had appeared consecutively in the cross-stream view. Based upon preliminary side-view observation, the typical-eddy convection velocity was found to be, on average, close to the local mean velocity. Therefore, the approximate convection velocity of a typical eddy can be obtained by using the known distance of the typical eddy from the wall to find the corresponding mean velocity in Figure 3.1. The streamwise length scale of the typical eddies is computed by the formula

$$C_x = (\text{local mean velocity}) \times (\text{number of frames}) \times (\text{framing rate})^{-1}$$

Figure 3.7 shows the definition sketch and the probability density distribution of C_x in wall layer units. Table 3.3 lists the statistical parameters of the data. In a manner analogous to the behavior of C_z^+, the overall data are well represented by a log-normal density function. This set of data is very important although they represent estimated values. It confirms that our samples were not long axial vortex pairs, but conforms well with the expected compact vortical shape with which typical eddies are characterized. Additionally, since the sampled vortex pairs were dyed florescent green, they were not hairpin vortices that had long legs attached to the wall. Based upon these findings and the fact that the vortex lines must have closed on themselves, the simplest hypothesis for the coherent shape of the sampled vortex pairs is that they were ring-like vortices. The joint probability density of random variables C_z^+ and C_x^+ is graphically presented in both a two dimensional contour map as well as a 3-D probability density distribution as shown in Figure 3.8. The peak occurrence is clearly located at the neighborhood of $C_z^+=92$ and $C_x^+=73$.

Table 3.3 Characteristics of C_x^+ distribution as shown in Figure 3.7

Characteristic	N	Mean	Mode	σ	ψ	S	F
Value	417	76.9	72.5	30.2	0.39	0.73	3.28

3.2.2.2 *Correlation of Diameter and Distance From the Wall*

The distance of a typical eddy from the wall (d) is defined as the distance between the center of the typical eddy and the wall. Figure 3.9 gives the definition sketch in the y-z plane and the probability density distribution of the distance (d) in wall layer units. Table 3.4 tabulates the statistical characteristics of the samples. The various dashed lines represent the normal, log-normal, as well as the Rayleigh probability density functions. It appears that the length scale d^+ is close to be a random variable of a log-normal distribution with a mean of approximately 118 wall layer units. It is also found that the most probable distance of the typical eddies from the wall were slightly under $y^+=100$ when propagating over the near wall region.

Table 3.4 Characteristics of d^+ distribution as shown in Figure 3.9

Characteristic	N	Mean	Mode	σ	ψ	S	F
Value	417	117.9	97.5	42.26	0.36	0.71	3.45

In the scaling analysis, the relationship between the spanwise diameter (C_z) of a typical eddy and its distance from the wall has also been explored. Figure 3.10 shows the dependence of C_z^+ on d^+. The data are obtained by performing several binning processes, with various bin widths, on both variables. Sample size is 417. Along with the data, the histogram of d^+ and upper/lower standard deviation boundaries of C_z^+ are also presented to show the degree of data dispersion. The results indicate that the spanwise length scale of the typical eddies gradually increases as their distance from the wall increases. This is expected if the formation process of the typical eddies and the diffusion of their vortex cores are the primary causes of this scaling dependence (more comments will be made in Chapter 4). The findings also serve as an evidence against the conjecture that the pairing process of typical eddies is important in the outer part of turbulent boundary layers. Furthermore, a reasonable linear relationship between these two length scales is found to exist over the range of $55<d^+<280$ as shown in Figure 3.11. The linear approximation is written as follow.

$$C_z^+ - 0.097d^+ - 88.6 = 0$$

A normalized distance (d^*), defined as $d^+ - 0.5C_z^+$, is also statistically characterized here although its use is not immediately revealed at this point. This scale provides an approximate measure that stands for the distance between the lower boundary of the vorticity concentration of the typical eddy and the wall. The accuracy of this estimated scale mainly depends on the orientation of the typical eddy with respect to the wall in the x-y plane. Figure 3.12 presents the probability density distribution of d^* and the normal, log-normal, as well as the Rayleigh probability density functions. The statistically significant properties of the data set is tabulated in Table 3.5. It is found that, among these three probability density functions, the Rayleigh distribution is obviously the best curve fit for the data set. Utilization of this length scale will be shown in Section 3.2.6.

Table 3.5 Characteristics of d^* distribution as shown in Figure 3.12

Characteristic	N	Mean	Mode	σ	ψ	S	F
Value	417	67.47	43.75	41.36	0.61	0.74	3.29

3.2.2.3 *Comparison with Outer Layer Data*

Table 3.6 shows the comparison of the present $C_z/2$ and C_x measurements with Falco's data, which were measured in the outer intermittent region by side-view observations, at a comparable Reynolds number. The data are compared in dimensionless forms as normalized by variables u_τ/ν and θ. The definition sketch for each scale is also provided. It shows that the current data are in good agreement with Falco's measurements although there is minor difference in scale definition (see the definition sketches for Falco's C_x and C_y). Qualitative comparison of these data demonstrates that the selected samples using cross-stream observations were typical eddies. Furthermore, because both side view and cross-stream views have the configuration drawn, we also confirm observations that typical eddies are indeed ring-like. Their toroidal conformations led to the appearance of counter-rotating vortices as they passed through the transverse laser sheet. Quantitatively, this comparison shows that the data are consistent with the trend that the size of typical eddies increases with distance from the wall. This is because that although $C_z/2$, the half spanwise diameter of the typical eddy, is comparable to C_y, the diameter of the vortex core in the x-y plane, $C_z/2$ should have been greater than C_y if measures were taken out of the same typical eddy. However, the results show a nearly identical mean value of $C_z/2$ and C_y for typical eddies in the two distinct regions of the turbulent boundary layer. The indication is clear that the length scales of the outer-layer typical eddies are, on average, larger than that of typical eddies existing close to the wall. The interpretation may also be made by the following mathematical expressions.

Since $C_z/2 \geq C_y$, for same typical eddy (T.E).

the comparison shows $(C_y)_{\text{outer T.E}} \cong (C_z/2)_{\text{inner T.E}}$

result in $(C_y)_{\text{outer T.E}} \geq (C_y)_{\text{inner T.E}}$

By similar interpretation, the comparison of our estimated C_x and Falco's measurements will simply result in the same conclusion. Additionally, the flow-visualization measurements of Hoyez (1990) also confirmed that statistically the diameter of typical eddies in the x-y plane increases with distance from the wall. Similar results are drawn although her samples were taken in the upper portion of the outer region at moderately high Reynolds numbers.

Examination of Table 3.6 suggests that, for Reynolds numbers in the order of the present experiment (O1000), the typical eddy normally has an axisymmetric donut-like configuration with diameter of the Taylor micro-scale (~100 wall layer units) and streamwise span about 75% of the diameter.

3.2.2.4 *Orientation*

In the laser sheet cross-stream observations, we have also measured the typical-eddy orientation, which was characterized by the angle (ϕ), ranging from $-\pi$ to π, between positive y axis and the typical-eddy axis. The measurements were taken when the maximum dimension of the typical eddies appeared in the laser plane. The definition sketch and probability density distribution are shown in Figure 3.13. The dashed line stands for the probability density function of a normal distribution. Table 3.7 lists the statistical properties of the data set as shown below. In this measurement, the error bar is ±2.5 degrees since the data were recorded by units of 5 degrees. As we can see, the normal distribution provides a fairly good curve fitting for the samples. This is also confirmed by the small skewness coefficient and relatively high flatness coefficient shown in the table. Results indicate that, within the first 300 wall layer units of turbulent boundary flows, the most probable orientation of typical eddies in the y-z plane is almost identical to their average orientation, which is approximately zero degrees. Incidentally, the symmetrical distribution demonstrates the excellent quality of the water tunnel flow which kept the mean lateral flow fluctuations negligible (i.e. $\overline{\partial(\ )/\partial z} \approx 0$) in the measuring station throughout the experiment.

Table 3.7 Characteristics of ϕ distribution as shown in Figure 3.13

Characteristic	N	Mean	Mode	σ	S	F
Value	417	-1.65°	0°	32.96°	0.27	6.60

By examining the sequential cross-stream views of a typical eddy, its orientation with respect to the wall in the x-y plane could also be deduced. Based upon their inclinations with the wall in x-y plane, typical eddies are divided into six category of orientations. Each category of orientation will be called a "*mode*". Figure 3.14 illustrates four of the six different *modes* of typical eddies in both side and cross-stream views as they are propagating past a transverse laser sheet. The sketched sequencing of the cross-stream views associated with each *mode* of the typical eddies shows how we managed to obtain their *modes*. It is noted that the figure illustrates an idealized scenario, and the real case is unlikely to be as regular and clear-cut as the sketch might indicate. We must anticipate the real pictures to be complicated because of the distortion by highly perturbed environment and complex typical eddy interaction, as well as the smearing effect of diffusion. Typical eddy of *Mode* 5 is defined as the transition stage from *Mode* 1 to *Mode* 2. In other words, the change of the typical eddy elevation was very small, essentially not measurable in the cross-stream view sequence (i.e. the self-induced velocity vector was pointing outwards and normal to the wall in the side view when crossing the transverse laser plane). Similarly, typical eddy of *Mode* 6 is defined as the transition stage from *Mode* 3 to *Mode* 4.

The statistical characteristics of typical eddies based upon their *modes* are presented in Table 3.8. Total sample size is 417. The first three columns of the table give the distribution of typical eddies in different *mode* categories. The length-scale properties associated with each *mode* are also tabulated in columns 4 and 5 (discussion concerning the rest of the table will be made later in this chapter). Examination of the table suggests that not only did *Mode* 1 represent the most probable geometrical orientation in the x-y plane, but also were typical eddies of this *mode*, on average, the closest ones to the wall. On the other hand, the occurrence of typical eddies of *Mode* 4 or 6 was almost nonexistent (less than 1%). In general, the majority of the typical eddies were oriented so that they induced themselves away from the wall (i.e. 97.9% of the typical eddies were *Modes* 1, 2, and 5).

Earlier, we have measured the mean spanwise diameter (C_Z) and estimated mean streamwise length scale (C_X) of the typical eddies. Therefore, the average inclination angle with the wall of *Mode*-1 typical eddies in the x-y plane can be calculated by the term, $\mathrm{Cos}^{-1}(76.9/101.3)=40.6$ degrees, assuming that the typical eddies on average had axisymmetrical forms. The denominator and numerator of the operand stand for the average diameter and the mean streamwise length of *Mode*-1 typical eddies respectively. By comparing this to the characteristic angle (about 45 degrees) of hairpin vortices as suggested by Head and Bandyopadhyay (1981), it is not difficult to realize how easily these two structural features could be misinterpreted in the x-y plane, and how closely the relationship they might have with regard to the evolution of wall region hairpins and the formation of typical eddies. Further discussion concerning a possible link between hairpin vortices and typical eddies will be made later.

3.2.2.5 *Period of Occurrence*

The time between typical eddy occurrences is one of the important features associated with the turbulent boundary layer dynamics, especially for these sampled typical eddies which were close to the wall (for $y^+<300$) having direct impact on the wall-region turbulence production. The period of occurrence (t_{TE}) was able to be measured by viewing the cross-stream view and recording the time at which typical eddies passed a pre-chosen measuring station. The station was an imaginary line which extended from the wall to $y^+=300$. It is noted that a typical eddy was counted if any portion of it crossed the imaginary line. Since a typical eddy usually required more than one frame to cross the measuring station, we regulated our time recording scheme so that the time was marked when the center of a qualified typical eddy appeared in the transverse laser plane (i.e. time was recorded when its spanwise dimension was maximum). If more than one typical eddy were crossing the imaginary line simultaneously, only one sample was counted. In order to have a large enough sample size, two measuring stations within the spanwise laser sheet had been selected to perform the investigation. They were separated by $300z^+$ to ensure the independence of the selected samples. Figure 3.15 shows the probability density distribution of t_{TE}'s in viscous time units, as well as the log-normal and Rayleigh probability density functions. The principal properties of this set of samples are listed in Table 3.9. It is found that the highly skewed probability density distribution of t_{TE}^+ is better represented by a log-normal density function with a mean of nearly $26t^+$.

Table 3.9 Characteristics of t_{TE}^+ distribution as shown in Figure 3.15

Characteristic	N	Mean	Mode	σ	ψ	S	F
Value	157	26.3	11.3	24.2	0.92	2.27	9.34

The average period of the typical eddy occurrence can be normalized by the boundary layer thickness and the average convection velocity of the sampled typical eddies, δ_{99}/U_{avg}. Note that the value of U_{avg} is calculated using the local mean velocity (Figure 3.1) based upon the mean d^+ of the typical eddies (Table 3.4). The resultant value is about 1.1 which suggests that, on average, one typical eddy in the log region or lower portion of the outer region could be seen by a stationary observer about every boundary layer thicknesses at low Reynolds numbers. Again, we approximate the mean convection velocity of a typical eddy to be the local mean velocity about its center of mass.

3.2.2.6 *Center-to-Center Spanwise Spacing*

In many visual studies of sublayer features, it has been noticed that the chances for witnessing the formation of a row of pockets along a spanwise direction in the immediate downstream of the wall slit are high. It is felt that the cause of this phenomenon should have been related to the lateral distribution of the excitation coherent motions in the log region and/or lower portion of the outer region. Thus, an important feature of the typical eddies which needs to be quantified is the characteristic dimension of their spanwise spacings. The data base for this investigation has been constructed by selecting the samples in which more than one typical eddy appeared simultaneously in the cross-stream view. If the centers of two typical eddies happened to be aligned vertically in a chosen sample, they were counted as one typical eddy in order to eliminate the possibility of zero spacing, which is meaningless for the purpose of this measurement. In fact, examination of the chosen samples indicates that the minimum distance between two typical eddies was about 56 z^+. Figure 3.16 shows the probability density distribution of center-to-center spacings (ξ^+) between neighboring typical eddies in the spanwise direction. The normal, log-normal, and the Rayleigh probability densities are also sketched to represent the distribution. Although none of these distributions represents the data perfectly, it appears that the log-normal density function fits the overall distribution better than the other two. The principal properties of the data set are listed in Table 3.10. It indicates that the typical eddies were, on average, spaced in the spanwise direction by roughly 0.6 boundary layer thicknesses. Note that, although the sample size is 84, there were 156 typical eddies involved in the analysis because each sample usually consisted of two or three typical eddies.

Table 3.10 Characteristics of ξ^+ distribution as shown in Figure 3.16

Characteristic	N	Mean	Mode	σ	ψ	S	F
Value	84	244	128	132	0.54	0.76	2.86

Using this spanwise spacing characteristic of the typical eddies, an argument will be presented later to reconcile the difference between the mean spacing of the sublayer streak pairs found in the present interaction study and the overall spacing of the low-speed streaks in turbulent boundary layers.

3.2.3 Long Sublayer Streaks

The low-speed, long streaky structure is an important feature in the wall region of wall bounded turbulent flows. It is well known that the average spacing (λ^+) of these streaky structures is about 100 when non-dimensionalized by wall variables. It was also documented that sublayer streaks with longitudinal length greater than 1000 wall layer units exist. Furthermore, once formed the streaks were observed to persist for very long time. Although the mechanism responsible for the formation of the long sublayer streaks has not been fully uncovered at this stage, previous observations suggested that the long sublayer streaks are formed in pairs as results of inner/outer region interactions.

3.2.3.1 *Spacing of Neighboring Long Streaks (Unconditionally Sampled)*

The characteristic length scale of long sublayer streaks is represented by its spanwise spacing (λ) between two neighboring streaks. In the current study, the method of measuring this length scale was to measure the spanwise distance between the centers of two neighboring streaks at a transverse measuring station located approximately $50x^+$ downstream of the second wall slit. It was required that the streaks had well defined outline (i.e. clear distinction of dye concentration) and streamwise extent of at least 100 wall layer units when sampled. If two streaks appeared to merge within $100x^+$ downstream from the measuring station, they were counted as one streak; otherwise, there was no preset minimum spacing. The film that contains only plan view was used to perform the streak counting. Each frame in the film was spaced by $1.84t^+$. We evaluated the streak spacings in still pictures that were evenly separated by $130t^+$ (i.e. 70 frames apart) in order to obtain statistical information of independent streaks. The total duration of investigation was approximately $7280t^+$.

Figure 3.17 shows the probability density distribution of λ's in wall layer units as well as the normal and log-normal density functions. Table 3.11 tabulates the statistical parameters of the samples. Results show that the overall data is very well represented by a log-normal density function with most streak spacings occurring between 40 and 170 wall layer units. Our data confirm the overall streak spacing measured previously by Kline et al. (1967) and many other investigators. The statistical parameters of our streak spacing distribution are also very similar to those determined by Smith and Metzler (1983; $0.75<S<1.0$, $0.34<\psi<0.4$) using hydrogen bubble technique and Oldaker and

Tiederman (1977; ψ=0.36) using dye visualization. The most probable value of the streak spacing (the Mode) is also consistent with the findings of Smith and Metzler (75~80z^+) and the value (about 20% less than the mean) suggested by Kline et al. (1967).

Table 3.11 Characteristics of λ^+ distribution as shown in Figure 3.17

Characteristic	N	Mean	Mode	σ	ψ	S	F
Value	500	96.0	78.5	34.9	0.36	0.91	4.44

3.2.3.2 *Spacing of Conditionally Sampled Long Streak Pairs*

In the section, we will present the spanwise length characteristic of the long sublayer streak pairs which were selected according to the rules of the conditional sampling (Section 2.5). The characteristic length of a streak pair is represented by its spanwise spacing (l) between the streaks. In the present study, the method of measuring this length scale was to measure the average spanwise distance between the centers of the two streaks, whose widths normally ranged from one to four Kolmogorov micro-scales. Figure 3.18 shows the measuring scheme and the probability density distribution of l's in wall layer units. The normal and log-normal density functions are also sketched. Table 3.12 gives the statistically important properties of the samples. It is found that the overall data is well fit by the log-normal density function with relatively small skewness and variation coefficients. Most of the samples ranged between 40 and 120 wall layer units. The mode is only about 6% less than the mean.

Table 3.12 Characteristics of l^+ distribution as shown in Figure 3.18

Characteristic	N	Mean	Mode	σ	ψ	S	F
Value	291	74.7	70	15.7	0.21	0.86	4.78

The conditional sampling of the streak pairs leads to the apparent disagreement in the wall-region mean streak spacing between our result (about 75 wall layer units) and the universal length scale (about 100 wall layer units). However, the results are different simply because they are two sets of data which were taken under different measuring rules. In the present experiment, the samples of the long sublayer streak pairs were conditionally selected based upon the occurrence of pockets in the sublayer or typical eddies in the log region and lower portion of the outer region. It is important to emphasize that the classical scheme used to deduce an average spanwise streak spacing was to count, from the motion pictures, the number of streaks in a number of statistically independent frames. The classical method of streak counting was not conditioned by the occurrence of other structural features on and/or above the wall. It is interesting to note that the streak spacing measurements using the classical method (Smith and Metzler 1983, as well as our application of the classical method, i.e. our unconditionally sampled data) resulted in a log-normal distribution having a mode nearly identical to the mean of our conditionally sampled streak pair spacings.

It is worth noting that when we use the term "streak pair", we are not necessarily implying that the length in streamwise direction of one streak must equal that of the other. In many visual studies concerning wall region features, single streaks could be observed occasionally because one of the streaks was longer than the other. Another possibility is that the confined dye-marking region prevented one of the streaks from being observed. The length that a streak was able to extend might depend on many factors such as the incident angle and the orientation of the excitation eddy, as well as the existing local conditions in the wall region. Hereafter, the phrase "streak-pair spacing" (l) is used to denote the spanwise spacing of a streak pair which is identified to be associated with the occurrence of a typical eddy or a pocket. On the other hand, the words "streak spacing" (λ) is still used to denote the lateral spacing between neighboring streaks. Further discussion on the wall-region streak spacing, involving the information obtained in Section 3.2.2.6, are made in Chapter 4.

3.2.4 Pocket

The pocket flow module is an important feature of the wall region structure that is clearly present close to the dye slit. It is necessary to have sufficient concentration of markers covering an area over the wall to visually detect them. Pockets were difficult to observe further downstream (> 400 x^+) from the wall slit because most of the dye would have been diluted and/or convected away from the wall. Falco (1980) documented the formation and evolution of pockets in detail. He also showed that, as the Reynolds number increases, the spanwise dimension of pockets increases slowly when non-dimensionalized with wall parameters. In this section, we will describe the length characteristic and the occurrence frequency of the pockets based upon the present set of samples.

3.2.4.1 *Length Scale*

The length scale of a pocket is characterized by its maximum width (w) as the fully developed stage has reached. In the present study, the method adopted for measuring this characteristic length was to measure the spanwise distance between the most densely marked boundaries of the pocket. Figure 3.19 shows the definition of pocket measurements, the probability density distribution of w^+'s, as well as two probability density functions. The statistical parameters of the samples are tabulated in Table 3.13. Apparently, the behavior of the pocket width conforms closely to a random variable of a log-normal distribution having a mean of about 82 wall layer units. Most of the samples are found to range between 50 and 130 wall layer units. Further examination of the table indicates that the skewness, flatness, and the variation coefficients are very similar to those of the streak pair spacing as shown in Table 3.12. Figure 3.20 presents the comparison of the average pocket width between the current data and the outcomes of some previous experiments in a log-log scale. It shows that our data is well in the range of the measurements of many others.

Table 3.13 Characteristics of w^+ distribution as shown in Figure 3.19

Characteristic	N	Mean	Mode	σ	ψ	S	F
Value	195	81.8	75	17.6	0.22	0.93	4.08

3.2.4.2 *Period of Occurrence*

In experiments designed to examine only the wall region (i.e. using the film containing only plan view), the measurement of the time (t_p) between pocket creations has been carried out. The counting scheme employed to determine the frequency of pocket occurrence is similar to that of counting typical eddies as described in Section 3.2.2.5. The pockets were counted when they crossed the measuring station which was a pre-chosen imaginary point located at about 120 x^+ downstream of the second wall slit. In order to collect a large enough size of samples, three measurement positions have been adopted. They were about 275 wall layer units apart in the spanwise direction, so that the pockets detected at each of these measuring stations provided independent data for the ensemble average.

The probability density distribution of t_p's, in dimensionless form, and two density functions are shown in Figure 3.21. It is found that the distribution of t_p^+'s is better represented by a log-normal density function with a mean of approximately 30. Table 3.14 lists the principal characteristics of the samples, indicating that the data exhibit a manner analogous to that of the occurrence period for typical eddies which propagated over the near wall region (see Table 3.9). It appears that both the t_P^+ and t_{TE}^+ have distributions conforming to log-normal behavior, which are highly skewed to the region of greater value than the mean. The slight difference of the expectation values is due to the fact that a portion of the typical eddies did not have strong interaction with the wall layer leading to pocket formations. Figure 3.22 presents the comparison of the mean t_P^+ between the current data and the results of some previous experiments in a log-log scale. It shows a good agreement with the recent data measured over a smooth wall at R_θ close to 800 (Yoo 1990).

Table 3.14 Characteristics of t_P^+ distribution as shown in Figure 3.21

Characteristic	N	Mean	Mode	σ	ψ	S	F
Value	183	29.8	13.5	24.3	0.82	1.91	6.97

3.2.5 Length Scale Correlations

3.2.5.1 *Typical Eddy and Sublayer Streak Pair*

Samples in which both a typical eddy and a sublayer streak pair occurred simultaneously are gathered to examine their length-scale correlation. Figure 3.23 shows the correlation of the streak-pair spacing and the spanwise diameter of the typical eddy, plotted as l^+ versus C_z^+, as well as the histograms of both scales. Sample size is 273. The data indicate that, in addition to the correspondence of streak pair spacing and typical eddy mean scales (the typical eddy is slightly larger than the streak pair it creates), statistically the spacing of sublayer streak pairs increases as the physical size of the corresponding typical eddies increases.

For comparison, subset of the data obtained from the ring vortex/moving wall simulations (Chu and Falco 1988) for 3 degree incident angle and Stokes layers of thicknesses ranging between 32 and 47 viscous units are also presented in the figure. Note that the simulation data in which both the diameter (D) of ring vortex and the streak-pair spacing (l^+) that were greater than 200 viscous units are not shown, simply because the nature seldom or never creates those situations for the Reynolds number on the present experiment. Since the simulation results provided data of l^+ against D^+, it is important to display them in the current coordinates. In the present set of samples, C_z of typical eddy was measured after the onset of the interaction (recall that the transverse laser plane was set downstream of the designated area). On the other hand, the diameter of the ring vortex (D) was recorded at the time when it was generated as an axisymmetric form. It is rational to believe that the ring vortex would have not been as symmetrical as it had been when it impinged the wall and stretched the lower part of the vortex laterally. Additionally, if the diffusion effect ($\sim\sqrt{\nu t}$) is also taken into account, although it might be small in this case, the diameter of the ring vortex would have been increased. Accordingly, one would expect that a corrected comparison would involve shifting the simulation data to the right (i.e. towards large value of C_z^+) to some degree when fitting into the coordinates of Figure 3.23.

However, examination of both correlations suggests that they were similar events (in the sense of interaction mechanism) in spite of that the details between the turbulent boundary layer and the laminar simulation were appearing significantly different. The trend of our correlation conforms well with that of the simulation data in the neighborhood of the peak occurrence and the region below it. Nevertheless, in the region of greater typical eddy size (for instance, $C_z^+>120$), the rate of growth for the corresponding streak-pair spacings falls short when compared to the simulation data. An important reason contributing to this is that those typical eddies of greater size were also, on average, located with greater distance from the wall in the turbulent boundary layer experiment. Therefore, the local wall areas underneath them being influenced were correspondingly smaller than the dimensions of the typical eddies. In the physical simulations, ring vortices of any size were, however, able to be forced to convect over regions adjacent to the wall. Furthermore, our experiments have been carried out in a much more perturbed environment than that of the physical simulations. The higher strain rate and lateral disturbance could have predominantly governed the shape and evolution of the sublayer features. For example, the spanwise 'stretch' of a developing streak pair, resulting from a large typical eddy convecting over the wall, could have been constrained if another typical eddy was also creating sublayer features to the side of it but in the same neighborhood. Contrarily, in the physical simulations, the wall-layer features were able to form freely in the absence of the side perturbations. Intuitively, it is believed that the constraints on the spanwise spacings of streak pairs due to the lateral disturbances will be more severe on the events of greater size than on the smaller ones. Coincidentally, our results also show this trend.

Figure 3.24 shows the 2-D probability density contour map as well as the 3-D probability density distribution of random variables, l^+ and C_z^+. It appears that the peak occurrence is located at $C_z^+\approx 92$ and $l^+\approx 72$. Figure 3.25 shows the dependence of the streak-pair spacing on the spanwise diameter of the typical eddy at $R_\theta \approx 805$. The reduced data are obtained by grouping the samples based upon the binning, with various bin widths, of C_z's. The figure also shows that a linear approximation reasonably fits,

(

s

ty

ec

po

ed

sub

C_z

bou

stra

data

rela

particularly in the high occurrence region, between l^+ and C_z^+. The linear relationship is written as follow.

$$l^+ = 0.29\, C_z^+ + 45\,, \quad \text{for } 50 < C_z^+ < 200$$

3.2.5.2 *Typical Eddy and Pocket*

Analogous to the previous analysis, samples in which both a typical eddy and a pocket occurred simultaneously were collected to examine their length-scale correlation. Figure 3.26 shows the dependence of the pocket size (w^+) on the spanwise diameter (C_z^+) of the typical eddy, as well as the histograms of both scales. Sample size is 173. The data were smoothed by performing several binning processes based upon C_z^+. Observation of the data indicates an apparent correlation existing between w^+ and C_z^+. It shows that statistically the pocket size increases as the physical size of the corresponding typical eddy increases. Moreover, it demonstrates a trend similar to that of the typical eddy/streak pair correlation depicted in Figure 3.25, although the growth rate of the pocket size is slightly greater than that of the streak-pair spacing for the larger typical eddies. The argument presented in previous section to explain why the size of the sublayer streak pairs did not grow as much as the size of the typical eddies in the large C_z region is also applied here for the pocket formations. At this point, we can see that both the streak pairs and the pockets are strongly correlated with the typical eddies. The straight line in Figure 3.26 represents the first order least square approximation of all raw data (un-binned data), which gives a reasonable fit between w^+ and C_z^+. The linear relationship is written as follow.

$$w^+ = 0.355\, C_z^+ + 46.5\,, \quad \text{for } 50 < C_z^+ < 200$$

Figure 3.27 shows the 2-D probability density contour map as well as the 3-D probability density distribution of random variables, w^+ and $C_z{}^+$. The peak occurrence is located at $C_z{}^+ \approx 89$ and $w^+ \approx 69$.

3.2.5.3 *Pocket and Sublayer Streak Pair*

Samples in which both a pocket and a sublayer streak pair occurred simultaneously, with the condition that a typical eddy was simultaneously propagating over the wall above them, were gathered to examine the length-scale relationship between the pocket and the sublayer streak pair. Figure 3.28 shows the correlation data, plotted as w^+ versus l^+, and the histograms of both scales. Sample size is 149. A fairly strong grouping is apparent. It also indicates that the majority of the data participate in a trend except two samples that are located in the region of l^+/w^+ ratio close to a factor of 2. Figure 3.29 shows the 2-D probability density contour map as well as the 3-D probability density distribution of random variables, w^+ and l^+. It is found that the peak occurrence is located at $l^+ \approx 71$ and $w^+ \approx 75$.

It is frequently helpful in analysis to search for an expression in describing a given set of data. Nevertheless, care must be taken to find such an expression since the present set of data is not a monotonically ascending or descending function based upon either scale, thus the binning or curve fitting based upon either scale as the independent variable will result in very different outcomes. Referring to Figure 3.28, two straight dashed lines stand for the first order least squares fits of the data using either scale as the independent variable (l^+ for the line with lower slope and w^+ for the other). It is found that both of the linear fits are biased, failing to represent the overall trend of the data set satisfactorily. This is because that use of only l^+'s and w^+'s results in mathematical representations which are totally blinded to a third feature that governs the two scales. In this case, the proper way to accomplish the correlation is to utilize the individual length-scale correlations of each feature (the pockets and the long streak pairs) with the typical eddy, which is responsible for the formation of these sublayer features. Referring to Sections 3.2.5.1 and 3.2.5.2, the expressions of l^+ and w^+ as functions of C_z^+ have been established. Therefore, the correlation of the pocket size and the streak-pair spacing, under the condition that a typical eddy was observed to convect over the wall above them, is readily derived as follows:

$$w^+ = 1.225\, l^+ - 8.6\,, \quad \text{for } 30 < l^+ < 150\,;\ 30 < w^+ < 140$$

It is very important to emphasize that this expression can not be obtained by solely using the information of w^+ and l^+. The above linear representation is also plotted, as a solid straight line, in Figure 3.28. It appears to be the best fit among these three linearities with regard to the overall trend of the scattered data. This evidently shows that the information about the typical eddy is required when characterizing the relationship between the sublayer streak pairs and the pockets. Examination of the linear representation suggests that the lateral dimension of both sublayer features are almost identical in the vicinity of the peak occurrence and the region below it. In the region beyond the peak occurrence, the pocket size gradually becomes greater than the streak-pair spacing.

Figure 3.30 shows the same linear representation and a data set that comprises samples in which both the sublayer features were formed in the absence of a typical eddy occurrence. Sample size is 18. It is interesting to note that this data set appears to conform well with the trend of its complementary data. This indicates that these sublayer events might have also related to typical eddies. A hypothesis suggesting why we were unable to identify the initiating motions is that they lost their characteristic structures or distorted significantly due to the interactions before the observation station.

3.2.6 The Effects of Typical Eddy Distance From the Wall

3.2.6.1 *On the Overall Length Scale Correlation*

It is understood that the distance of a typical eddy from the wall is also capable of affecting the length scale of the sublayer feature(s) that it creates. In this section, samples which contain all the three coherent features (i.e. simultaneous occurrence of a typical eddy, as well as a pocket and an accompanying streak pair) are analyzed to uncover their overall scaling correlation, including the distances of typical eddies from the wall. Figure 3.31 shows the dependence of the pocket size (w^+) on both the distance (d^+) and the normalized distance (d^*) of the typical eddy from the wall. The histogram of w^+ as well as the upper/lower standard deviation boundaries for d^+ and d^* are also provided to show the degree of the data dispersion. In addition, the average spanwise scales of the corresponding typical eddies and the sublayer streak pairs, $C_z{}^+$ and l^+, for each data point are listed near the top of the figure (standard deviation in brackets). Total sample size is 149.

Examination of the data based upon d^+, one could be misled by the fact that the pockets and the sublayer streak pairs (see l^+'s near the top of the figure) of greater dimension were, on average, associated with typical eddies positioned further away from the wall. It is necessary to recall that these typical eddies of greater distance from the wall also, on average, possessed greater physical size. This, however, raises the question: What is the criterion of the maximum distance (d^+) in which a typical eddy is able to create biggest sublayer feature(s), or is simply too far away from the wall to make any disturbance at all? The ambiguity between the distance of the center of a typical eddy to the wall and the distance from the "bottom" of the typical eddy to the wall for different size eddies can be resolved by introducing a normalized parameter d^* (i.e. d^+-$0.5C_z^+$) which takes the magnitude of the typical eddy into account. In the same figure, the data points based upon d^* reveal a striking feature showing that essentially all the typical eddies responsible for the formation of the pockets and the sublayer streak pairs were equally close to the wall, with $d^* \approx 50$. The invariant d^* suggests an average height condition that typical eddies must comply with in order to initiate a disturbance on the wall layer. Figure 3.32 shows the details of the correlation by refining the binning process with various bin widths. Results preserve the apparent constancy of d^*. The data representing the mean value of d^* for the events that only pocket was formed is also marked, which is slightly less than $y^+=50$. Further discussion of this feature will be made in next Chapter.

With these findings, the underlying physics that describes the size correlation of the typical eddies and the sublayer features is more readily identifiable. Since the bottoms of these typical eddies were, on average, equally close to the wall, some of them were able to create bigger sublayer feature(s) simply because the larger physical size they had (see C_z^+'s near the top of the figure). This statement, however, can not be seen as conclusive. Although it describes an important feature necessary to uncover the overall size correlation, we have not factored in the intensity of the typical eddies, which should be a crucial factor of the interaction process. The strength of the typical eddies was not obtainable in this study. In the next section, we will see that the use of d^* is more advantageous than using d^+ when the measure of a typical-eddy's ability to initiate an interaction with the wall is considered. Further observation of Figure 3.31 indicates that a linearity between w^+ and d^+ exists. It is found that the slope representing d^+/w^+ is about

0.33 over a range between $50<w^+<140$. In general, Figure 3.31 shows the existence of an overall length-scale correlation between typical eddies, pockets, and sublayer streak pairs.

3.2.6.2 *On the Ability of Initiating an Interaction*

Three subsets of our data base were studied to see how the distance of a typical eddy from the wall could affect the ability of the typical eddy to initiate an interaction with the wall layer. These three subsets consist of samples which are selected based upon the simultaneous occurrence of (i) typical eddy and pocket, (ii) typical eddy and streak pair, and (iii) typical eddy and either streak pair or pocket, respectively. Note that subset (iii) is the union of subsets (i) and (ii). It is important to point out that if a pocket and/or a long streak pair in the sublayer, and a typical eddy in the log region or the lower portion of the outer region were visualized to occur simultaneously in accordance with our sampling criteria, the sublayer feature(s) were assumed to be created as a result of the interaction between the typical eddy and the wall layer. Discussions concerning the legitimacy of the interaction hypothesis will be made in next chapter.

Figure 3.33 presents the probability of the occurrence for each of the above interactions as a function of d^* and d^+. Total sample size is 417. Generally, it shows that the probability for a typical eddy to interact with the wall increases as its distance from the wall decreases. Further examination of the data indicates that, as d^* of a typical eddy decreases, the possibility of forming a pocket and/or a sublayer streak pair increases monotonically. On the other hand, if using d^+ as the measure, the probability of the interaction reduces when d^+ decreases in the region of $d^+<60$. This demonstrates the apparent advantage of using d^* instead of d^+ in this region. The magnitude of d^* is a better direct measure in indicating whether an interaction would take place or not (regardless of the size of the created sublayer features), particularly for the interactions involving the formation of a pocket (i.e. subset i; as defined in previous paragraph). The reader is reminded that, according to the results of the previous section, the spanwise dimensions of the pocket and the sublayer streak pair are found to depend primarily on the magnitude of C_z^+. Summarizing of these findings, when considering the interactions between typical eddies and the existing wall region vorticity distribution, d^* of the typical eddy plays a decisive role in determining whether an initiating interaction with the wall layer will occur, whereas the diameter (C_z^+) of the typical eddy dictates the lateral dimension of the interaction.

An interesting feature in Figure 3.33 worth mentioning is that the probability of the typical eddies having an interaction with the wall layer goes statistically to zero when they were convecting at distances greater than 155 or 218 wall layer units from the wall based upon d^* or d^+ respectively. This is consistent with the data of two-point correlations obtained by Klewicki (1989). He showed that negative spanwise vorticity fluctuation correlations for positive Δy separations and the stationary probe positioned at $y^+=7.5$ were weak when the separations were greater than 100 Δy^+ (correlation negligible when Δy^+ was greater than about 150) at a comparable Reynolds number (see his figure 4.13). Furthermore, Figure 3.33 also shows that the probability of creating a sublayer streak pair was always greater (or, at least, equal) than that of creating a pocket for a typical eddy at a given distance (or normalized distance) from the wall.

The importance of the typical eddy distance from the wall is now further discussed. For convenience, the evolution of the typical eddy/wall layer interactions in turbulent boundary layers is divided into 4 classes based upon the formation of sublayer features. They are as follows.

(1) formation of a pocket only

(2) formation of a streak pair only

(3) formation of both a pocket and a streak pair

(4) neither a pocket or a streak pair was formed (i.e. no interaction)

The samples corresponding to each class of the interactions make up a subset of our data base. It is noted that the intersection between any two subsets described above is a null set. Figure 3.34 shows the probability density distributions of the specified interactions based upon the distance d^+. The representing distribution associated with each class of interactions is the best fit among the normal, log-normal, and the Rayleigh probability density functions. The sample size, principal properties, and the name of each representing distributions are tabulated in Table 3.15. Referring to the table, we can see that about 71% of the typical eddies were able to interact with the wall layer (i.e. union of classes 1, 2, and 3). Among the interaction classes, the event of the least probability of occurrence concerned the interactions in which only pockets were formed (i.e. 5.8% for class 1). Further examination of the table indicates that sublayer streak pairs were formed by typical eddies which were, on average, propagating at greater distances from the wall than that of typical eddies which created pockets. The same feature is also reflected in the peak occurrence as shown in Figure 3.34. This result along with the previous findings from Figure 3.33 are consistent with the observations of Chu and Falco (1988). In their physical simulations, the creation of the wall-region long streak pairs occurred even when the ring vortices were quite distant from the wall, well into the outer part of the log region. All of these suggest that a typical eddy that convected over the wall close enough to create an interaction would initially form a pair of streaks. Pockets would have also been created only if the typical eddies continuously moved towards the wall. It is interesting to note that the probability density function associated with the interactions wherein only streak pairs were formed (i.e. class 2) is best represented by a normal distribution with an amazingly low skewness.

The probability density distribution, which describes the events associated with the class in which only pockets were formed (i.e. class 1), indicates that these typical eddies were, on average, the closest to the wall, and did not result in the formation of streak pairs. This may suggest that these typical eddies were brought, by a strong instantaneous wallward flow field, close to the wall with an incident angle steeper than the normal for typical eddies, so that the interaction became almost like a quick vertical impact on the wall by the outer layer high speed fluid. Consequently, both the interaction time and the region over which the interaction occurred were too short to enable the formation of a pair of streaks of sufficient length that they were able to be differentiated from the pocket interaction. Although, as the table indicates, this class of interactions had the lowest probability of occurrence in turbulent boundary layers, its significance in physics is not allowed to be overlooked because this class might result in the strongest interactions of all classes and hence produce high Reynolds stress near the wall.

Figure 3.35 shows the probability density distribution of each class of interactions based upon the normalized distance d^*. The sample size, principal characteristics, and the name of each representing distribution are tabulated in Table 3.16. It is found that all distributions are best fitted by Rayleigh density functions except the data associated with the events that neither a streak pair nor a pocket was formed (i.e. class 4) when a typical eddy propagated over the wall. Observation of the table shows that the trend of the mean d^*'s for various classes of interactions is similar to that of mean d^+'s, thus the physics drawn from the previous figure/table are also applied when d^* is used as the measure of the distance between typical eddy and the wall. It is also found that the representing probability density functions and their peak occurrences for interaction classes 1, 2, and 3 shown in Figure 3.35 are unable to be clearly distinguished (i.e. the distributions are very similar). This shows that the employment of d^* provides a measure in determining the possibility of interaction between typical eddy and the wall layer without regard to what class of interactions might occur. It is believed that the class of an interaction was mainly decided by not only the incident angle of the typical eddy as mentioned earlier, but also the intensity of the typical eddy and the local vorticity distribution in the sublayer, which were not obtainable through our visual investigation.

Comparison of Tables 3.15 and 3.16 indicates that, for each class of interactions, the difference of $\overline{d^{+}}$- $\overline{d^{*}}$ is approximately 50.5 wall layer units, which is exactly one half of the mean C_z^{+} for all typical eddies. This constant difference suggests a strong geometric similarity in typical eddies among the different classes of interactions. Further examination of the present data suggests that the typical eddies which did not create sublayer streak pairs or pockets (i.e. case 4) were, on average, located way beyond the distances, or normalized distances, of typical eddies that interacted with the wall layer. Additionally, both of the probability density functions based upon d^{+} and d^{*} associated with this no-interaction class are represented by the normal distributions. The underlying physics for the distance and the normalized distance of typical eddies from the wall being the normal distributions is tentatively interpreted as follows. It is known that the distribution of a random variable is sometimes dependent on the magnitude of the random variable. For example, the log-normal distribution is formed when the influences on the random variable are proportional to the magnitude of the variable, whereas the influences on a normally distributed random variable are independent of the variable magnitude (see Aitchison and Brown 1957). Usually, the distribution of a random variable with non-negative value and potentially unconstrained upper limit is non-symmetrical owing to the constraint of the lower limit (i.e. zero, an impossible occurrence of magnitude for the random variable) such as the personal incomes which are log-normally distributed. In the events of no-interaction, the symmetrical feature of the normal distributions for random variables d^+ and d^* apparently shows that the lower limit (zero) of the random variables did not influence the distributions. Physically, it seems to indicate that the presence of the wall (zero) did not affect the distribution of the typical eddies which did not interact with the wall layer. In other words, these typical eddies did not sense the existence of the wall region vorticity distribution or the impermeability condition, so that no interaction could possibly occur.

3.2.7 Temporal Correlations of the Coherent Features

In Sections 3.2.2.5 and 3.2.4.2, we have presented the characteristics of the occurrence periods, t_{TE}^+ and t_P^+, for typical eddies and pockets respectively. It is noted that those results were obtained by performing two independent countings in the cross-stream view (for typical eddies) and the plan view (for pockets). In this section, we will utilize the correlation data to study the temporal relationships associated with the occurrence of the sublayer features and the typical eddies. The procedure adopted for obtaining the period of occurrence of the correlated events was similar to that described in Section 3.2.2.5, except that the additional constraint that the occurrence of the sublayer features was also enforced. In order to collect a large enough size of samples, four measurement positions have been employed. They were located about 200 wall layer units apart in the spanwise direction, so that the events detected at each of these measuring stations provided independent data for the ensemble average. Figure 3.36 shows the probability density function of the period of occurrence (Δt^+) for each specified correlation. The probability density representations of t_{TE}^+ and t_P^+ from Figures 3.15 and 3.21 are also plotted for comparison. The set number, sample size, principal properties, and the name of each distribution are tabulated in Table 3.17. Note that the probability density function which represents each data set is chosen from the best fit among the normal, log-normal, and the Rayleigh distributions. It is found that all of the data sets are best fitted by log-normal distributions except data set #3. In addition, the common features of these log-normal distributions are high positive skewness and variation coefficients (i.e. the mean value and the standard deviation are the same order of magnitude) as shown in the table. The distribution for data set #3 is represented by a normal density function having a relatively low standard deviation. However, the small sample size and the low flatness for this events indicate that the representing distribution is merely a rough approximation. Note that the intersection of sets #3, 4 and 5 is a null set.

The period of the simultaneous occurrences of a typical eddy and a pocket (no streak pair) is described by the properties listed in set #3 of the table. It is found that, on average, about every nine appearances of typical eddies (within the first 300 y^+) resulted in an interaction in which only a pocket was formed in the sublayer (i.e. average $\Delta t^+/t_{TE}^+ \approx 9.3$). However, examination of its probability density representation in Figure 3.36 suggests that interactions of this class took place in a random manner, showing no clear trend that enables us to predict when it will occur. Referring to the table, the occurrence of the events that only a streak pair was formed when a typical eddy convected over the wall is characterized in set #4, showing that statistically the interactions of this class occurred by a rate nearly twice higher than that of set #3 interactions. Further observation of the table indicates that the interactions which resulted in both a pocket and a streak pair formations (set #5) took place about every 80 viscous time units. A very important feature of this distribution is the mode characteristic, which shows that the most probable period of these correlated interaction events is almost identical to that of the individual occurrence of t_{TE}^+'s or t_P^+'s. This suggests that the majority of the pocket formations were coincident with the typical eddy appearances in the near wall region. It also infers that the typical eddies, which created pockets, usually formed streak pairs as well. This again supports the strong correlation of the presence of typical eddies and the formation of sublayer features.

3.2.8 The Effects of Typical Eddy Orientation on the Formation of the Sublayer Features

In Section 3.2.2.4, we have classified the typical eddies into six *modes* according to their inclination angle with respect to the wall in the x-y plane. In this section, we will present the data to show how the interaction could be affected when the orientation of the typical eddy is taken into consideration. Table 3.8 tabulates the statistical features for each *mode* of the typical eddies. The table has been divided into two divisions based upon the sign of the vorticity in the lower portion of the typical eddy. The first three rows present the data of *Mode* 1, 4, and 5 typical eddies which possessed vorticity of the opposite sign as that of the mean shear in their lower lobes. On the other hand, statistics for typical eddies of *Mode* 2, 3, and 6, which were oriented so that the vorticity in their lower portions had the same sign as that of the mean shear are listed in the last three rows.

Examination of the table indicates that the majority of the pockets (84.1%) were created by typical eddies of the first division. Contrarily, only 9 out of 195 pockets (4.6%) were observed to form as the typical eddies of the second division passed over the wall. This reveals a strong dependence between pocket formation and the typical eddy orientation. Note that, in our visual study, 11.3% of the pockets were observed to form in the condition that no typical eddy was convecting over their tops. Results also show that the probability of interacting with the wall layer (i.e. creating either pocket or sublayer streak pair) for typical eddies of the first division was always greater than that for typical eddies of the second division. However, it is interesting to point out that the probability of creating pockets for typical eddies of the first division was greater than that of the second division typical eddies with a ratio of nearly 3 to 1 (i.e. 45.7 : 15.5), but the ratio dropped substantially to approximately 7 to 4 (i.e. 69.6 : 39.7) for the probability of typical eddies to create sublayer streak pairs as shown in the last column of the table. This seems to indicate that the dependence of the streak pair formation upon the typical eddy orientation was considerably weaker than that of the pocket formation. Finally, we must bear in mind that the distance, or normalized distance, of the typical eddy from the wall has also been shown to be able to affect the probability of interaction. It is found that both the distance (d^+) and normalized distance (d^*) from the wall for typical eddies of the first division were, on average, less than those for typical eddies of the second division. This suggests that the strong ability of the first division typical eddies to form pockets are due to at least two characteristics of the typical eddies, the (normalized) distance from the wall and the orientation. Further discussions concerning the mechanisms responsible for the creation of the sublayer features will be made in next chapter.

3.3 Templates of Flow Visualization

3.3.1 The Wall Region Subset of the Interactions

In experiments designed to investigate only the wall region, observations indicated that the sequential evolutions described by the wall region subset of the Overall Production Module (OPM; see Falco et al. 1989a, and Falco 1991) frequently occurred. Figure 3.37 shows an example of the observations in the plan view. The flow is from left to right and the first dye slit is located near the leftmost edge of the pictures. The production sequence starts with the formation of a pair of low-speed streaks via the rearrangement of the red dye emanating from the first wall slit. There are, of course, some other dye rearrangements taking place in the pictures due to either parts of similar events and/or interactions with the current event. The streak pair in Figure 3.37 has an average spacing along its length of $z^{+}\cong 73$, which is nearly equal to the mean spacing of our conditionally sampled streak pairs. It is also found that the pair of long streaks has developed over the distance between the two wall slits (i.e. $x^{+}\cong 440$) in only the first three frames. The time needed to accomplish this is in the order of 20 viscous time units. By the fourth frame, it can be seen that the streak pair is readily marked by the dye emitting out of the second wall slit and a pocket is forming near the downstream end of the streak pair. The continuation of the streak-pair formation shown in the pictures by the two colors of dye infers that the mechanism responsible for this evolution is still active. By the fifth frame, the pocket is clearly seen. The pocket develops through frames four to eight (or nine) and becomes a fully formed pocket (stage III or IV) in about $20t^{+}$ time span. Additionally, the lifetime of the pocket (from frame four to the last frame) is found to be approximately $30t^{+}$. These time scales are consistent with the temporal characteristics of pocket evolution depicted in the paper of Falco (1980). The maximum spanwise dimension of the fully developed pocket in frame nine is about $80z^{+}$. Furthermore, the duration for the entire evolution of the wall-region subset of the interaction can be estimated from this example to be in the order of $60t^{+}$. Note that this time scale can only be treated as a rough estimate, because how well it represents the overall duration of the interactions is not yet known. It is interesting to point out that the flow visualization in the near-wall region using oil droplets and a laser sheet parallel to the wall at $y^{+}=8$ by Bessem et al. (1989) has clearly shown the spatial phasing between the sublayer streak pair and pocket in a stage comparable to the sixth or seventh frame in Figure 3.37. The picture (figure 3 of their paper) was presented in order to demonstrate the quality of a visualization technique, which accidentally provided a very illustrating scenario for the typical spatial phasing of the sublayer features.

Figure 3.38 shows another example in describing the sequence in which the flow development in the vicinity of the pocket is focused. The flow is also from left to right. This sequence begins with the formation of a streak pair which has been developing in the region between the first and the second wall slits. Note that the prints have been enlarged to depict the details of interest so that the first wall slit is not shown in the field of view. The first frame starts the sequence at the time when a pocket has just formed near the downstream end of the streak pair. It is also found that secondary hairpin vortices associated with the pair of streaks appear in the region immediately upstream of the pocket. The stage of the evolution presented in this frame is almost equivalent to that of the fifth or sixth frame in the previous example. In the subsequent frames, we can observe the development of the secondary hairpin vortices. By the second frame, the dye indicates that the pair of hairpin vortices has moved over the edges of the pocket because the lifted hairpins has undergone greater convection velocities than the pocket. In the third, fourth, and fifth frames, the pair of hairpins appears to be rotated towards the center of the pocket. The last two frames show that the twisted hairpins are being induced towards the wall into the pocket center. It is important to point out that the entire sequence of the secondary hairpin rotation takes about only $t^{+}=10$ (frames third to seventh). Although the intensity of the pocket vortex is unable to be measured using dye technique, the rapid evolution clearly suggests that a very strong vorticity exists along the upstream boundary of the pocket. Note that the average streak-pair spacing and the pocket size in the third frame are approximately 94 and 118 wall layer units respectively. Furthermore, the average thickness of the hairpin-vortex filament is found to be of the order of Kolmogorov scale (about 5 to 10 wall layer units).

3.3.2 The Typical Eddy / Sublayer Interaction

Before examples are shown, it is necessary to note that the visual data to be presented below are prints selected from split screen images which initially had three simultaneous views (i.e. using *Method 1*, see Section 2.4), thus the magnified portions shown have higher grain than similar views would show in a single view experiment. Figure 3.39 shows an example illustrating the simultaneous plan and cross-stream observation of a typical eddy/wall layer interaction. The flow is from right to left for the plan view and into the paper for the cross-stream view. The scale in these two views are different due to the additional optical magnification for the cross-stream view (see Figure 2.3). The scale ratio between the plan view and cross-stream view is about 1.5 : 1. Note that side views are not shown since the interaction was not occurring nearby the streamwise laser sheet. In frame A, the plan view shows the development of a pair of streaks (indicated by the black arrows). During this exposure, no organized motion above the wall can be identified at the corresponding location of the cross-stream view. In frames B and C, the formation of a pocket, in the designated area, near the downstream end of the streak pair can be seen in the plan view (also indicated by the black arrows), whereas there is still no organized motion identifiable in the simultaneous cross-stream observation. In the next four frames (i.e. frames D to G), we can see that an intermediate scale vortical motion appears in the cross-stream view (indicated by the white arrow), whose spanwise location is approximately aligned with that of the sublayer streak pair and the pocket. In frames E and F, this vortical motion appears as a streamwise counter-rotating vortex pair. Its spanwise diameter is measured to be about 120 viscous units (i.e. C_z^+). In the last frame, the cross-stream view of the vortical motion is no longer seen. Therefore, the streamwise extent of this vortical motion can be estimated. It is found to be about 102 viscous units (i.e. C_x^+). This indicates that the vortex pair is neither a long axial counter-rotating vortex pair nor the stretched legs of a hairpin. Additionally, the consecutive cross-stream view of the vortical motion is similar to the sequential cross-stream geometry of a typical eddy as sketched in Figure 3.14. All of these suggest that the observed vortical motion is a ring-like typical eddy crossing the transverse laser plane. The temporal and spatial phasing of the typical eddy and the sublayer features indicate that they are correlated events as described in the conditional sampling criteria in Section 2.5. In this example, the pocket size (w^+), streak-pair spacing(l^+), and the height of the typical eddy (d^+) are measured to be approximately 80, 68, and 115 respectively.

Figure 3.40 shows another example illustrating the formation of a pocket by a typical eddy, and the subsequent interaction between the typical eddy and lifted sublayer fluid near the downstream end of the pocket. The pictures show the simultaneous side and plan views of the interaction sequence. The corresponding transverse views are not presented because the interaction took place in the neighborhood of the intersection of the laser sheets, where the excess brightness makes the visualization of the typical eddy in the transverse view impossible. The flow is from left to right and the first dye slit is located at the leftmost edge of the pictures. The sequence starts with the presence of a typical eddy in the vicinity of the wall (indicated by the white arrow), and no apparent sublayer feature appears under it (frame one). The typical eddy in this frame might have just moved into the streamwise laser sheet from the far side as suggested by both the location of the pocket in the second frame and the poor conformation of the typical eddy in the first frame. In frame two, the formation of a pocket flow module near the center of the designated area is clearly observable in the plan view (indicated by the black arrow), although the image is partially blocked by the brightness of the laser sheet. In the meantime, the typical eddy is located at the intersection of the laser sheets, which prevent it from being seen in the side view. Whether or not there is a sublayer streak pair formed upstream of the pocket cannot be determined from the plan view because the presence of the streamwise laser sheet disrupts the view of streak pair observation. In the third and the fourth frames, the typical eddy, which moved out of the transverse laser sheet, and the lifted sublayer fluid, as well as a hairpin vortex (dyed in red) in the downstream end of the pocket are clearly seen. In the fifth frame, the interaction between the lifted sublayer fluid and the typical eddy results in the sublayer fluid being ingested into the typical eddy. As a result, both the typical eddy and the lifted sublayer fluid lose their coherent appearances (see the last frame). This interaction is similar to the Type III interactions as classified by Chu and Falco (1988, also see Liang et al. 1983).

3.3.3 The Pinch-Off of Lifted Hairpins and Formation of New Typical Eddies

Figure 3.41 shows sequential pictures of the evolution of a hairpin vortex into a new typical eddy. In these pictures, the development of the hairpin vortex, which initially formed in the region immediately downstream of the pocket in the last example (i.e. Figure 3.40), is discussed. The flow is from left to right. Note that only the side view is shown since the observation of the hairpin evolution is primarily observable in the side view. The first frame of this figure is about $37t^+$ later than the last frame of Figure 3.40. Through frames two to seven, one can easily observe a new typical eddy emerging from the wall layer fluid through a pinch-off of the lifted hairpin vortex (indicated by the white arrow). By frame four, a clearly defined lower lobe can be seen. In the last few frames, the newly formed typical eddy is observed to evolve from *Mode* 1 into *Mode* 5 before it is out of sight. The rapid change of the typical eddy orientation in such a short time scale was due to the strong shear of the mean velocity in the near wall region. This example shows that the primary hairpin which is formed as a result of typical eddy/sublayer interaction may evolve into a new typical eddy. The time needed for this evolution is about $160t^+$ (i.e. the time between the third frame of Figure 3.40 and the fourth frame of Figure 3.41).

Figures 3.42 and 3.43 show two other examples of typical eddy formation process. Only side views are shown. The flow is from right to left and the rightmost edge of the pictures is the location of the cross-stream laser sheet. In both figures, the process starts with a hairpin being formed near the wall as indicated by the white arrow (frame one). In the subsequent frames, we can clearly see the formation of a new typical eddy from the lifted hairpin. By frame six of Figure 3.42 and frame seven of Figure 3.43, the clearly defined lower lobes are readily observable. Coincidentally, the evolution time for the pinch-off phenomena in both examples are nearly identical, which is approximately $133t^+$. The examples shown in this section indicate the type of visual evidence supporting the hypothesis that typical eddies are produced in the near wall region via pinch-off of wall layer fluid, which also provides a link between the typical eddies observed by Falco and the hairpin vortices observed by others.

CHAPTER 4

DISCUSSION

4.1 Scaling of Sublayer Streak Spacing

In Section 3.2.3, we have pointed out that the conditional sampling of the pairs of long sublayer streaks results in a mean spanwise spacing that apparently differs from the overall streak spacing of the unconditionally sampled long sublayer streaks. Here, we are able to use our statistical results to present an argument addressing that difference; it will be shown that the mean streak-pair spacing essentially provides complementary information for understanding the underlying process of the wall-region long streaky structure spacing in turbulent boundary layers.

Suppose a pair of long low-speed streaks was formed as a result of a typical eddy/wall layer interaction (the formation of pocket is not the main issue here). Our statistical results suggest that the sublayer streak-pair spacing and the spanwise dimension of the typical eddy would be, on average, 75 and 100 wall layer units respectively. Results also show that the average center-to-center spanwise spacing between two neighboring typical eddies was about $z^+=244$. The available knowledge for the length characteristics is summarized by the scenario shown in Figure 4.1, which illustrates the phase relationship of two typical eddies crossing through the cross-stream plane simultaneously. The characteristic parameters of the flow structures are assumed to be random variables with fluctuations about their mean values. Note that only two typical eddies are sketched although others might generally be found in this view. Since almost all the typical eddies sampled were close to the wall, it is rational to assume that they were capable of initiating interactions with the wall layer in the vicinity of the cross-stream laser plane. In Figure 4.1, two pairs of long streaks created due to the interactions are also illustrated in both the plan and cross-stream views. It has been well-known that once a low-speed streak was formed it often extended to a very long streamwise length. This fact strengthens the validity of the phase relationship between the typical eddies and sublayer streak pairs shown in the figure. In the plan view, it appears that three spanwise spacings were established between these four streaks. Therefore, the estimate of the average streak spacing in wall layer units could be computed by a simple calculation, 318+3=106. This method is same to the classical streak-spacing measuring scheme as described in Chapter three, which has been widely employed by many investigators (see for example, Kline et al. 1967, Oldaker and Tiederman 1977) resulting in a hundred wall layer units for the mean streak spacing.

The result of our scaling analysis suggests that the low-speed streaks, which are found to occur randomly in space and time in the near-wall region by many experimentalists, with mean spacing in the order of 100 wall layer units, could result from distributions of streak pairs with an average spanwise spacing of about 75 wall layer units. The coincidence of length scale strongly supports the postulate that, in turbulent boundary layers, the sublayer streaks are formed in pairs rather than being generated singly. As we mentioned earlier, the measurements of Smith and Metzler (1983) clearly indicated that the most probable streak spacing was in the range of 75-80 viscous units (our unconditionally sampled data also verifying the mode is 78). This length characteristic is nearly identical to our mean spacing of streak pairs. The implication of this coincidence is that the majority of the low-speed streaks sampled by Smith and Metzler were essentially paired. More importantly, our results show that these streak pairs were formed as the result of interactions between typical eddies and the wall layer. The link between the inner and outer dynamical features, as well as the agreement on the length characteristics in the wall region, provide statistical support for the typical eddy/wall layer turbulence production model.

It might be questioned if typical eddies are indeed responsible for the formation of the long streak pairs in the sublayer as our correlation data suggest. Specifically, why is the size of a typical eddy Reynolds number dependent whereas the overall spacing of streaks is not? This brings up the core of the question --- 'Is our assertion concerning the mechanism for the formation of long streaks still valid when Reynolds number is taken into account?'. A qualitative answer to this question is made as follows. As we know, at higher Reynolds numbers, the physical size of typical eddies is, on average, greater than that at lower Reynolds numbers when scaled with wall variables as shown in Figure 3.5. On the other hand, the mean streak spacing has been found to be invariant with Reynolds numbers up to 5830 (Smith and Metzler 1983). If the trend of the size correlation between typical eddies and sublayer streak pairs still holds at higher but moderate Reynolds numbers, the spacings of streak pairs which are created by typical eddies at higher Reynolds numbers must be greater than those of streak pairs at lower Reynolds numbers. At $R_\theta \approx 805$, the average ratio of streak-pair spacing to the spacing between neighboring streak pairs is about 1 to 2 (see Figure 4.1). At moderate higher Reynolds numbers, this ratio should increase noticeably towards unity due to both the increase of average streak pair spacing and the decrease of spacing between neighboring streak pairs. This will result in an increasing number of samples with λ^+ about its overall mean value. By the same token, the probability of observing samples with large λ^+ that formed between two narrow streak pairs should also be reduced. Referring to the results of Smith and Metzler (1983, figure 6), two probability density histograms for Reynolds numbers differing by a factor of 4 are compared. It apparently confirms the trend that is described above. In their figure, the log-normal probability representation of λ^+ at higher Reynolds number appears to have smaller standard deviation (i.e. greater concentration of samples about the mean) and skewness (i.e. shorter tail in the large λ^+ region) than those at lower Reynolds number. Although we do not yet know exactly what is the size correlation of typical eddies and the corresponding streak pairs at higher Reynolds numbers, these results suggest that our hypothesis would hold at higher Reynolds number.

4.2 The Formation and Evolution of Typical Eddies

In the previous chapter, we have classified the typical eddies into six characteristic *modes* based upon their orientation with respect to the wall in the x-y plane. It was found that the typical eddies existing between $y^+=300$ and the wall were predominantly oriented as *Mode*-1 typical eddies. It is also understood that the probability of the occurrence of *Mode*-4 and/or *Mode*-6 typical eddies was nearly zero. These statistical findings are strongly in favor of the assertion that the formations of typical eddies are originated from lifted hairpin-shaped vortices through the pinch-off phenomena (see Falco 1983). This is because the typical eddy that most probably would have evolved into *Mode* 1, owing to the sharp mean velocity gradient, was *Mode* 4 which has been, however, proven almost nonexistent. Therefore, *Mode* 1 should represent the initial orientation of a typical eddy as it was being produced. Coincidentally, ring-like vortices pinching-off from tip portions of elongated hairpin vortices are also naturally oriented as *Mode* 1. Our results (see Section 3.2.2.4) also show that the average inclination angle of *Mode*-1 typical eddies is very close to the characteristic angle of hairpin vortices observed by Head and Bandyopadhyay (1981). In addition, Table 3.8 shows that *Mode*-1 typical eddies were the ones that were statistically located closest to wall among the different *modes* (except *Mode* 5 which, however, did not occur often), implying that their close spatial relationship with the wall layer was analogous to the nature of the hairpin vortices. More importantly, typical eddies scale on wall parameters ν and u_τ, and over a few decades their sizes are still close in magnitude to the Taylor micro-scale. These facts lead to our hypothesis that the coherent typical eddies in turbulent boundary flows are formed via the wall-region vorticity reconstruction, most probably through the pinch-off mechanism. In the present study, hairpin-like vortices have been observed in many occasions. They could be visually distinguished from the typical eddies since they were dyed with red color instead of green. Some of them having spanwise dimension in the order of 100 wall layer units were seen to be lifted as high as 150 wall layer units above the wall. In our side-view observations, many hairpins have been clearly visualized to pinch-off into new typical eddies. The typical examples of this phenomenon are shown in pictures embodied in Section 3.3.3. The experiments conducted by Chu and Falco (1988) have also shown that it did occur in the interactions between the ring vortex and a moving belt at certain initial conditions. Moreover, the typical eddy pinch-off phenomenon has been demonstrated to take place in the computations of Moin et al. (1986) as we mentioned in Chapter one.

Examination of our statistical and visual results along with the above supporting information has resulted in the conceptual model shown in the side view of Figure 4.2. It represents the deduced picture of a typical eddy evolution in the log region and lower portion of the outer region. The figure illustrates that a typical eddy of *Mode* 1 is being created out of a lifted hairpin vortex loop via the pinch-off mechanism. It also shows that the typical eddy will immediately be brought either inwards or outwards by the local instantaneous flow field. At the same time, the typical eddy will, of course, be convected downstream and possibly evolve into a *Mode*-2 typical eddy. Referring to Table 3.8, it indicates that we were rarely able to see a typical eddy which had evolved into *Mode* 3.

This might be because the time span required for a typical eddy to evolve from *Mode* 1 into *Mode* 3 (through *Modes* 5 and 2) was usually longer than the typical eddy's life time. Needless to say this is the reason why *Mode*-4 and/or *Mode*-6 typical eddies were almost non-existent. In the same figure, two possible trajectories (shown as dashed lines) are sketched illustrating that sublayer feature(s) would be created if the typical eddy is brought down low enough to interact with the existing wall region vorticity distribution. In some cases, the typical eddy would lose its physical identity by approaching too close to the wall. Normally, the typical eddy will start to move away, or maintain a constant distance, from the wall after having reached the lowest point where its own speed and the inviscid flow boundary effects have overcome the instantaneous wall-ward flow field which has brought it down. Although the sketch suggests that the typical eddy starts to diffuse when oriented as *Mode* 3, the typical eddy may, in fact, blur or even lose its characteristic structure due to diffusion in any *mode* of orientation. It is important to emphasize that the evolution of the typical eddy proposed here is mainly for those existing in the log region and lower portion of the outer region where the mean shear dominates the flow dynamics. Once the typical eddies are displaced beyond the outer region by, for example, the local instantaneous flow eruptions, they may not follow the pattern we proposed because the typical eddies are now embedded in a flow field of higher convection velocity but much less shear.

It is interesting to point out that the hypothesis of the typical eddy origination is also supported by our statistical results in Section 3.2.2.2. They showed that the mean scale of typical eddies grew as the distance from the wall increased (i.e. Figures 3.10 and 3.11), which implies that typical eddies were formed in the vicinity of the wall and continued to grow in size mainly due to diffusion process as they were migrating over the boundary layer. It also leads to an argument that typical eddies propagating beyond the inner region usually don't come back to the proximity of the wall because our data clearly indicate that the typical eddies existing near the wall were, on average, smaller than typical eddies in the outer region, and it seems unlikely that typical eddies of greater dimension shrank their physical size as they moved inwards, unless either significant stretch or interaction with other vortical motions that reinforced their strength occurred during the time when they were moving towards the wall. Nevertheless, this argument is by no means to hint that typical eddies propagating in the outer region are unable to interact with the wall layer (remember that they have advantageous physical size). It does suggest that the interactions between typical eddies and the wall layer are usually initiated by newly formed typical eddies which have strong vorticity intensity and positions close to the wall as their advantages.

4.3 The Estimate for the Mean Vertical Velocity of Typical Eddies Using the Size-Distance Correlation and the Diffusion Equation

As we know, the mean streamwise velocity for typical eddies is of the order of the local mean convection velocity since the mean flow dominates the boundary layer dynamics. We have also learned that typical eddies are normally oriented so that they induce themselves away from the wall. Results of Hoyez (1990) also showed that typical eddies moving outwards outnumbered the typical eddies moving inwards (see histogram in her figure 4-12). It might be interesting to know how the typical eddies migrated vertically in the turbulent boundary layer. If we accept the hypothesis of the typical eddy origination in the inner region and also assume that the growth of the spanwise diameter of typical eddies was purely resulted from diffusion process, then the average vertical velocity (v_{TE}) of typical eddies in the proximity of the wall can be determined. In doing so, we must use the linear relationship of C_z^+ and d^+, as well as the governing equation of diffusion process. As a result, the relationship between v_{TE} and d, when normalized by the free stream velocity U_∞ and the boundary layer thickness δ_{99} respectively, is equated as follows (derivation of this equation is written in Appendix B).

$$v_{TE}/U_\infty = [22.16 + 10.17(d/\delta_{99})]^{-1}$$

Figure 4.3 shows the function in the range of $0.14<d/\delta_{99}<0.7$ (because the linearity of C_z^+ and d^+ used for deriving the function existing only for $55<y^+<280$). Examination of the function indicates that the typical eddies on average migrated outwards with velocity slowly decreasing as the distance from the wall increased. This is consistent with the physical picture that, as time went by, the typical eddies were losing their vorticity intensity in the marked vortex core, thus reducing the induced convection velocity that had an outward normal component. Certainly, part of the typical eddy's vertical movement was driven by its own induction. Blackwelder and Kovasznay (1970) used the continuity equation and the measured growth rate of boundary layer thickness finding out that the maximum mean value of the non-dimensional normal velocity, v/U_∞, was less than 0.0025, which occurred at the outer boundary. It appears that their number is negligible when compared to our estimated v_{TE}/U_∞. Apparently, the outward convection of the typical eddies was not provided by the mean normal velocity of the boundary layer. Figure 4.3 also shows the *rms* of the y-component velocity fluctuation for a turbulent boundary layer at a comparable Reynolds number (see Klewicki 1989). It is found that our estimate is approximately 25% greater than the maximum *rms* of the normal velocity fluctuation. However, it is unclear how the inferred mean vertical velocity of the typical eddies can be related to this quantity.

The time needed for a typical eddy to travel over the entire boundary layer can also be estimated. If we use the mean v_{TE} at $d/\delta_{99}=0.5$ and assume that typical eddies were normally produced at d^+ between 100 and 150, the time required for typical eddies to reach the outer intermittent region is found to be in the order of $t^+=400$. The spatial scale over which this evolution takes place can also be approximated by multiplying the average convection velocity of typical eddies at $d/\delta_{99}=0.5$ by the time span, $t^+\approx 400$. This results in the length scale on the order of $7{,}000x^+$. The question is whether the average life time of typical eddies is greater than $400t^+$ or not. If not, it means that typical eddies which appear in the outer intermittent region have lost most of their energy when we observe them. Thus, the answer seems to be yes, they have a lifetime greater than $400t^+$ unless there are some other mechanisms that can create typical eddies in the outer region. If another mechanism of typical eddy generation dominates the outer region flow, these typical eddies created in the outer region can only contribute to the Reynolds stress in the outer part of the boundary layer, but have little effect on the wall region turbulence production. This is because the argument addressed in the end of the previous section also applies here. It is important to also be reminded that all the discussions made in this section is based upon the assumption that the diffusion was the only cause for the growth in size of the typical eddies.

4.4 The Mechanisms Responsible for the Formation of the Sublayer Features

4.4.1 Formation of Pockets

4.4.1.1 *Stagnation Flows and the Orientation of Typical Eddies*

Falco (1980) suggested that the outer sweeping eddy, which was oriented so that the lower portion of the sweep had vorticity of sign opposite to that of the mean shear, was able to create a favorable flow field for the formation of the pocket flow module. Referring to Table 3.8, our statistical results also showed that the probability of creating pockets for typical eddies possessing positive vorticity in the lower lobe was nearly three times greater than that for typical eddies of negative vorticity near the wall (mean shear had negative vorticity). The findings lead to an interpretation of the mechanism responsible for the pocket formation in the viscous layer. In Figure 4.2, the side view illustrates a scenario showing that a pocket would be created in the sublayer if the typical eddy of *Mode* 1 or *Mode* 5 (*Mode* 4 is nearly non-existent) is brought down low enough to establish a stagnation point in the very-near-wall region (as seen by an observer moving with the speed of the pocket center). The stagnation flow is created as a result of the counter rotational flow field induced by the lower portion of the typical eddy and the mean shear of the boundary layer. In the same figure, the sketch of the close-up isometric view indicates that the presence of the stagnation point locally decelerates the upstream spanwise vortices of the mean shear and accelerates the downstream spanwise vortices, thus providing the mechanism for the generation of a pocket flow.

The link between the stagnation flow and the pocket formation suggests that the orientation of a typical eddy is a crucial factor to determine whether or not a pocket would be created when the typical eddy is in the position to interact with the wall. Since a *Mode* 2 typical eddy possesses vorticity of the same sign as that of the mean shear in the lower portion of the ring vortex, the establishment of a stagnation point very near the wall is unlikely even if the typical eddy is in the proximity of the wall. This would substantially reduce the possibility of producing a pocket. The lack of ability to generate a favorable flow field for pocket formation by this *mode* of typical eddies was well reflected in the statistical outcomes of this study. Table 3.8 shows that merely 6 out of 51 (i.e. 11.7%) *Mode*-2 typical eddies were able to form pockets. Furthermore, although typical eddies of *Mode* 3 or 6 have negative vorticity close to the wall, they are capable of creating stagnation flows in the near wall region, due to the counter rotation of their own, when moving towards the wall. However, this would have occurred only if the typical eddies approached very close to the wall. More importantly, the occurrence of these *modes* was found to be rare (probability for *Mode* 3 is 0.014, for *Mode* 6 is 0.002), thus their contribution to the near-wall region dynamics is limited. Note that the ability to form a pocket for *Mode*-3 typical eddies is also well shown in Table 3.8. It indicates that 3 out of 6 (i.e. 50%) typical eddies of this *mode* created pockets.

4.4.1.2 *The Average Height Condition for Typical Eddies to Create Pockets*

The foregoing discussion has addressed the important role of the typical eddy in inducing a stagnation flow that promotes the pocket formation. In addition to the orientation of a typical eddy, the distance from the wall for a typical eddy is also crucial regarding the formation of a stagnation flow very near the wall. Referring to Figure 3.32, the data based upon d^* show a dominant feature; all of the typical eddies responsible for the formation of both the pockets and the sublayer streak pairs were found, on average, to be at height of $d^*\approx 50$ when the interactions were occurring or just occurred. We have suggested that the invariant d^* could be a statistical height condition with which typical eddies must have complied in order to form the sublayer features. Since we have also learned that the sublayer streak pairs were able to be formed by the typical eddies when they were further out from the wall, this length characteristic (i.e. $d^*\approx 50$) might well be the average height condition for the typical eddies to form the pockets. That is, the "bottoms" of typical eddies on average needed to enter the zone between $y^+\approx 50$ and the wall in order to create pockets. This is consistent with the findings that the mean d^* of typical eddies for the events in which only pocket was formed was slightly less than $y^+=50$ (see Figure 3.32).

Data of two-point correlations concerning spanwise vorticity fluctuation obtained by Klewicki (1989) showed that the negative correlations appeared to become significant when the separations of the probes were under about 50 wall layer units (see his figure 4.13). He also presented data concerning the spanwise vorticity skewness and kurtosis (flatness coefficient) distributions at three Reynolds numbers ranged between 1,010 and 4,850 in his figures 3.14 and 3.15 respectively. The results showed that the skewness coefficient (always negative) reached the strong negative peak near $y^+=40$, then started to increase until $y^+\approx300$. On the other hand, the kurtosis increased from approximately 3 to 8 in the range of $3<y^+<40$ and stayed high for $y^+\geq40$. Combining these statistical features shows a good agreement with our physical picture. Interpretation of these features is as follows.

The trend of skewness suggests an evolution of motions with intense negative spanwise vorticity (i.e. same sign as that of the mean) that lifted from the sublayer, which might be associated with either the tip portion of hairpin vortices or pocket vortices studied by Falco. The data also suggest that the lifted wall region motions reached a maximum intensity at $y^+\approx40$ with respect to the mean of the surrounding motions. The kurtosis profiles showing increase within the first 40 wall layer units confirmed this type of processes. That is, if kurtosis is an indicator of intermittent behavior, the increase of kurtosis in the near wall region is consistent with the physical picture that the proposed motion scaled on wall variables decreased its <u>relative</u> scale as it moved away from the wall. In order that these hairpin-type of motions continued to be dominant farther out in the boundary layer, the skewness probably should have continued to increase negatively. However, his results showed that the skewness started to decline in magnitude for $y^+\geq40$, whereas the kurtosis still maintained in high levels. This indicates that the importance of the lifted hairpin vortices began to level off by a more dominant feature containing motions of strong positive spanwise vorticity for $y^+ \geq 40$. The high kurtosis in this region suggested that these vortical motions occurred intermittently. Recapitulating, our results show that the "bottoms" of the typical eddies were on average located near $y^+=50$ when forming pockets. All of these observations indicate that the motions containing strong positive spanwise vorticity might plausibly be associated with the lower lobes (of sign opposite to that of the mean) of the typical eddies that impinged the wall. In summary, the statistical results and our visual findings suggest that the typical eddies on average start to enter the inner-region dynamical picture by themselves at $y^+ \approx 40$, after which they are also able to significantly influence the near wall region vorticity field through strong vortical interactions.

4.4.2 Formation of Long Sublayer Streaks

In physical simulations, Chu and Falco (1988) have discovered that long counter-rotating streamwise vortices were not necessary for long sublayer streaks to be created in contrast to the suggestion of many authors. Furthermore, the numerical simulations using full Navier-Stoke equations of a turbulent shear flow by Kim (1986) have shown that the eddies which have streamwise vortices were not elongated in the flow direction. In addition, many investigators (see, for example, Praturi and Brodkey 1978) have measured the streamwise vorticity in the near-wall region discovering that these vortices have been of short extent or very weak circulation in the cross-stream plane (also see Bakewell and Lumley 1967). All of these suggest that the long, low-speed streak pairs could be formed by a mechanism other than the streamwise vortices (at least that they are not the primary cause). Referring to our data, it is interesting to note that, by comparing the data of columns 8 and 10 in Table 3.8, the probability for a typical eddy to create a long sublayer streak pair appeared to be less sensitive to its orientation than the creation of a pocket. As we know, the pressure field induced by a roundish typical eddy is almost insensitive to how the typical eddy is oriented. Based upon all the information presented above, it may be concluded that the long sublayer streaks could be created more by the influence of the convecting pressure perturbation than the internal vorticity or velocity field of the incident typical eddy. That is, the directly vortical interactions between typical eddies and the existing wall region vorticity distribution are not required to form streak pairs. If we accept the argument, the formation of the long streak pairs in the sublayer is simply the result of the fluid being pushed away from the center line of the paths of typical eddies moving over the wall, which then builds up into the streaks. The streamwise extent of the streaks therefore depends upon both the time and the spatial length that the typical eddy is able to interact with the wall as it convects downstream.

4.5 Use of the Statistical Correlation of Events to Support the Interaction Hypothesis

In our study, if a pocket and/or a long streak pair in the sublayer, and a typical eddy in the log region and lower portion of the outer region were visualized to occur concurrently in accordance with our sampling criteria, the sublayer features were considered to be created as a result of the interaction between the typical eddy and the existing wall region vorticity distribution. It is understood that if our interaction hypothesis was correct, the probability for the concurrent occurrence of the sublayer features and typical eddies should have been high. That is, for example, if the pocket formations were related to typical eddies as hypothesized, observation of a typical eddy propagating over the top of an evolving pocket should be highly expected. This was what our sampling conditions were constructed for. We sampled the pockets forming in the designated area and checked to determine if typical eddies or any other Taylor micro-scale coherent motions were crossing the transverse laser plane which was setup immediately downstream of the designated area. By doing this, the motions responsible for the pocket formations could be revealed. As we briefly mentioned before, other than typical eddies no coherent motion which had size comparable to the size of the pockets and streak pairs was found to occur with statistical significance.

Referring to Table 3.16, our results show that 41.5% of the typical eddies were found to propagate over the wall with pockets formed in the sublayer, and 65.4% of the typical eddies were associated with the formation of long streak pairs in the sublayer. However, these statistical numbers do not fully reflect the legitimacy of our interaction hypothesis. This is because some of the observed typical eddies, which were found unable to interact with the wall layer based upon our observation arrangement, were either located too far away from the wall to make any disturbance in the wall layer, or they might be able to create pockets in regions other than the designated area (in particular, just downstream). As explained above, the best measure for the validation of the hypothesis is reflected on the ratio, N_{TE}/N_P, which stands for the probability of the typical eddy occurrence when a pocket was visualized to form. Table 4.1 (see below) shows the corresponding occurrence of typical eddies based upon the occurrence of pockets and/or long sublayer streak pairs. It is found that 88% of the sublayer events were observed to take place coincidentally with typical eddies convecting over their tops at distances varying from 0 to 300 viscous units from the wall. This ratio provides a strong statistical evidence showing that the typical eddies were indeed closely related to the creation of pockets and long streak pairs in the viscous layer as hypothesized.

Table 4.1 The corresponding occurrence of typical eddy in the log region and lower portion of the outer region based upon the occurrence of pocket and/or long streak pairs in the wall layer.

Coherent Features Observed in the Sublayer	N	%	No. of Typical Eddies Simultaneously Observed above the Sublayer Events (N_{TE})	N_{TE}/N%
Pocket with or without Streak Pair	195	100	173	88.7
Pocket with Streak Pair	167	85.6	149	89.2
Pocket only	28	14.4	24	85.7

Examination of the table also indicates that near 90% of the events, which consisted of both the long streak pair and pocket formations in the sublayer, were found to be associated with the occurrence of typical eddies. The ratio drops to about 85% for the events in which only pockets were formed. Although the difference between these two ratios is not great, it is consistent with the observation that the typical eddies, which created only pockets in the sublayer, had greater probability to lose their vortex-ring-shaped structures during the interactions than the typical eddies that created both long streak pairs and pockets. It is interesting to note that the typical eddies responsible for events in which only pockets were created had, on average, the lowest d^* among all the classes of interactions (see Table 3.16). The physics behind this has been partially discussed in Section 3.2.6.2, suggesting that the typical eddies of this kind were convected towards the wall with an incident angle steeper than that of the typical eddies creating both pockets and streak pairs. Consequently, their chances of eluding the wall were reduced. Furthermore, hot-wire measurements conducted by Klewicki et al. (1990)

have shown that vortices with vorticity of sign opposite to that of the mean shear had essentially zero probability of existing within the first 12 wall layer units. It can be deduced that a typical eddy with vorticity of opposite sign of the mean shear in its lower lobe would never maintain its vortex-ring-like structure if the lower portion of the typical eddy approached to the wall within 12 wall layer units. Referring to Table 3.8, we have learned that typical eddies with vorticity of opposite sign compared with that of the mean shear in its lower lobe (for instance, *Mode* 1) were, however, the main contributors of creating the pockets. This suggests that some of the typical eddies, which created only pockets, would have lost their structural identities because their lower portions had entered into the immediate proximity of the wall in which the vorticity with opposite sign as that of the mean shear could never be sustained (in an attached flow). The vortex-ring-shaped structures broke up because the lower portions of these typical eddies strongly interact with the sublayer vorticity (Type III or IV interaction, Chu and Falco 1988) and undergo a violent instability. Referring to Table 4.1, this could be the reason why a statistically smaller number of typical eddies were visualized when this class of interactions occurred.

4.6 Implications for Drag Reductions

Drag reduction for surfaces exposed to turbulent flows has been a long time interest of engineering research. Control of turbulent boundary layers has been attempted using outer layer manipulators such as LEBU's (see, for example, Lemay et al. 1988), passive wall region modifications such as riblets (see, for example, Walsh 1982), or combinations of both. Active controls such as air suction and fluid ejection have also been experimented. In the current study, we have learned that many characteristics of the typical eddy are able to directly affect its ability of interacting with the wall layer.

Therefore, modifications of any of these typical eddy characteristics will definitely result in an alternation of the drag on the wall. Some of these parameters, such as the eddy size and vorticity intensity, may not be controllable. However modifications of many others are possible, for instances, the angle of incidence, orientation in the x-y plane, and the distance from the wall.

Suppose the turbulence production in the near-wall region is indeed undergoing a cyclic procedure as we proposed, with the new typical eddies produced via the pinch-off process. As we can see, it is very important for revealing the ordered spatial-temporal correlations of these coherent features because the uncovered inter-relationships can provide many places to apply a control mechanism to break the chain and interrupt the cyclic production process. By doing this, we will be able to alter not only the drag in the local region but also drag in the downstream. According to the present study, most of the sublayer feature formations were found to be directly related to the typical eddies propagating over the region close to the wall. With respect to the drag reduction, the typical eddy appears to be the key in the production chain that can be modified by outer layer manipulations. Many passive outer region manipulators have been used to interfere with the LSMs enabling the sweeping flow field, which could bring the typical eddies to the proximity of the wall, to be diminished. The attempts were somewhat successful as indicated by the local drag reduction, but the drag downstream was also increased owing to the disturbances created by the intersection of the wallward side of the wake (formed behind manipulators) and the wall layer (see Falco and Rashidnia 1987).

Active control of typical eddies in the log and the outer regions is also possible. This, however, requires an un-intrusive detector which can rapidly monitor the formation of typical eddies or their current state. A discriminator (with criteria functions) is also needed in order to determine when and how long a control should apply. If we can, for instance, detect the orientation of typical eddies and apply a control, if necessary, to alter it, we can easily inhibit the establishment of a favorable flow field for pocket formation. Although the formation of sublayer streaks can not be prevented by solely altering the orientation of typical eddies, their contribution to the turbulence production can be confined by using riblets which will be discussed below. The most probable distance of the typical eddies from the wall for each class of interactions and the frequencies of the correlated events are available from our probability density distributions. This information may provide statistical references needed for a control algorithm to be developed for interrupting the process of the interactions. Our data also show that the wall-region interactions caused by the typical eddies did not take place when typical eddies are on average positioned greater than 218 and 155 wall layer units for d^+ and d^*, respectively. Additionally, $d^* \approx 50$ is found to be statistically critical for typical eddies to form pockets. The implication is that if we could maintain typical eddies above the critical distance from the wall, the suppression of turbulence would have been substantial and hence the skin friction. Due to the control capability at this stage, the inability of accomplishing the foregoing task is understood, but it does provide a subject worth further studying and possibly be done by a computational work.

Among attempted wall region modifications, riblets are found to be effective on stabilizing the long sublayer streaks and hence inhibiting their subsequent breakup. However, the decrease of the drag is limited (5%-7%, Walsh 1982) by solely controlling the stability of long streaks. This result is foreseeable simply because the production of turbulence in the near-wall region is dominated by a more important process, that is the stretching and amplification of the pocket vortices. Owing to the technical difficulty of achieving active control of typical eddies in the log and the outer regions, the design of wall region modifications to interfere with the pocket formation and its subsequent evolution seems more feasible for practical implementation. According to our investigations, the necessity for a pocket formation is a stagnation point in the very-near-wall region as seen by an observer riding with the mean velocity of the pocket. Finding a mean to prevent the stagnation flows from occurring and/or to interfere with the retarding tendency of the pocket vortices inhibiting further deformation of the sublayer vortices appears to be the main task for the study of drag reduction at this stage.

CHAPTER 5

CONCLUSIONS

The correlations between the major coherent motions existing in the lower portion of turbulent boundary layers have been studied statistically via visual analysis. Experiments were carried out in a water channel which provided an incompressible smooth-surface turbulent flat-plate flow with $R_\theta \approx 805$ at the observing section. Long sublayer streak pairs and pocket flow modules were sampled when observed to form and evolve under passing typical eddies in the log region and lower part of the outer region. In the cross-stream observation, portions of the typical eddies appeared as counter-rotating vortex pairs. Efforts have been made through the development of our multi-color dye system and visualization technique to eliminate the possibility that hairpin legs or long axial vortex pairs were mistakenly recognized as typical eddies. Results show that the streamwise extent of the counter-rotating vortex pairs passing through the crossss-stream laser sheet were on average 77 wall layer units, which conforms well to the length characteristic of typical eddies that our overall evidence showed they were part of. Our data showed that the typical eddies exist throughout nearly the entire boundary layer, which is contradictory to the assertion of Head and Bandyopadhyay (1981).

A statistical relationship between these coherent features has been found. The probability density distributions of the non-dimensional spanwise length scales for typical eddies, pockets, and long streak pairs were all well approximated by log-normal density functions having mean values of about 101, 82, and 75 wall layer units respectively. Additionally, the evaluation of the overall spanwise spacing of the long low-speed streaks using a classical counting method was also performed. The mean streak spacing was found to be about $z^+ \approx 96$, which is consistent with outcomes of many previous experiments. Correlations of the simultaneous occurrence of the typical eddies and the sublayer features -- long streak pairs and pockets -- developing underneath them were formed. They show that the dimensions of both sublayer features increased as the spanwise diameter of the typical eddy increased. It is also found that the correlation of the pockets and the long sublayer streak pairs was better characterized using the information of the third coherent motions, the typical eddies. Furthermore, we are able to use our statistical results of the typical eddy spanwise distribution spacing and the mean streak-pair spacing to present an argument showing that long sublayer streaks, generated in pairs, are spaced so as to result in the overall mean streak spacing ($\lambda^+ \sim 100$). The foregoing results strongly support the hypothesis that the coherent typical eddies are the significant motions that govern the generation of the wall region dynamical features in the turbulent boundary layer.

Based upon both the statistical findings and the inference from piecing together the visual evidence, the origination of the typical eddies and the pinch-off phenomena of wall-region lifted hairpin vortices were linked. Accordingly, a cyclic interaction process was deduced. In addition, the relationship between the vortex diffusion and the growing typical eddy magnitude as a function of its distance from the wall provides not only extra support to the hypothesis of cyclic interaction, but also an argument that the wall region interactions were mainly initiated by newly formed typical eddies existing adjacent to the wall. Results have also shown that the pocket formation is associated with (a) the presence of a typical eddy, and (b) the ability of the typical eddy to form a convected stagnation flow very near the wall (as seen by an observer moving with the velocity of the pocket center). Statistical results show that the latter is primarily governed by two overall typical eddy characteristics : the orientation in the x-y plane, and the distance from the wall. Our data also suggest that the long streak pairs found in the sublayer could have been formed as a response to the convecting pressure disturbance induced by the typical eddies propagating over the wall. It also appears that typical eddies are able to produce pairs of low-speed streaks from a distance greater than from which that they can create pockets.

A normalized length variable, d^* ($=d^+-0.5C_z{}^+$), was introduced as the physical distance between the "bottom" of the typical eddy and the wall. It was found that this length characteristic is a potential measure for the ability of a typical eddy to initiate an interaction with the existing wall region vorticity distribution, particularly for the pocket formation events in which the bottoms of the corresponding typical eddies were, on average, located at $y^+\approx50$ (i.e. $d^*\approx50$). Furthermore, the probability for the simultaneous occurrence of the typical eddy and the sublayer feature(s) was found to be remarkably high. It serves as a measure indicating that the hypothesis of the inner/outer coherent motions is legitimate.

Qualitative flow visualization was done using a double-dye "refresh" wall slit and a cross-stream observation arrangement. Results demonstrated that a sequential evolution existed incorporating all of the important structural features in the viscous sublayer and the typical eddies in the log region and/or lower portion of the outer region. The entire sequence, with period of occurrence in the order of 80 viscous units, made up the Overall Production Module (OPM) depicted by Falco et al. (1989a) and Falco (1991). In the wall region observation, the rapid induction of the secondary hairpins towards the wall reveals the predominant streamwise vorticity of the stretching pocket vortex in this event. Summarizing, both the visual observations and the statistical correlations provide additional support for, and more detail about the inner/outer region interactions embodied in the Overall Production Module. It also offers information necessary for the study of drag reduction in wall-bounded turbulent flows.

TABLES

Flow characteristic	Denotation	Value
Reynolds number	R_θ	805
Temperature	T	12.5 °C
Kinematic viscosity	ν	0.0123 cm^2/sec
Momentum thickness	θ	0.465 cm
Velocity at free surface	U_∞	0.21 m/sec
Boundary layer thickness	δ_{99}	4.7 cm
Shape factor	H	1.271
Density	ρ	1 g/cm^3
Skin friction coefficient	c_f	0.005
Friction velocity	u_τ	1.065 cm/sec

Table 3.1 Summary of principal characteristics of the turbulent boundary layer flow.

Falco's Data at R_θ=740		Present Data at R_θ=805	
$C_x u_\tau/\nu$	75.0	76.9	$C_x u_\tau/\nu$
C_x/θ	1.95	1.91	C_x/θ
$C_y u_\tau/\nu$	50.5	50.7	$C_z u_\tau/2\nu$
C_y/θ	1.33	1.26	$C_z/2\theta$

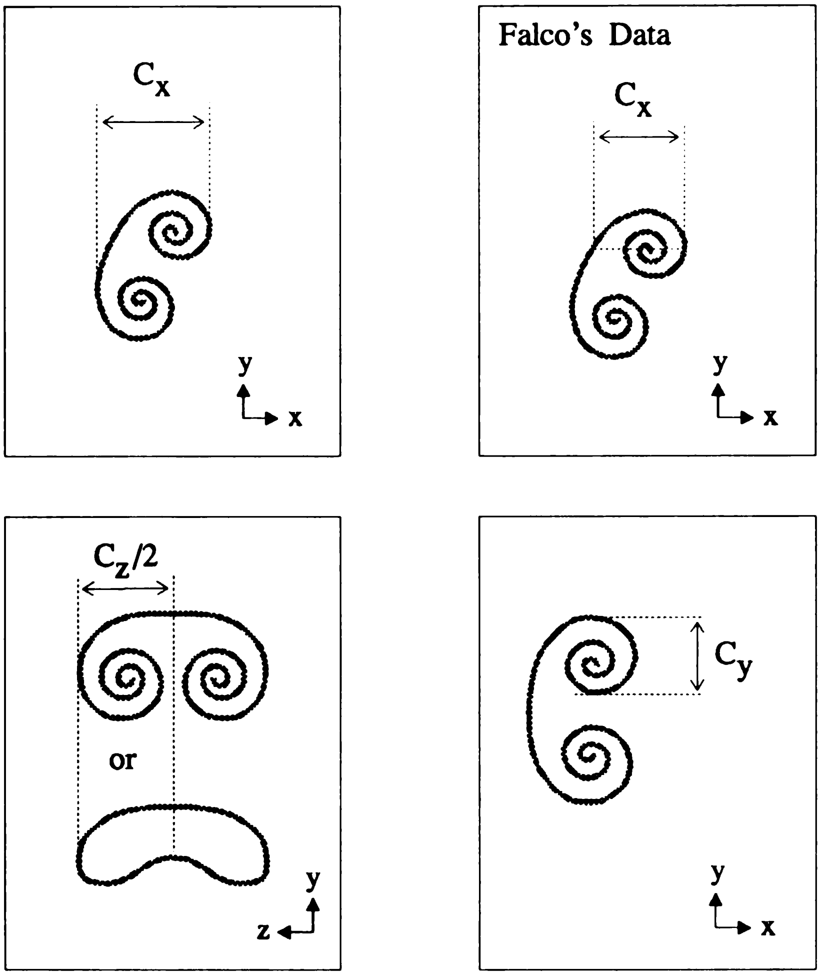

Table 3.6 A comparison of typical-eddy dimensions between outer-layer data and the present data at $R_\theta \approx 805$. The data are non-dimensionalized by both variables θ and u_τ/ν. The definition sketch of each scale is also illustrated. Note the difference of C_x between his measurement and ours.

Typical Eddy *Mode*	N_{TE}	%	$\overline{d+}$	$\overline{d*}$	$\overline{C_z{}^+}$	Np[§]	$N_p/N_T\%$	$N_p/N_{TE}\%$	N_s[§§]	$N_s/N_{TE}\%$
1	343	82.3	113.7	62.9	101.6	154	79.0	45.7	238	69.6
4	2	0.5	123.5	68.5	110.0	1	0.5		2	
5	14	3.4	113.1	61.7	102.9	9	4.6		10	
2	51	12.2	142.8	93.9	97.9	6	3.1	15.5	19	39.7
3	6	1.4	159.0	108.2	101.7	3	1.5		4	
6	1	0.2	119.0	66.1	105.8	0	0		0	

where, N_T=195 (Total number of pockets observed)

Table 3.8 The statistical features of the typical eddies in each characteristic *mode* of orientation.

[§] Number of typical eddies that created pockets.

[§§] Number of typical eddies that created streak pairs.

Event Description	N	%	$\overline{d^+}$	σ^+ of d^+	S	F	ψ	Distribution
All typical eddies	417	100	117.92	42.26	0.707	3.45	0.36	log-normal
Streak formation only	124	29.7	104.07	26.84	0.003	2.97	0.26	normal
Pocket formation only	24	5.8	97.50	27.11	0.889	3.64	0.28	log-normal
Streak and pocket formation	149	35.7	99.60	31.99	0.358	2.21	0.32	normal
No interaction	120	28.8	159.07	40.88	0.201	3.15	0.26	normal

Table 3.15 The principal properties of the probability density distribution for each class of interactions based upon the distance (d^+) of typical eddy from the wall.

Event Description	N	%	$\overline{d^*}$	σ^+ of d^*	S	F	ψ	Distribution
All typical eddies	417	100	67.47	41.36	0.745	3.29	0.61	Rayleigh
Streak formation only	124	29.7	53.51	25.47	0.112	2.86	0.48	Rayleigh
Pocket formation only	24	5.8	46.80	29.41	0.809	3.65	0.63	Rayleigh
Streak and pocket formation	149	35.7	49.20	30.18	0.507	2.44	0.61	Rayleigh
No interaction	120	28.8	108.71	39.85	0.105	2.84	0.37	normal

Table 3.16 The principal properties of the probability density distribution for each class of interactions based upon the normalized distance (d^*) of typical eddy from the wall.

Set #	Correlation Description	N	Mean	Mode	σ	S	F	ψ	Distribution
1	typical eddy	157	26.3	11.3	24.2	2.27	9.34	0.92	log-normal
2	pocket	183	29.8	13.5	24.3	1.91	6.97	0.82	log-normal
3	typical eddy & pocket only	15	245.1	245.1	191.5	0.20	1.55	0.78	normal
4	typical eddy & streak pair only	60	121.1	26.5	114.6	1.44	4.62	0.95	log-normal
5	typical eddy, pocket & streak pair	96	81.8	12.7	83.4	1.98	8.26	1.02	log-normal

Table 3.17 **The principal properties of the probability density distributions for various correlated interaction events based upon the period of occurrences (Δt^+). The mode for each distribution is determined using histogram.**

FIGURES

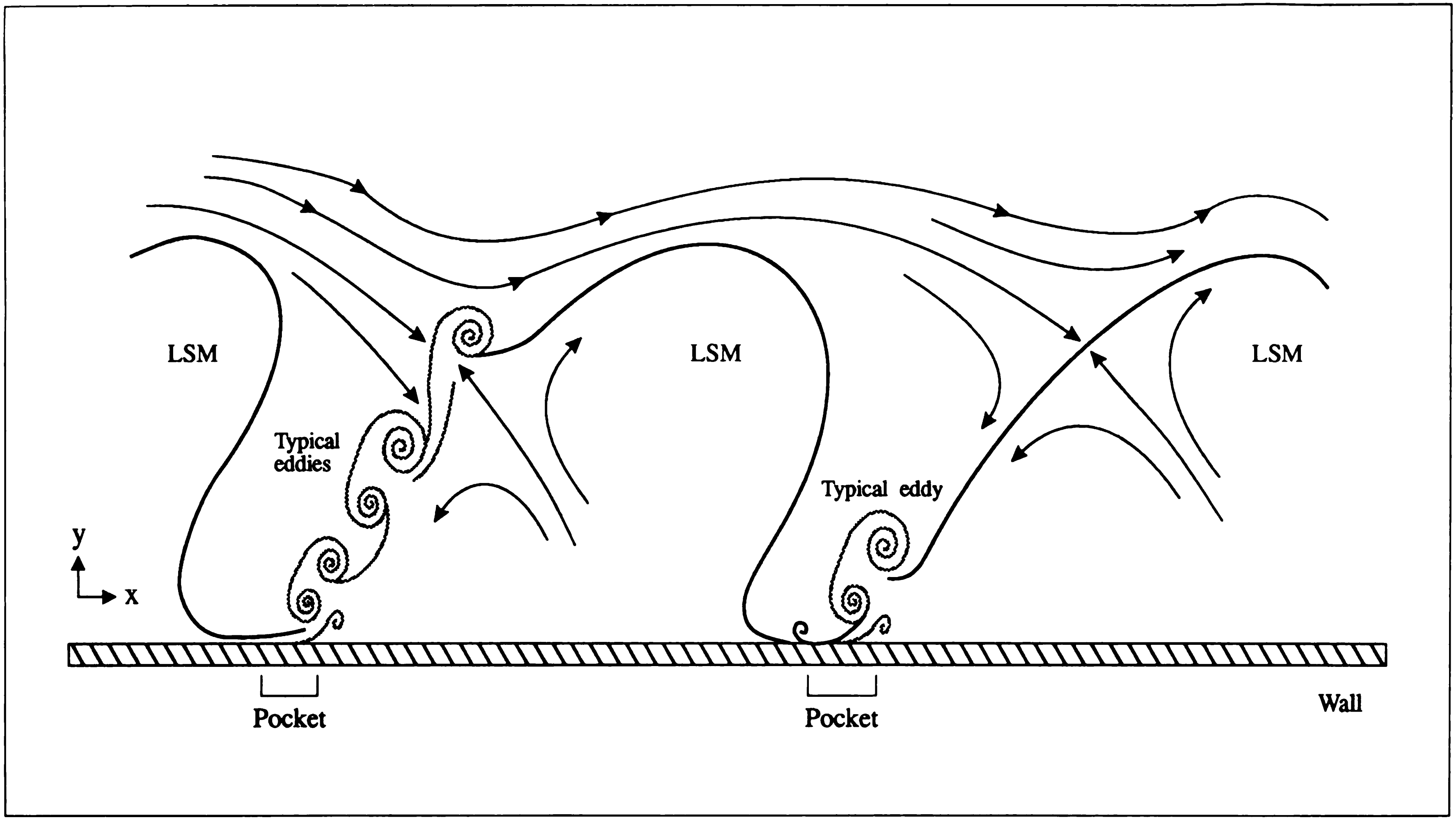

Figure 1.1 A conceptual model of the outer flow organization of the Overall Production Module, showing the spatial phasing of typical eddies and LSMs as seen by an observer moving with the convection velocity of the upstream side of the LSMs. This will result in wall-region interactions as typical eddies are being brought to the proximity of the wall (figure adapted from Falco et al. 1989b).

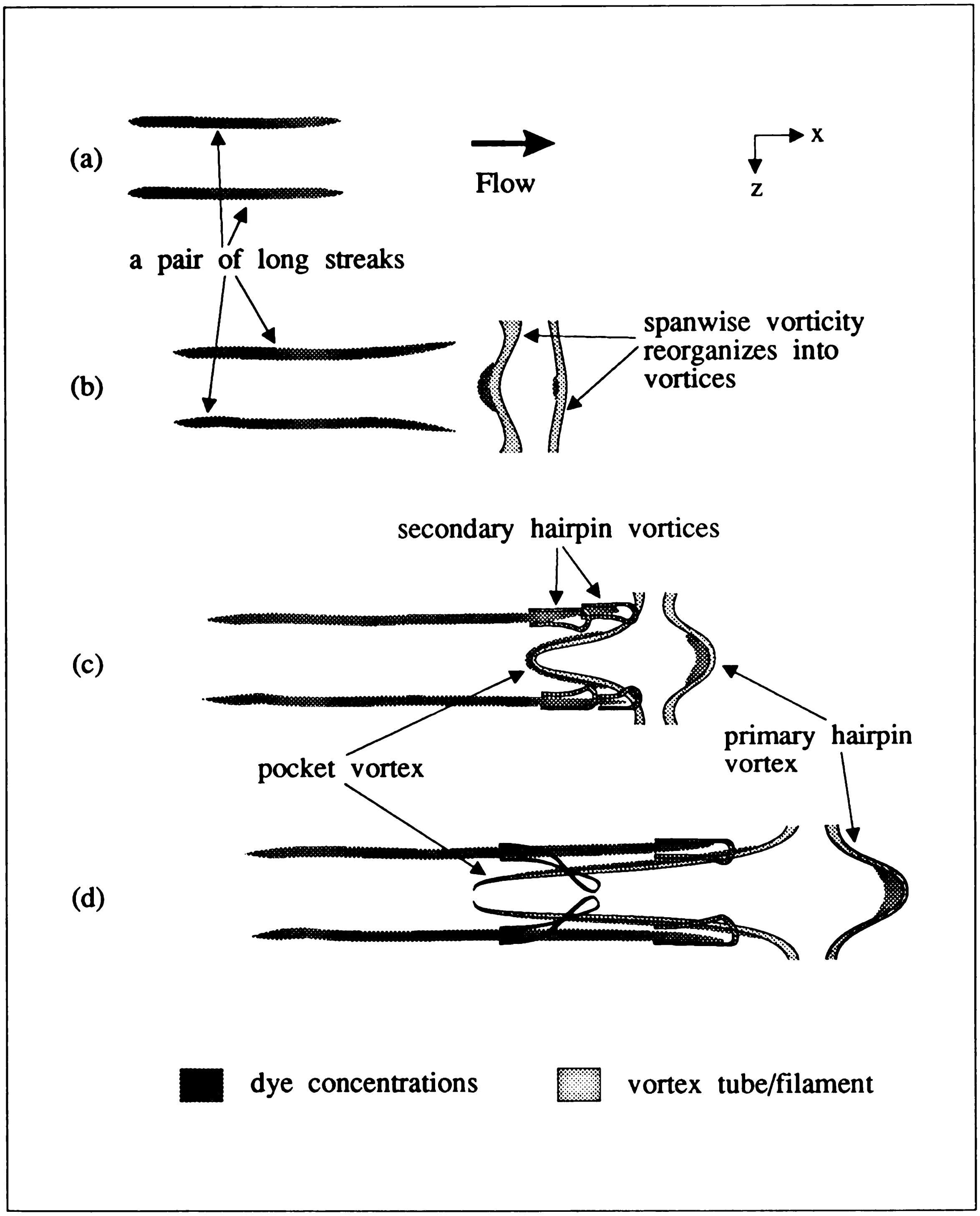

Figure 1.2 A plan view illustrating four sequences in the evolution of the wall region subset of the OPM. It begins with (a) the formation of a pair of streaks, followed by (b) the development of streaks and formation of pocket, followed by (c) the formation of vortices in the pocket and over the streaks, followed by (d) the interaction between the stretching pocket vortex and the secondary hairpin vortices (figure adapted from Falco et al. 1989b).

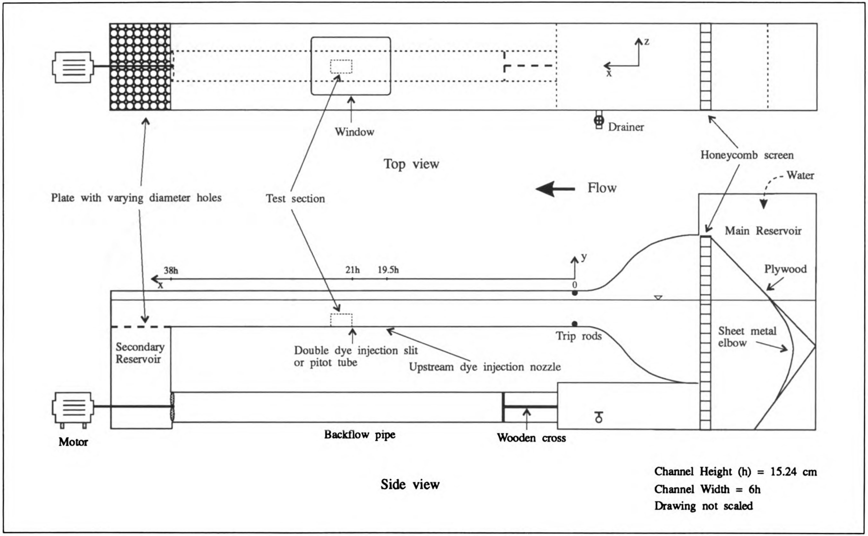

Figure 2.1 Schematic of the low-speed water tunnel.

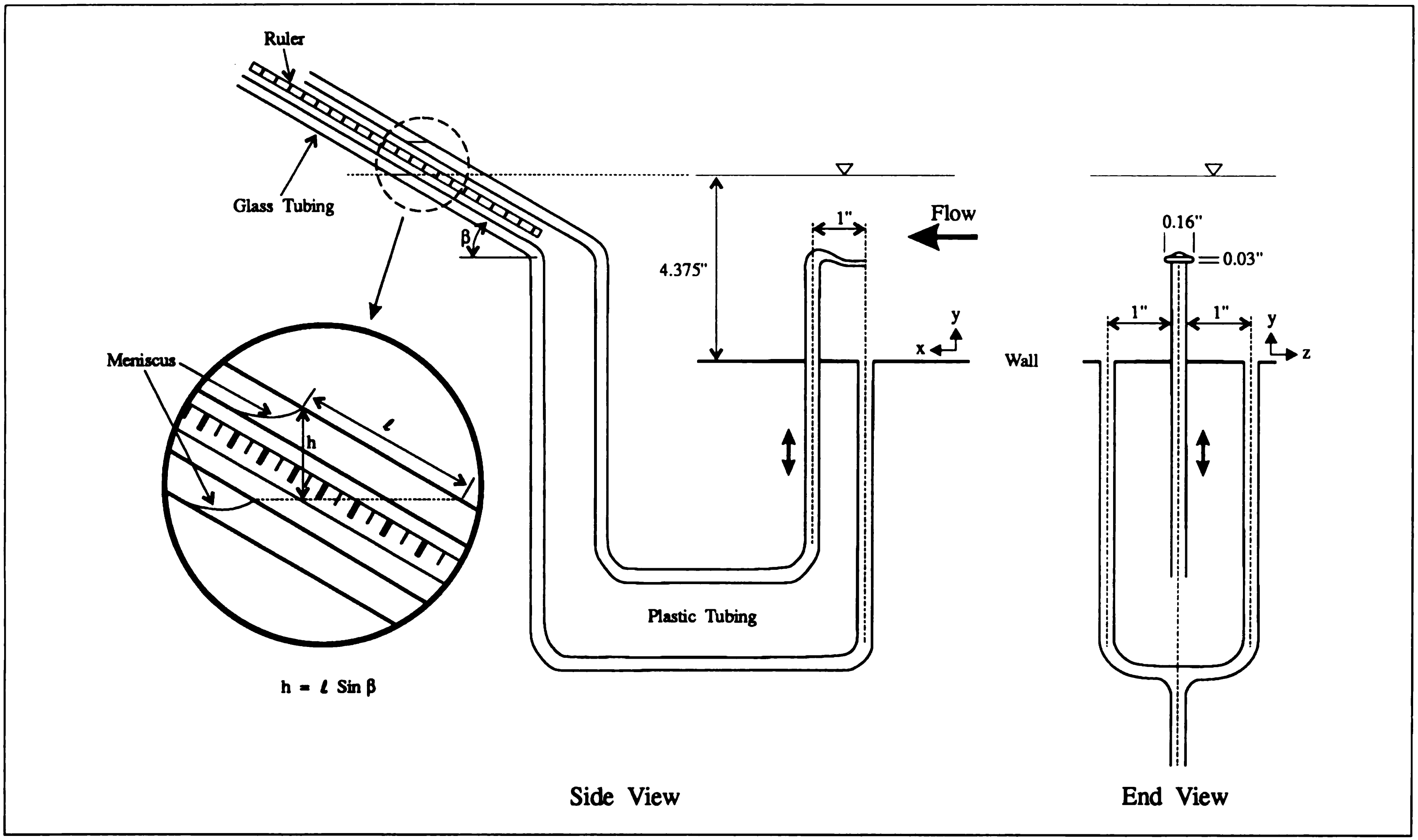

Figure 2.2 Schematic diagram illustrating the setup of pressure anemometry used for the mean velocity measurement. β=30 degrees.

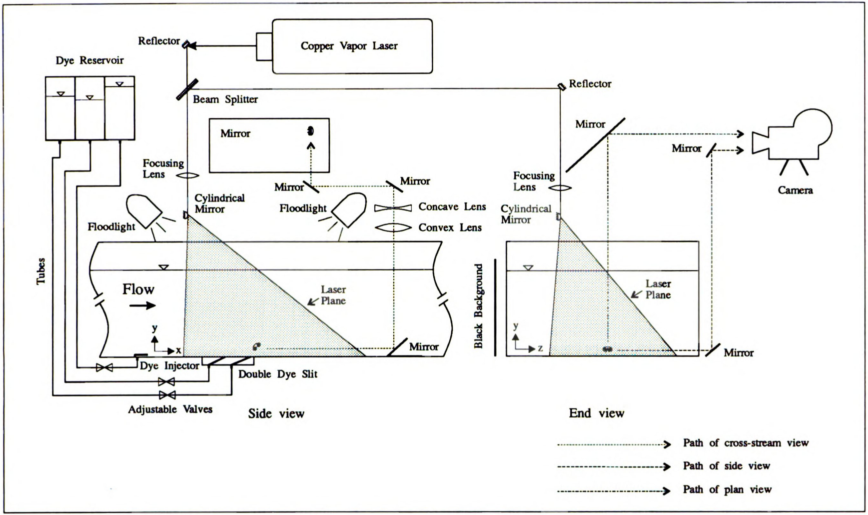

Figure 2.3 Side and end views of a schematic of the experimental apparatus employed in the visualization of turbulent boundary flows.

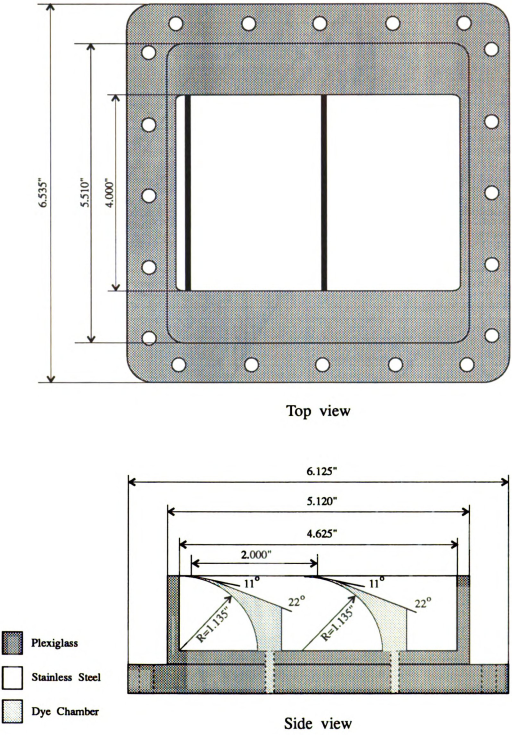

Figure 2.4 Schematic of the double-dye slit.

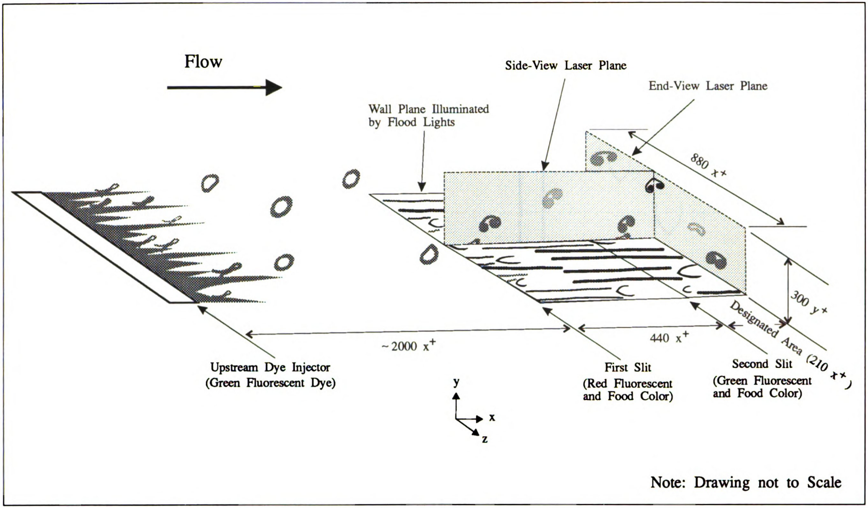

Figure 2.5 An isometric view of our experiment showing the designated area incorporated into the multi-corlor dye system and observation arrangement.

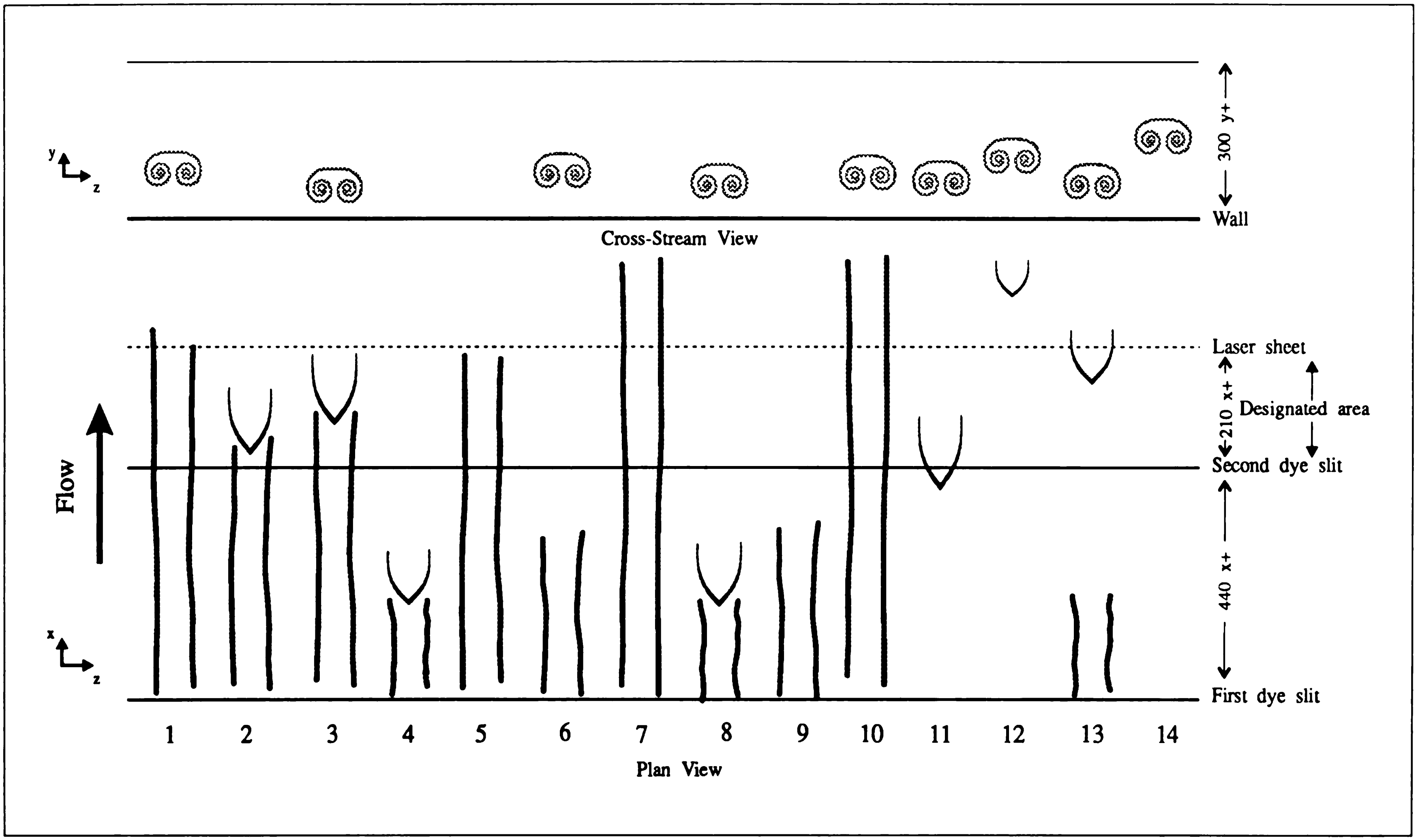

Figure 2.6 Examples describe the principles of the conditional sampling of coherent features. All typical eddies observed are sampled. Sublayer features are sampled for conditions 1, 2, 3, and 11. Only a pocket is sampled in condition 13.

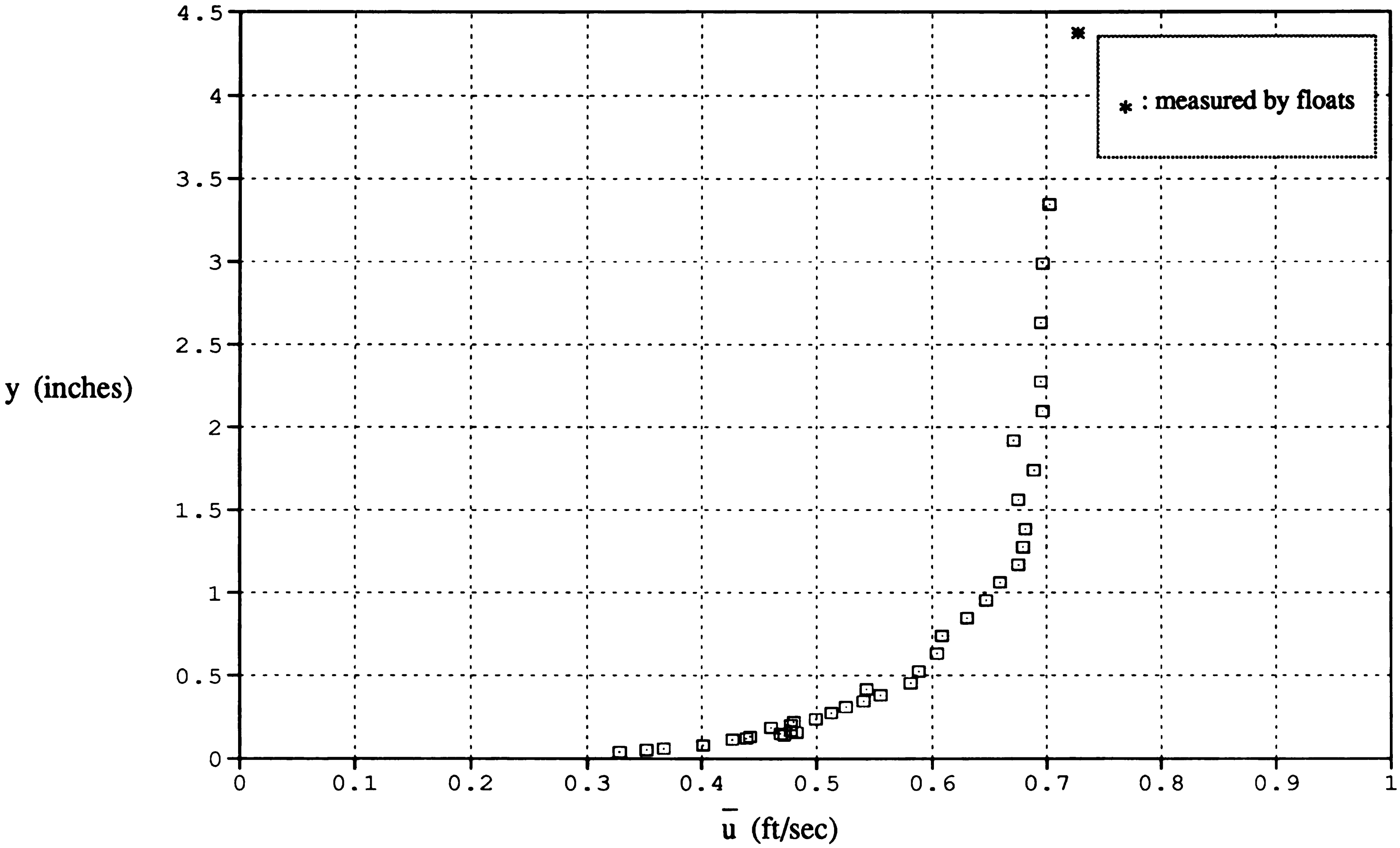

Figure 3.1 Dimensional mean velocity profile obtained from pressure measurements. The velocity of the free surface was measured by floats.

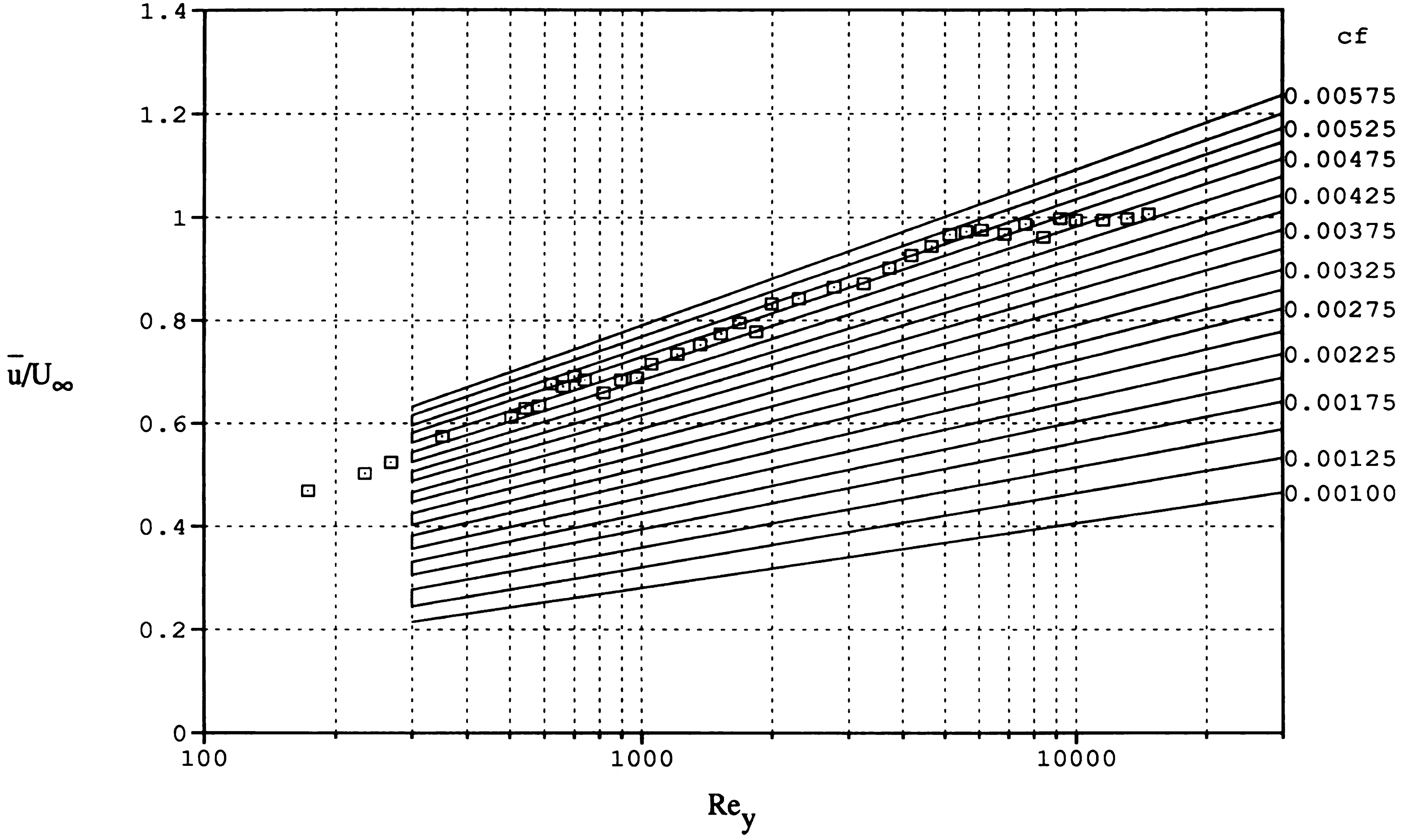

Figure 3.2 The determination of skin friction coefficient utilizing Clauser plot.

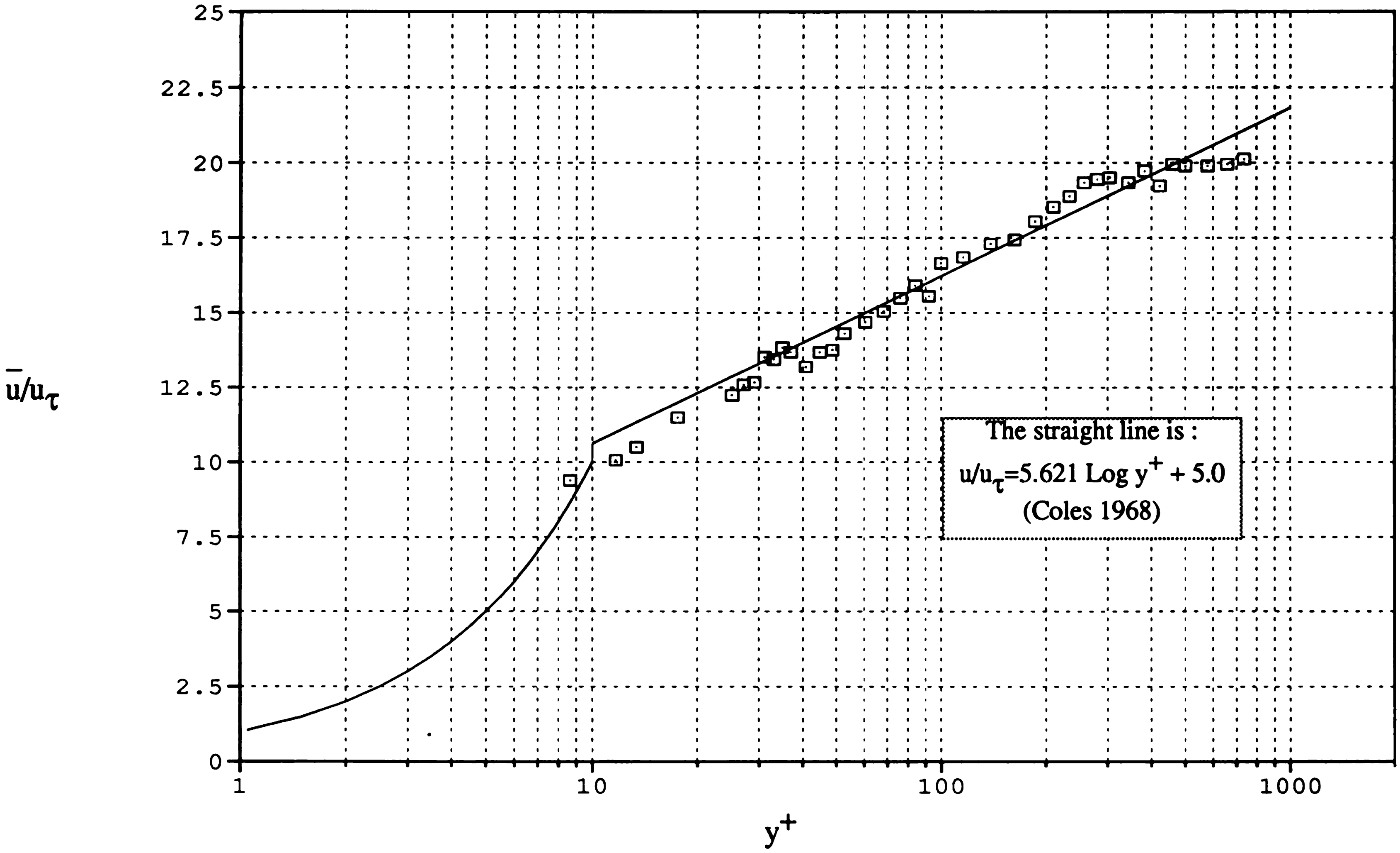

Figure 3.3 Logarithmic mean velocity profile.

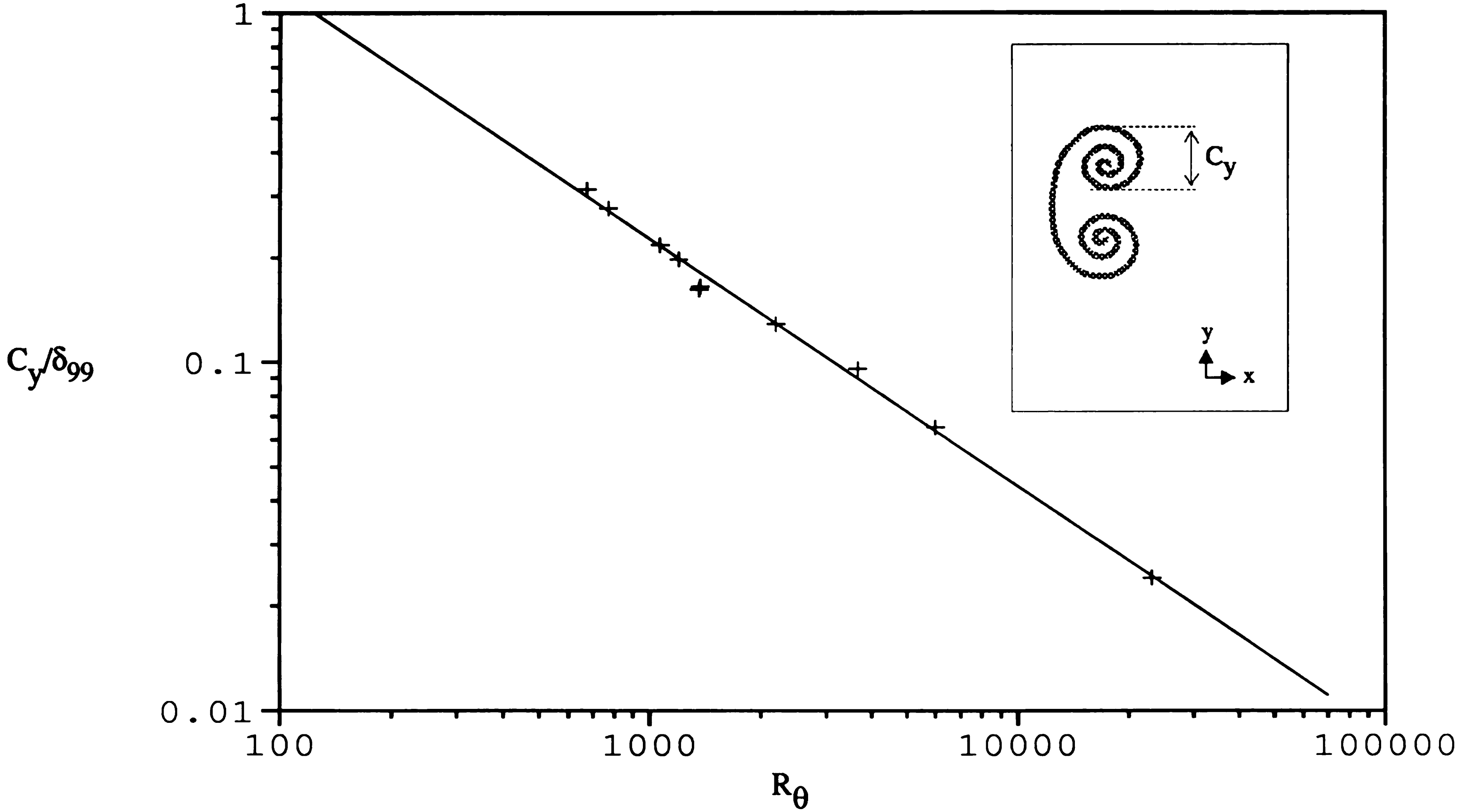

Figure 3.4 The average length scale of the visualized cores of typical eddies, in the intermittent region of turbulent boundary layers, as a function of R_θ when non-dimensionalized by the boundary layer thickness δ_{99}. The curve fit is $C_y/\delta_{99}=30.5R_\theta^{-0.758}$ (Falco 1991). The definition sketch of C_y is also illustrated.

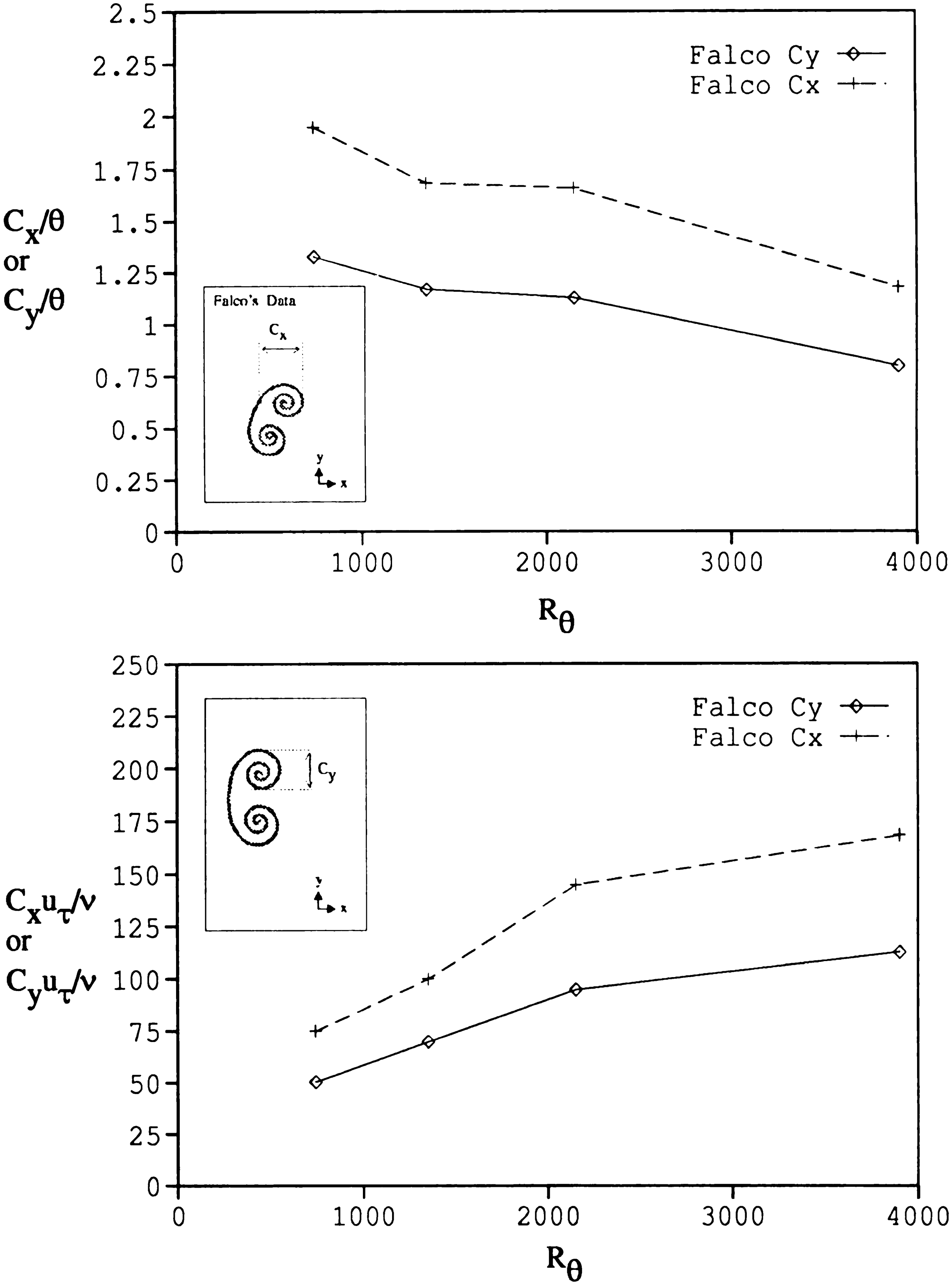

Figure 3.5 The average dimensions of typical eddies in the outer intermittent region as a function of Reynolds number. The data were non-dimensionalized by both variables, θ and u_τ/ν, in the respective figures. The definition sketches of C_x and C_y are also illustrated.

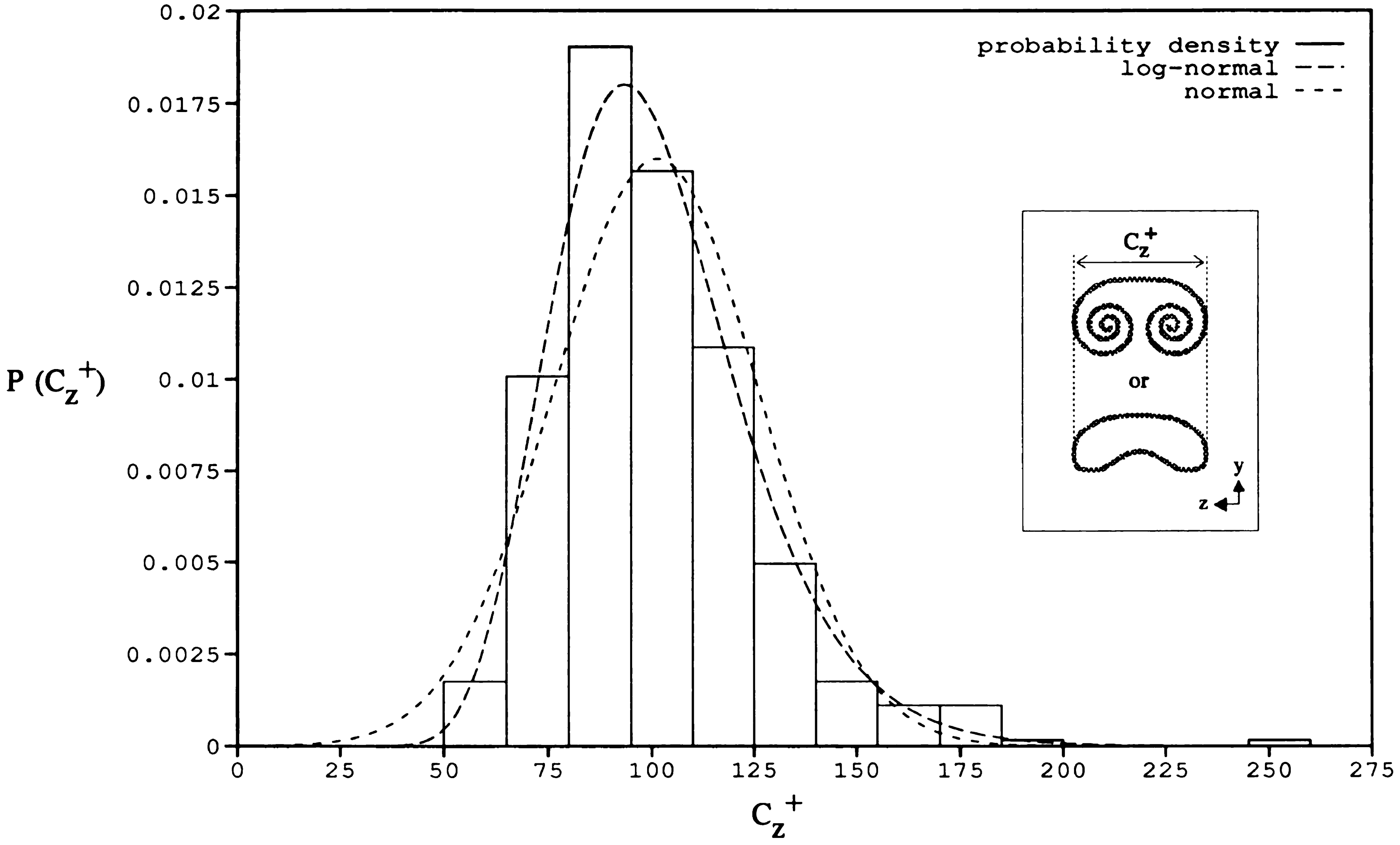

Figure 3.6 The probability density distribution of the spanwise diameter of typical eddies. The dashed lines are the normal and log-normal distributions. The definition sketch shows two probable appearances of typical eddies in the cross-stream view.

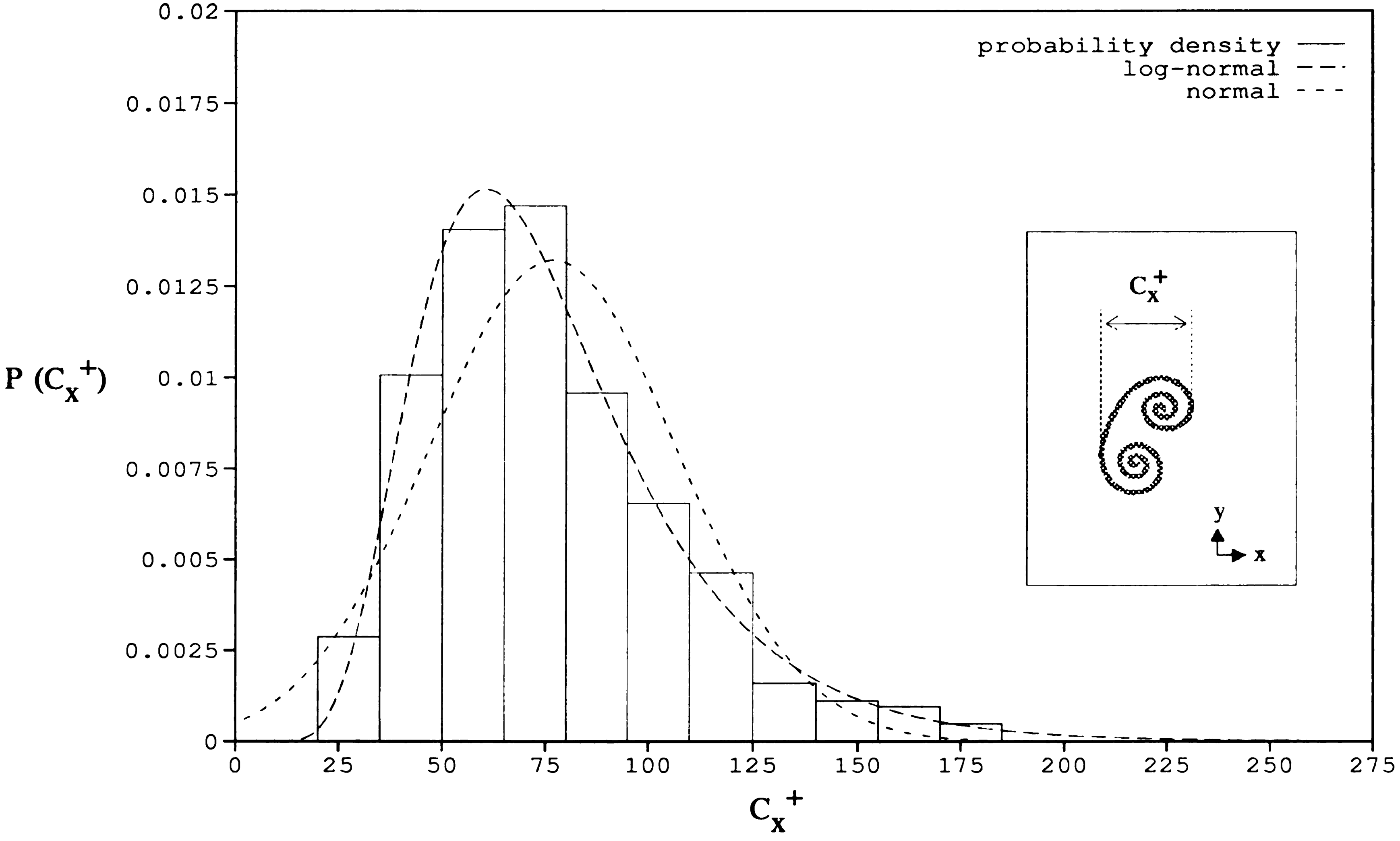

Figure 3.7 The probability density distribution of the streamwise length scale of typical eddies. Normal and log-normal distributions are also shown in dashed lines.

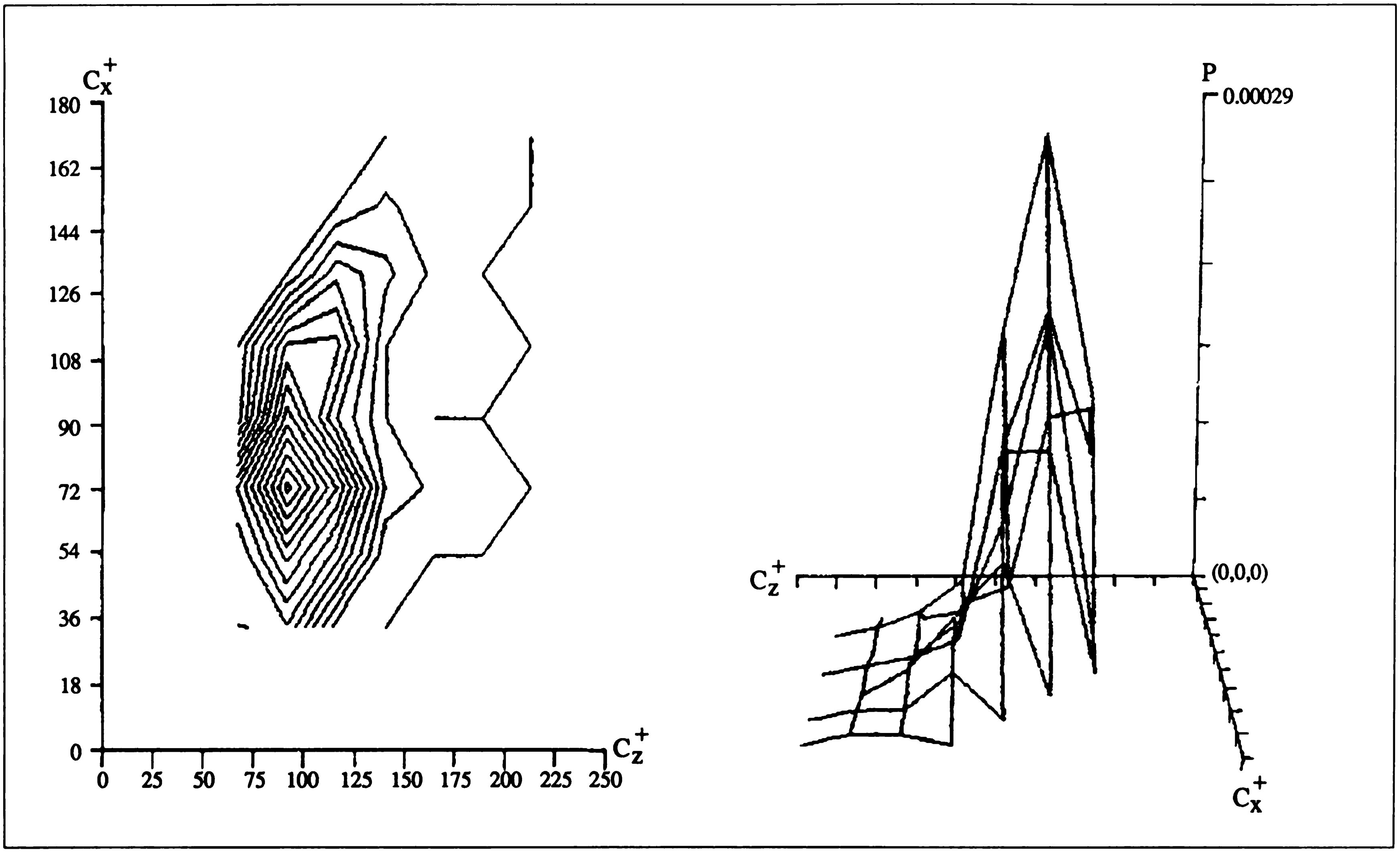

Figure 3.8 2-D probability contour map and 3-D probability density distribution of random variables, C_z^+ and C_x^+ .

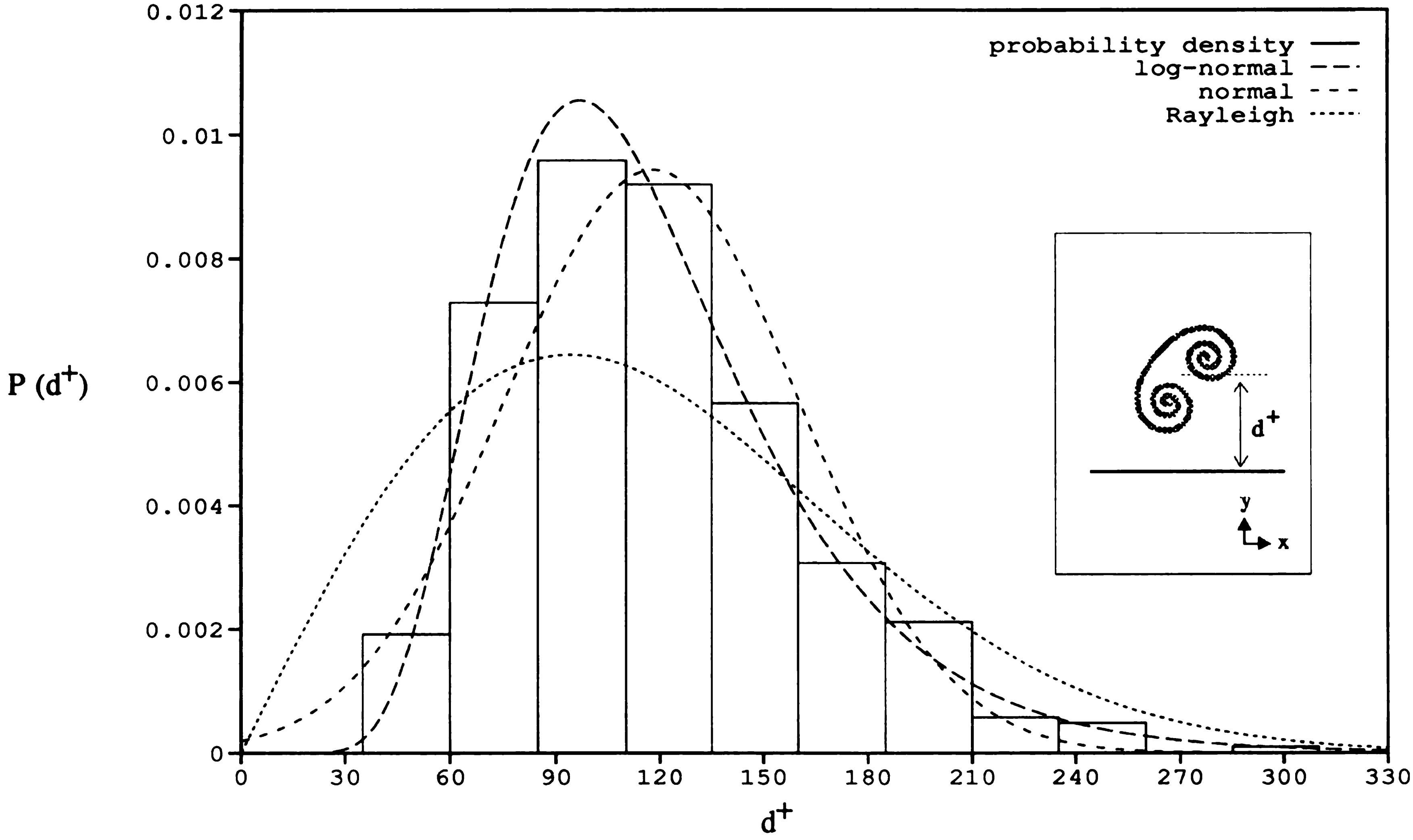

Figure 3.9 The probability density distribution for the distance of typical eddies from the wall. The dashed lines are the normal, log-normal, and Rayleigh density functions. Definition sketch is also shown. Sample size is 417.

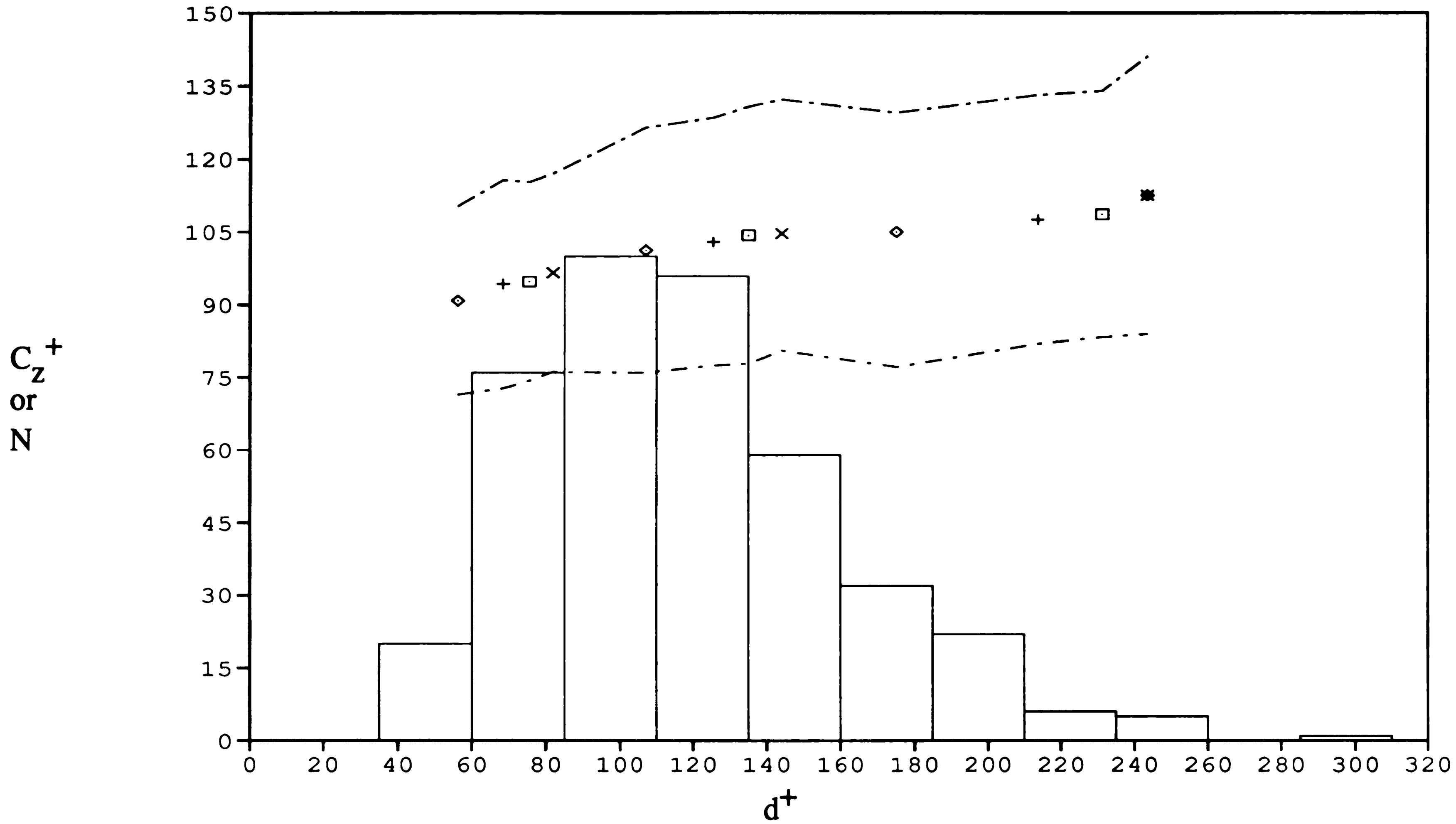

Figure 3.10 The dependence of the spanwise dimension of typical eddy on its distance from the wall. Histogram of d^+'s is also shown. The dot-dashed lines represent the upper and lower bounds of standard deviation of C_z^+. The various symbols used stand for the data obtained by binning processes with various bin widths.

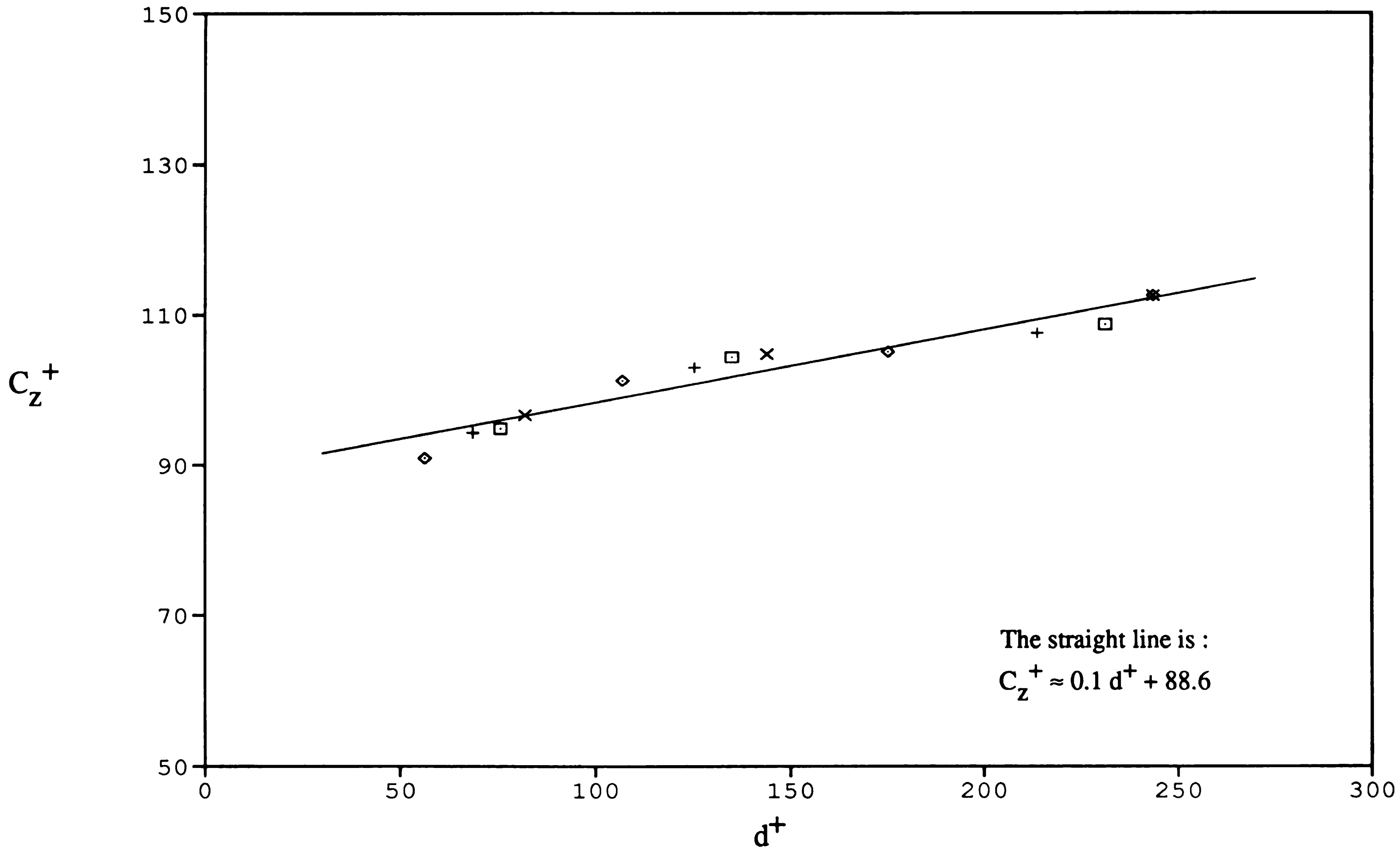

Figure 3.11 A possible linear relationship between the spanwise size of typical eddy and its distance from the wall. The approximation is calculated using the least square method.

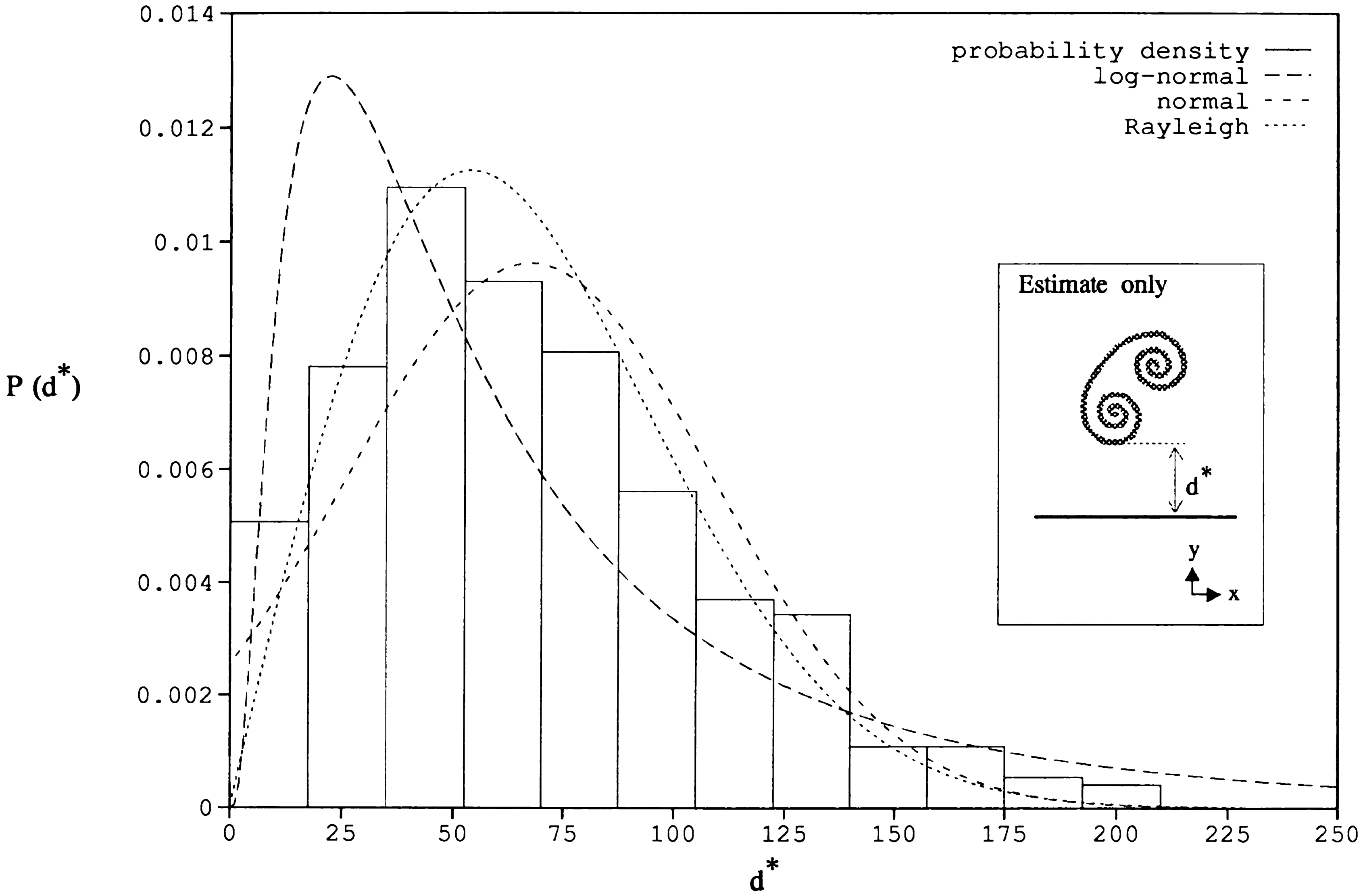

Figure 3.12 The probability density distribution of the normalized distance of typical eddies from the wall. Normal, log-normal, as well as Rayleigh distributions are also shown in dashed lines.

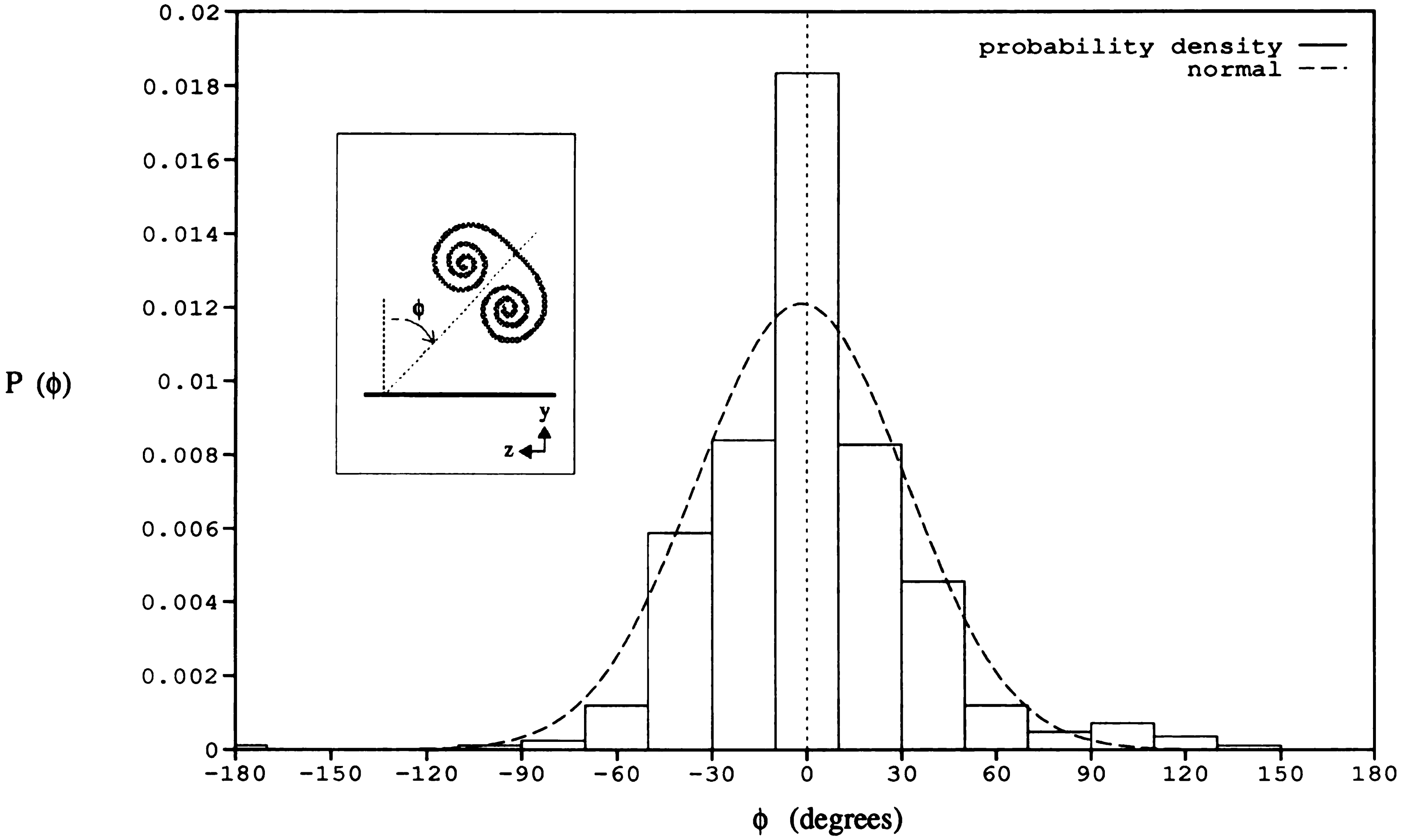

Figure 3.13 The probability density distribution of typical eddy orientation in the cross-stream plane. The curve fit is a normal distribution. Definition sketch is also illustrated.

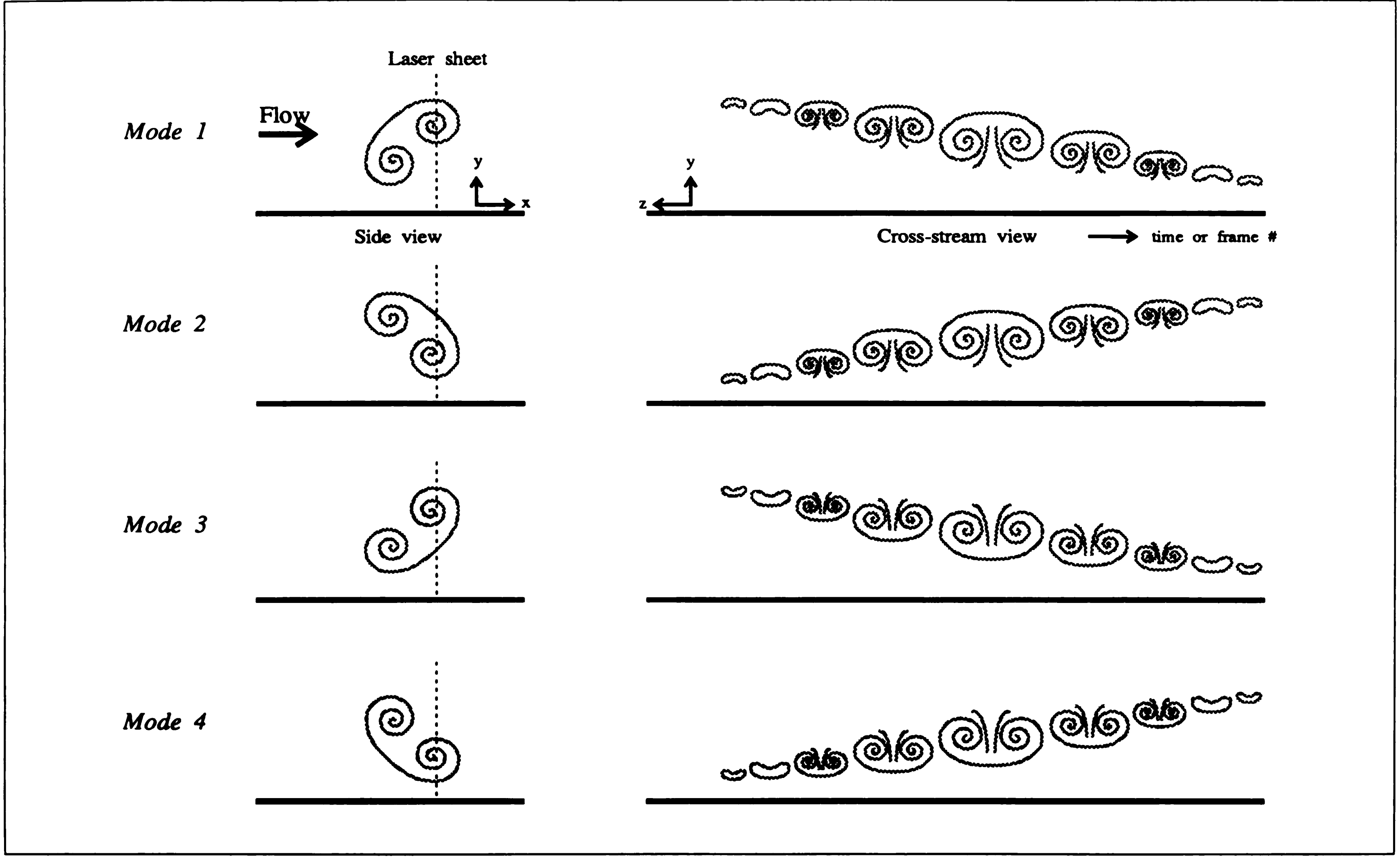

Figure 3.14 Definition sketch of typical eddy characteristic modes based upon its orientation with respect to the wall in the x-y plane. The sequence of the cross-stream views for each typical eddy mode is also illustrated.

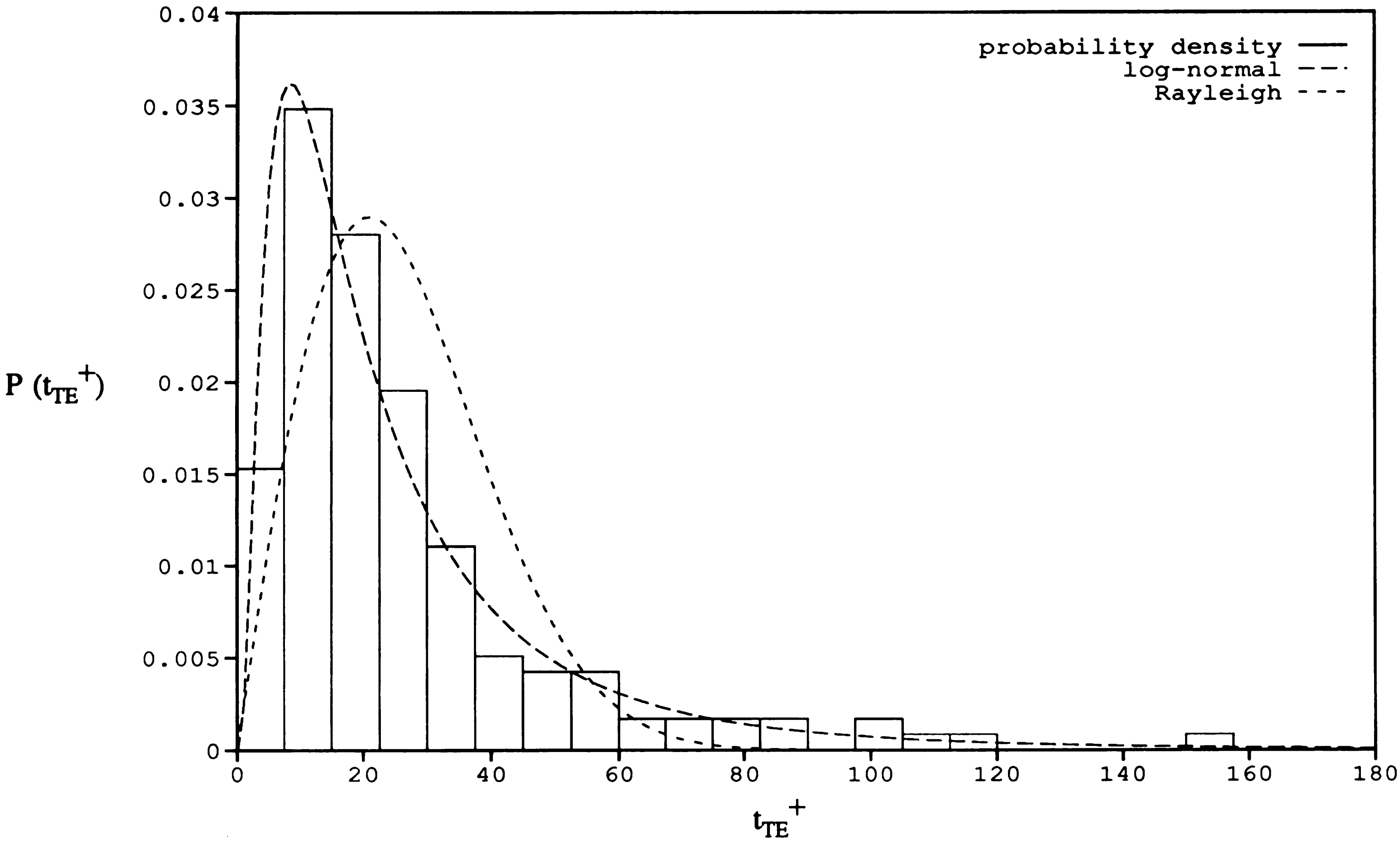

Figure 3.15 The probability density distribution of the period between typical eddy occurrences for $y^+<300$. Log-normal and Rayleigh density functions are also shown to fit the distribution.

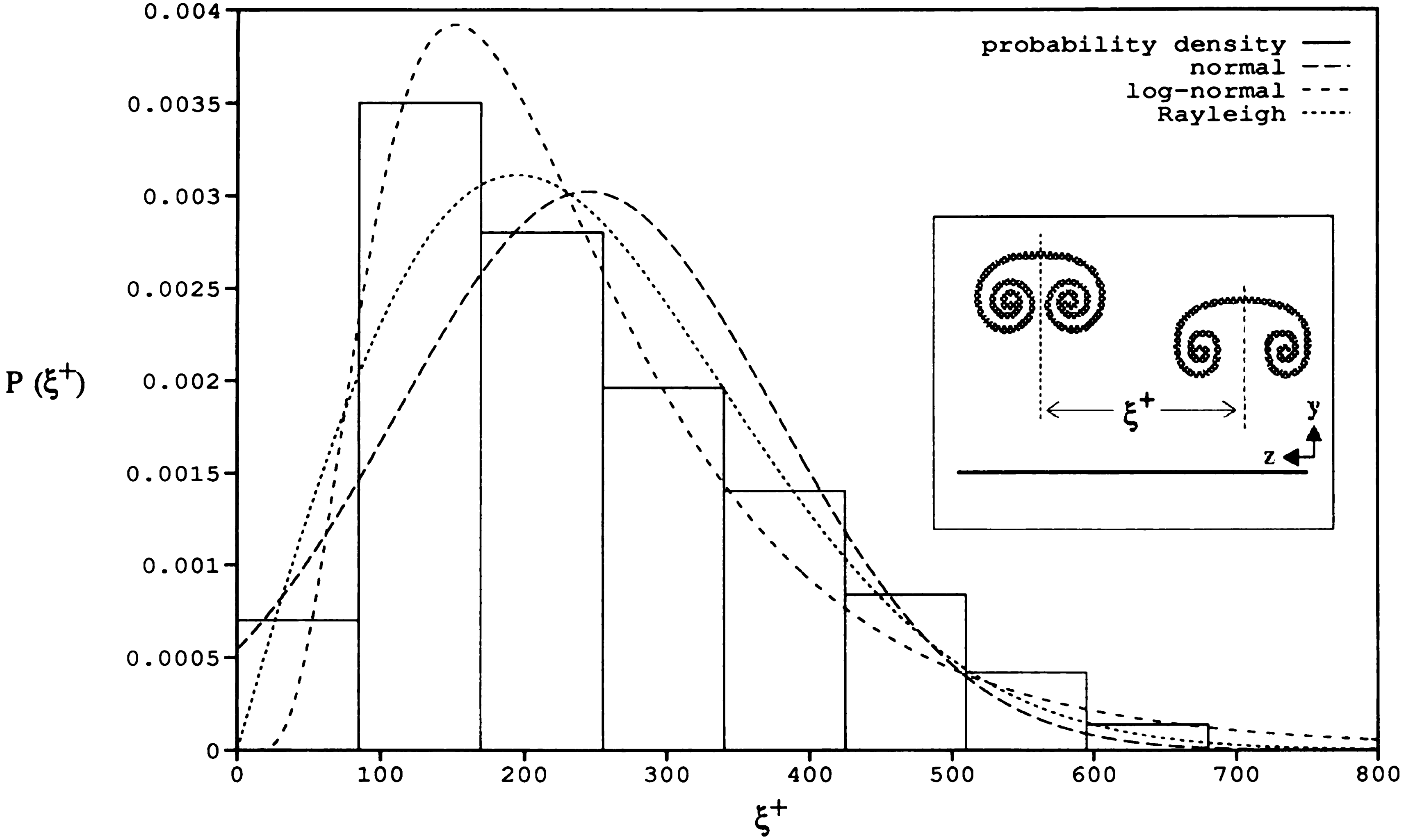

Figure 3.16 The probability density distribution of the center-to-center spacing in the spanwise direction between neighboring typical eddies. Three density functions are also shown to approximate the data set.

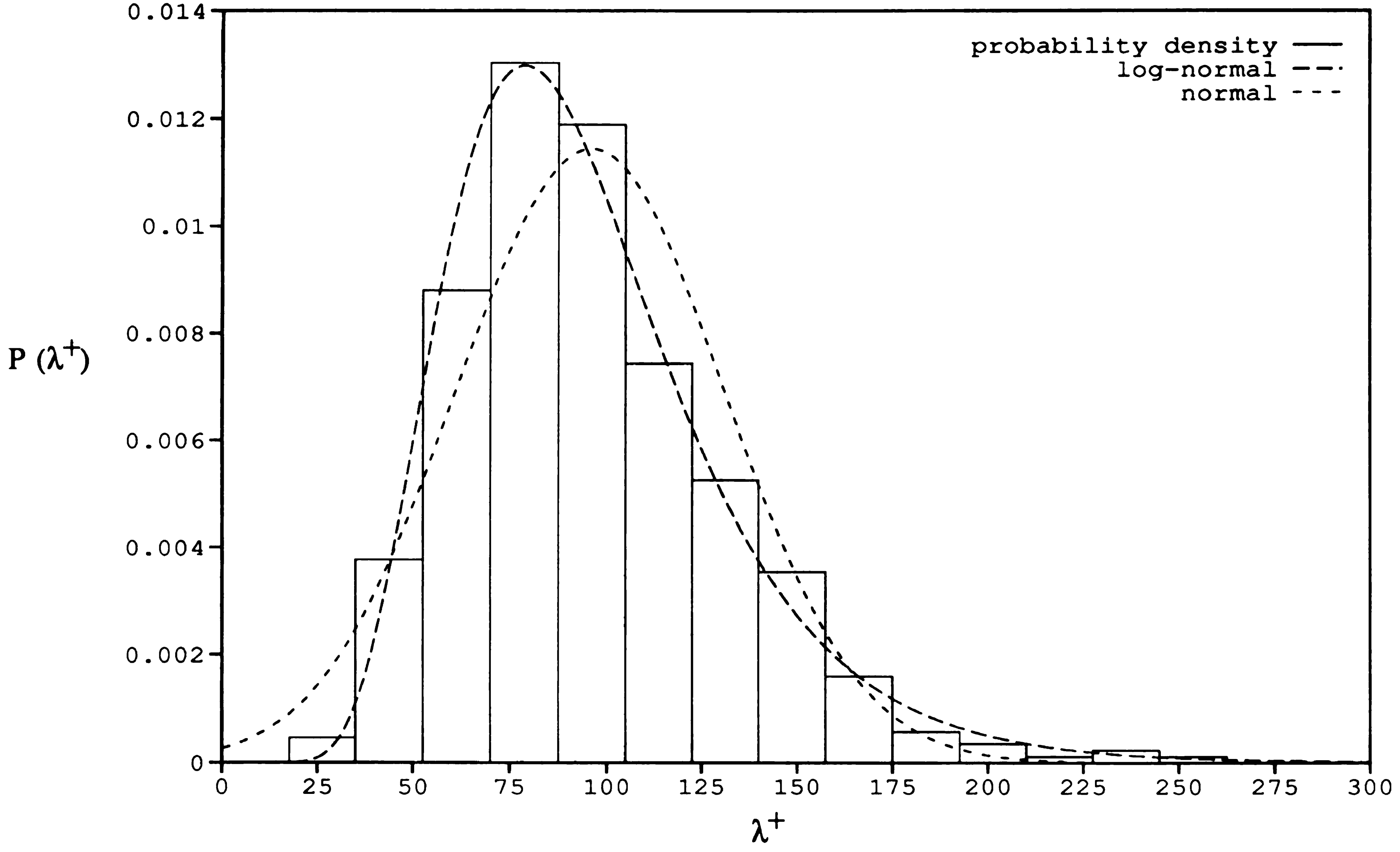

Figure 3.17 The probability density distribution of the spanwise spacing between neighboring low-speed streaks. Normal and log-normal density functions are also plotted to fit the data. Sample size is 500.

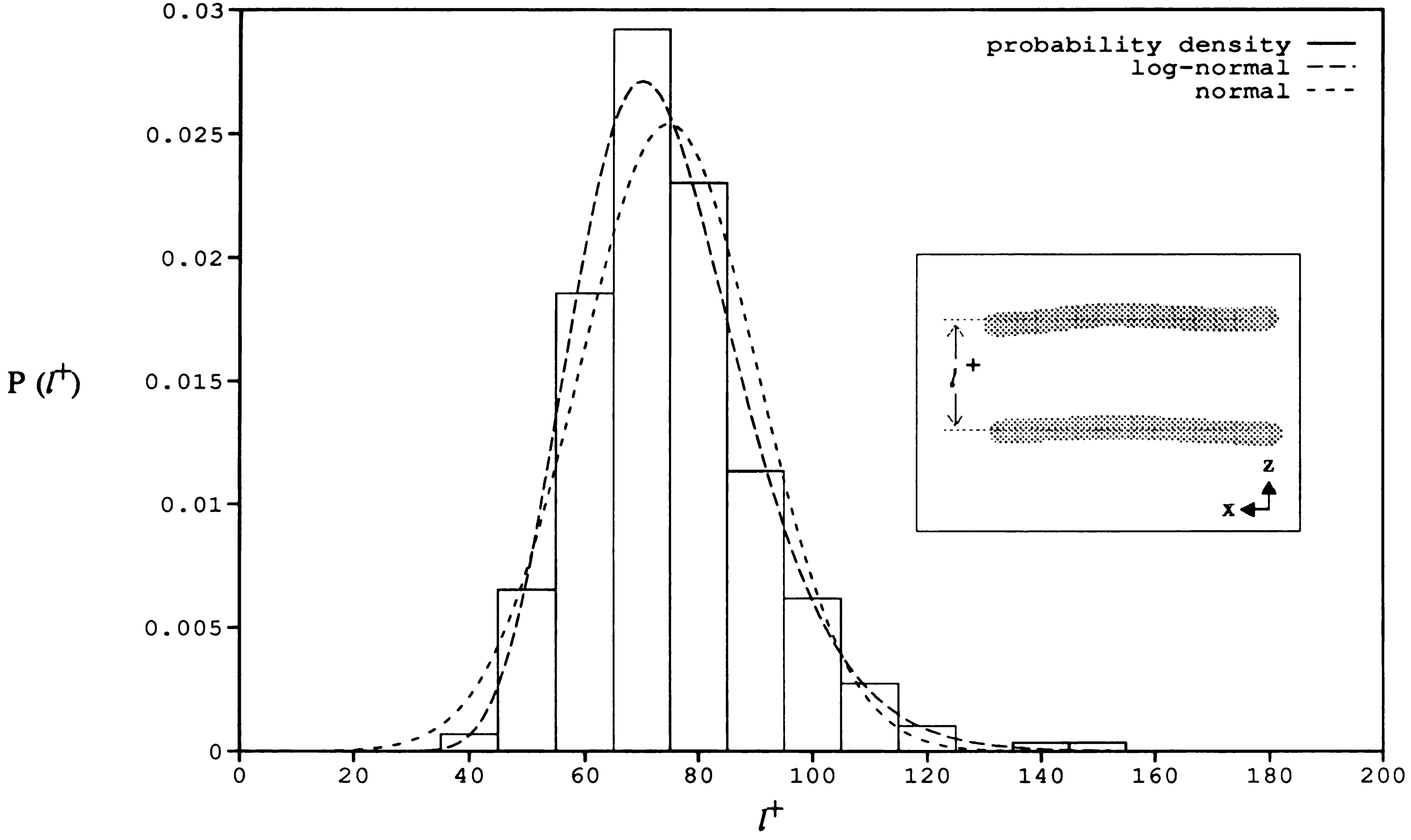

Figure 3.18 The probability density distribution of the sublayer streak-pair spacings in the spanwise direction. Normal and log-normal density functions are also presented to fit the data set. Definition sketch illustrates that the measurements were the average distances between the most dense lines.

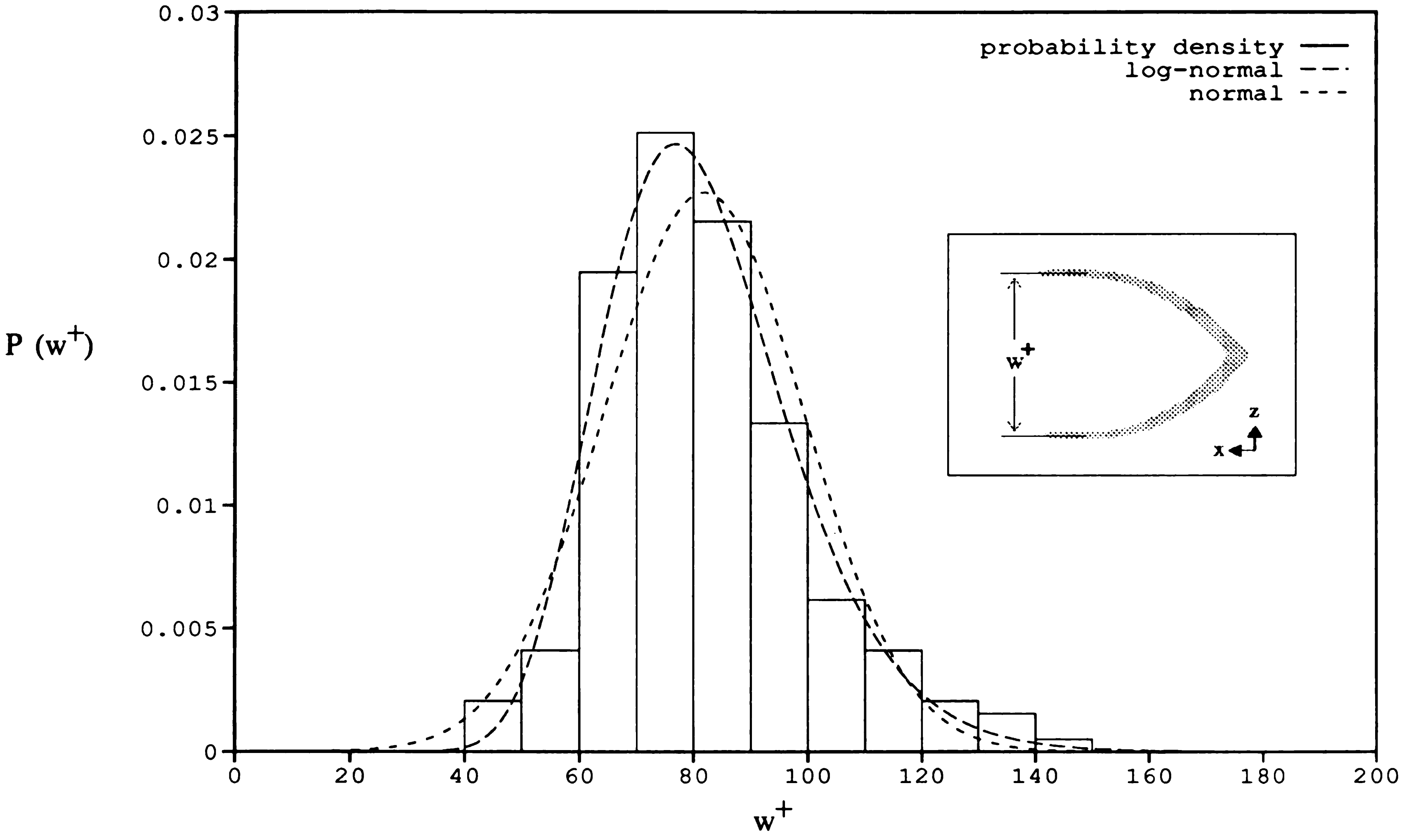

Figure 3.19 The probability density distribution of the pocket dimensions in the spanwise direction. The dashed lines are the normal and log-normal distributions. Definition sketch shows that the measurements were taken between the most dense lines.

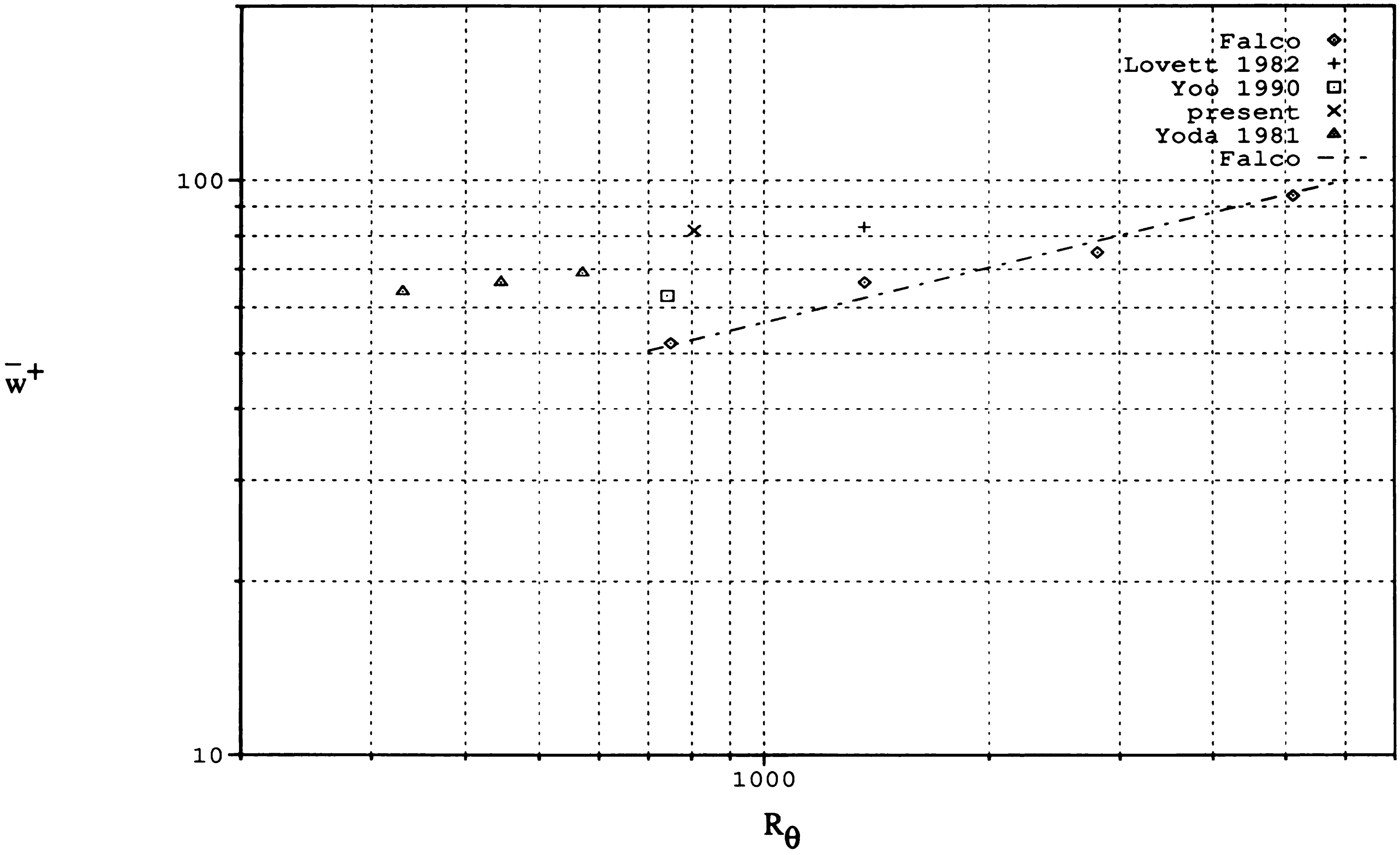

Figure 3.20 The comparison of the mean spanwise dimension of pockets between our data at $R_\theta \approx 805$ and results of many others in a log-log scale.

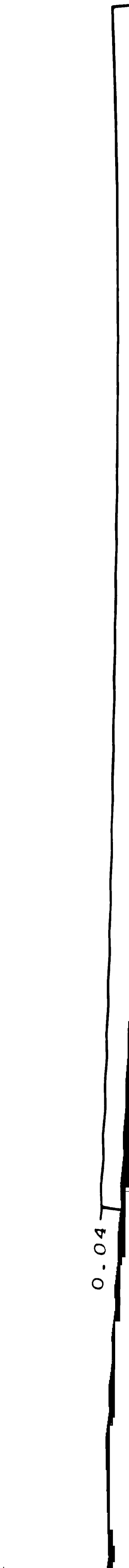
0.04

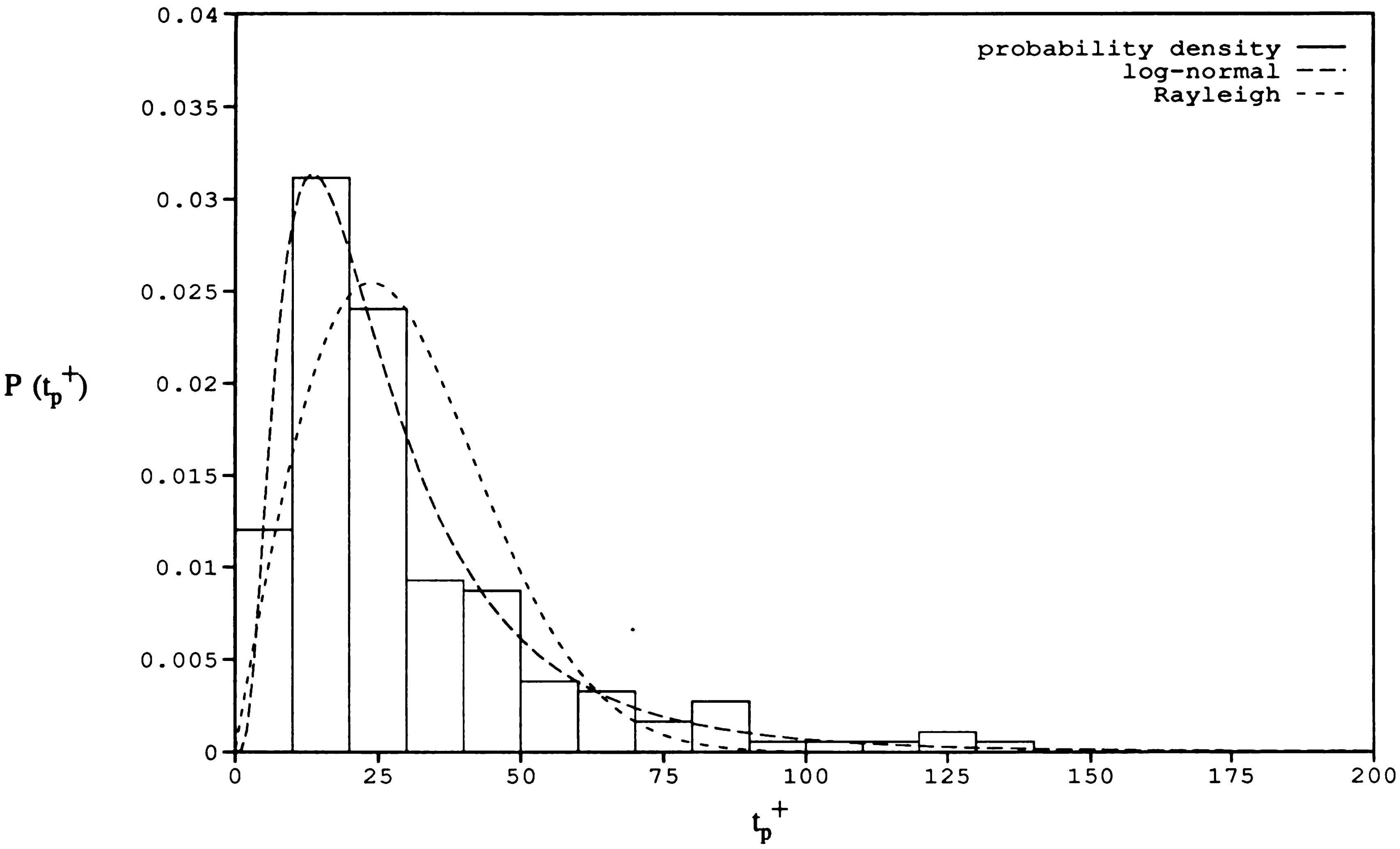

Figure 3.21 The probability density distribution of the period between pocket creations. Log-normal and Rayleigh density functions are also drawn to represent the distribution.

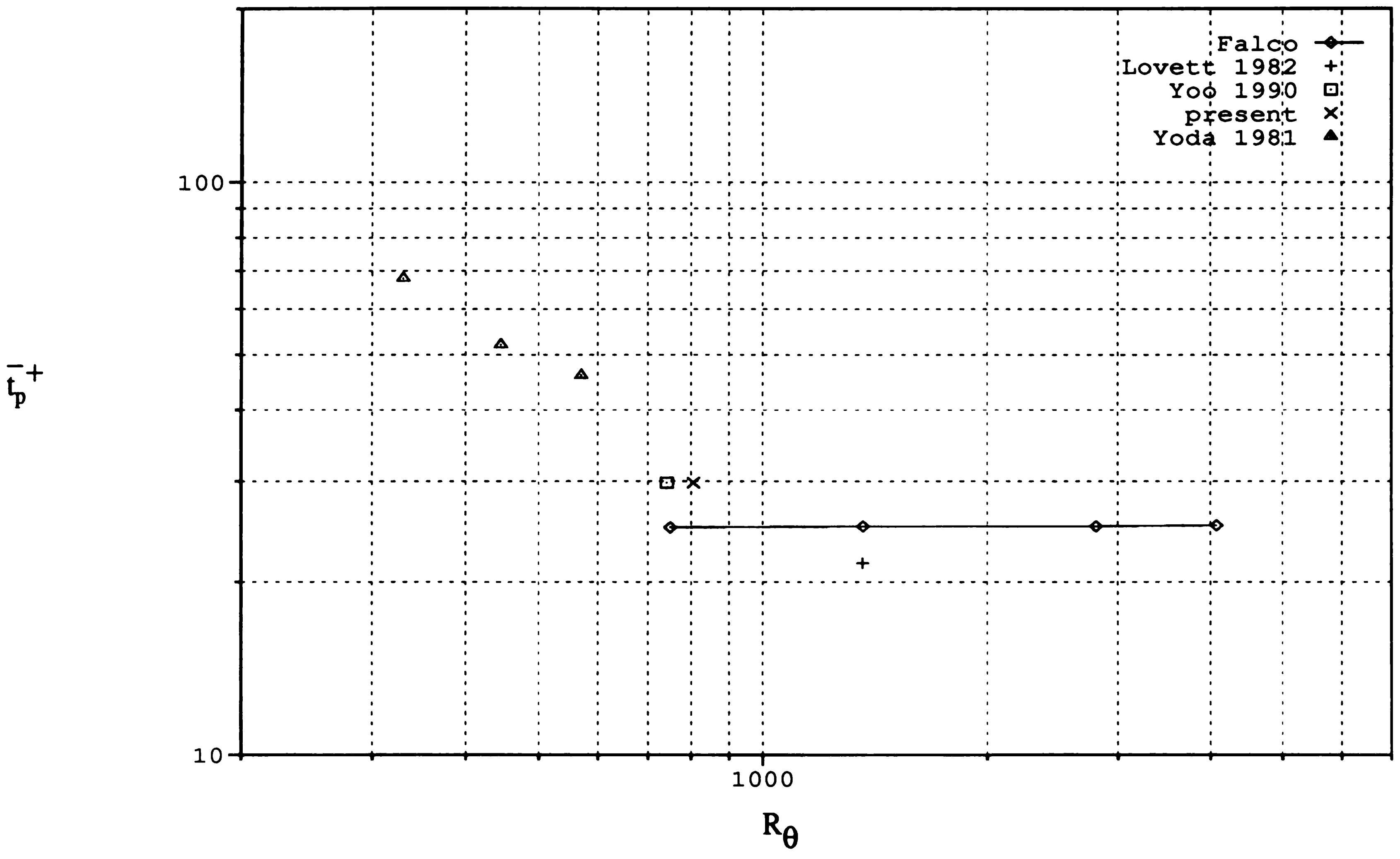

Figure 3.22 The comparison of the period of pocket formations between our measurement at $R_\theta \approx 805$ and results of many others in a log-log scale.

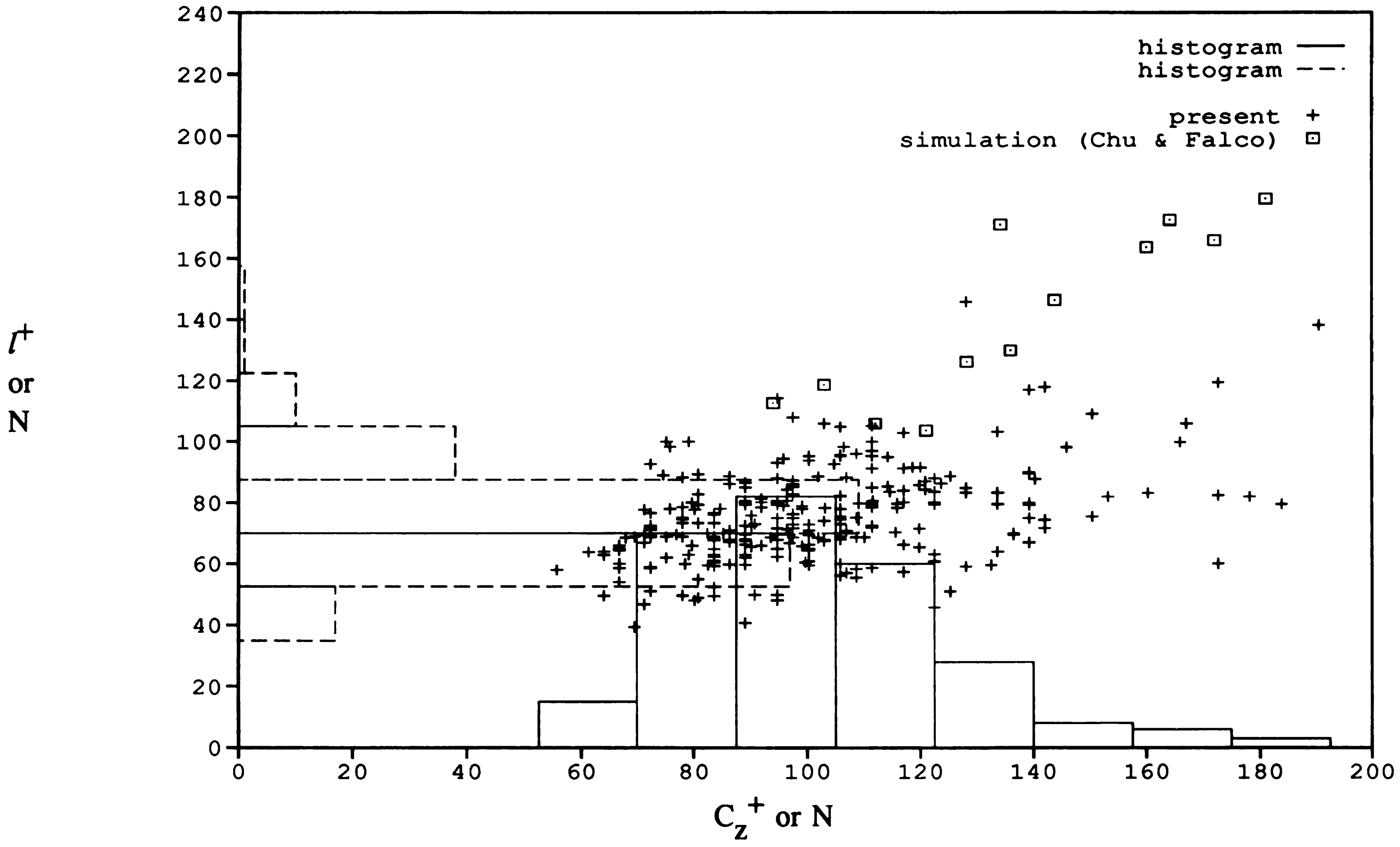

Figure 3.23 The correlation of the typical eddy spanwise diameter and the streak pair spacing. Histograms of both scales are also shown. Simulation data are scaled as l^+ versus D^+(the diameter of ring vortex as it was being generated).

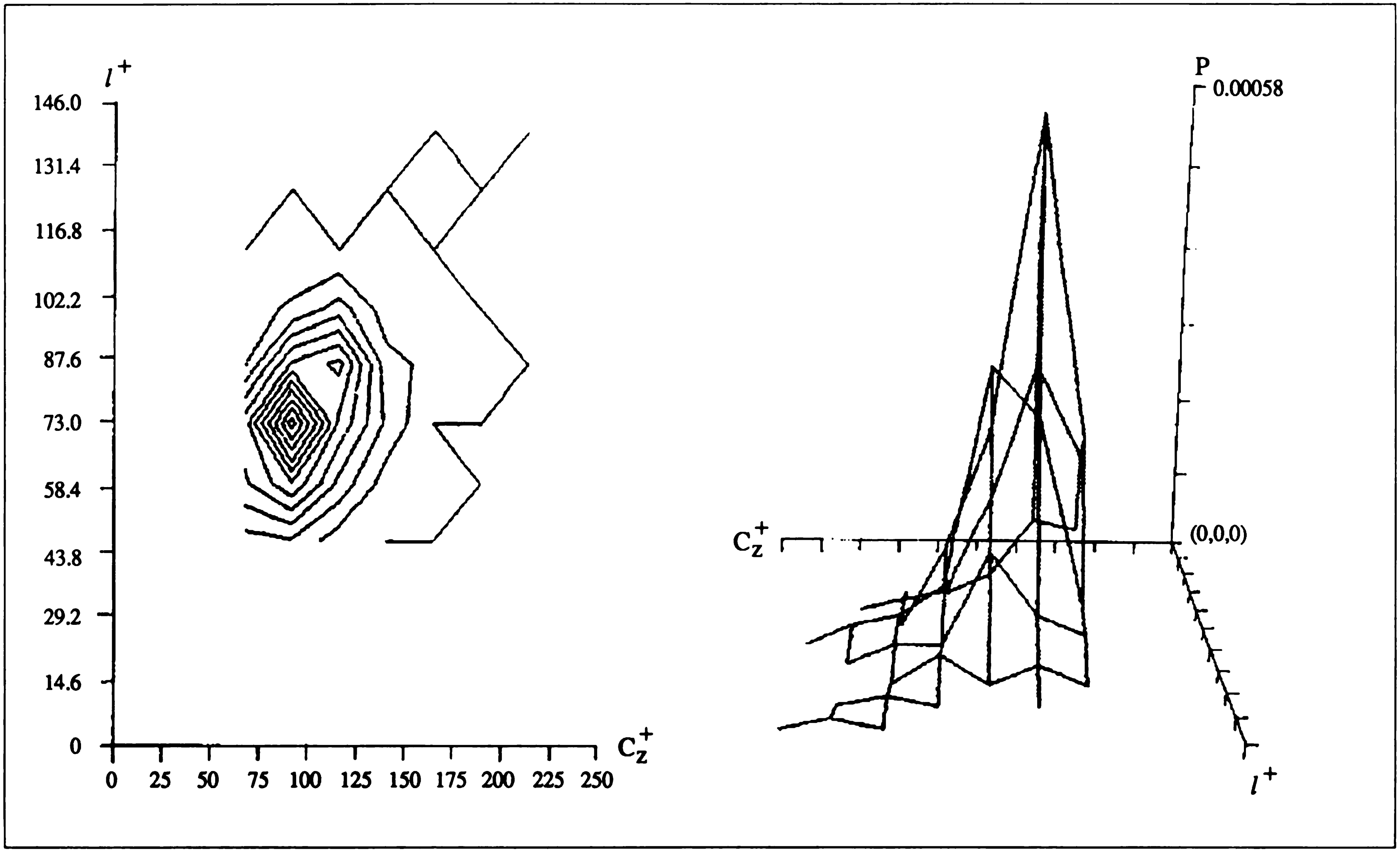

Figure 3.24 2-D probability contour map and 3-D probability density distribution of random variables, C_z^+ and l^+.

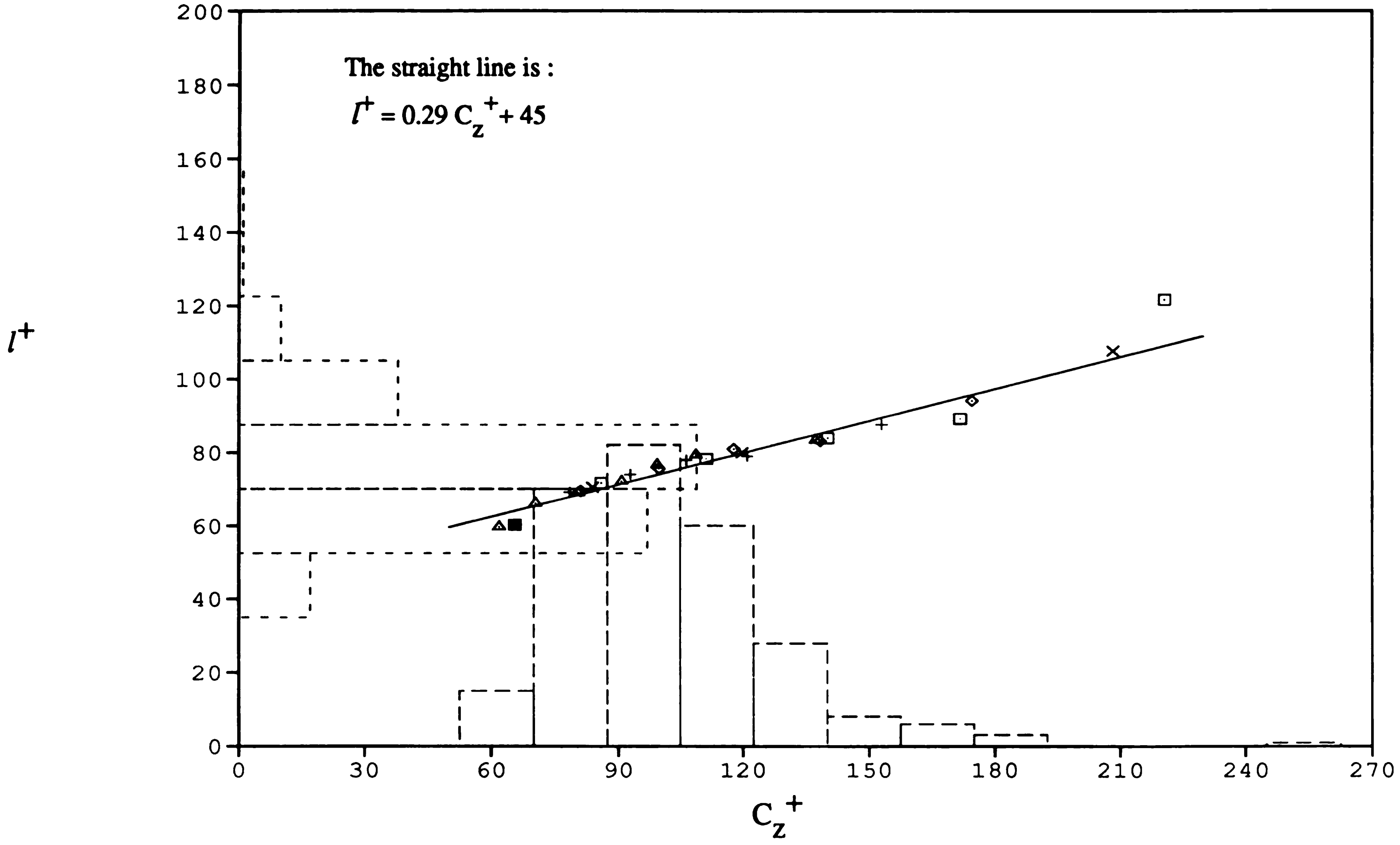

Figure 3.25 The dependence of the streak-pair spacing on the typical-eddy spanwise diameter. Histograms of both scales are also shown. The straight line is the first order least square fit. Various symbols represent that the data are obtained by binning processes based upon various bin widths. Sample size is 273.

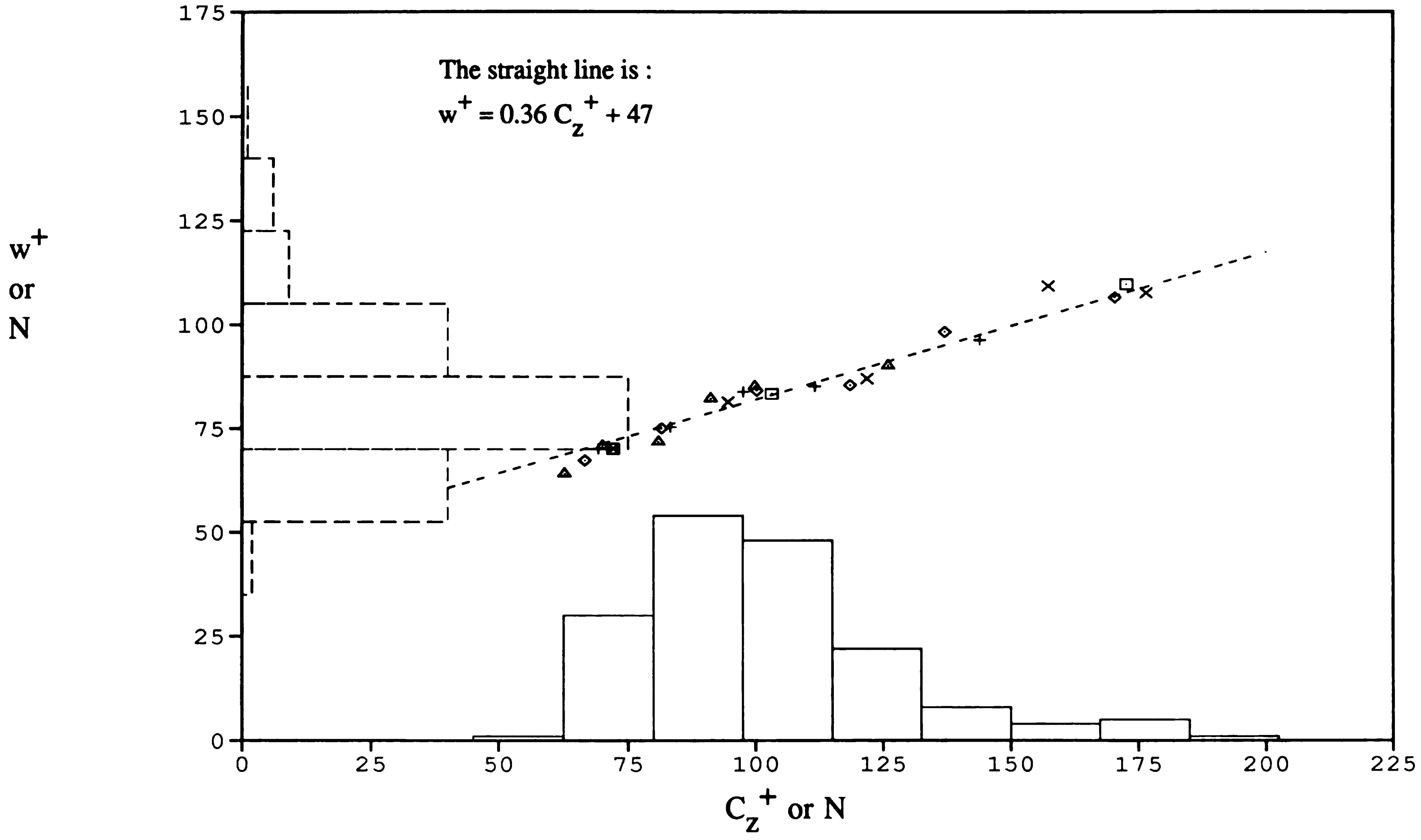

Figure 3.26 The correlation of the spanwise dimensions of typical eddies and pockets. Histograms of both scales are also shown. The linear fit is obtained by first order least square approximation. Various symbols stand for that the data are binned with various bin widths. Sample size is 173.

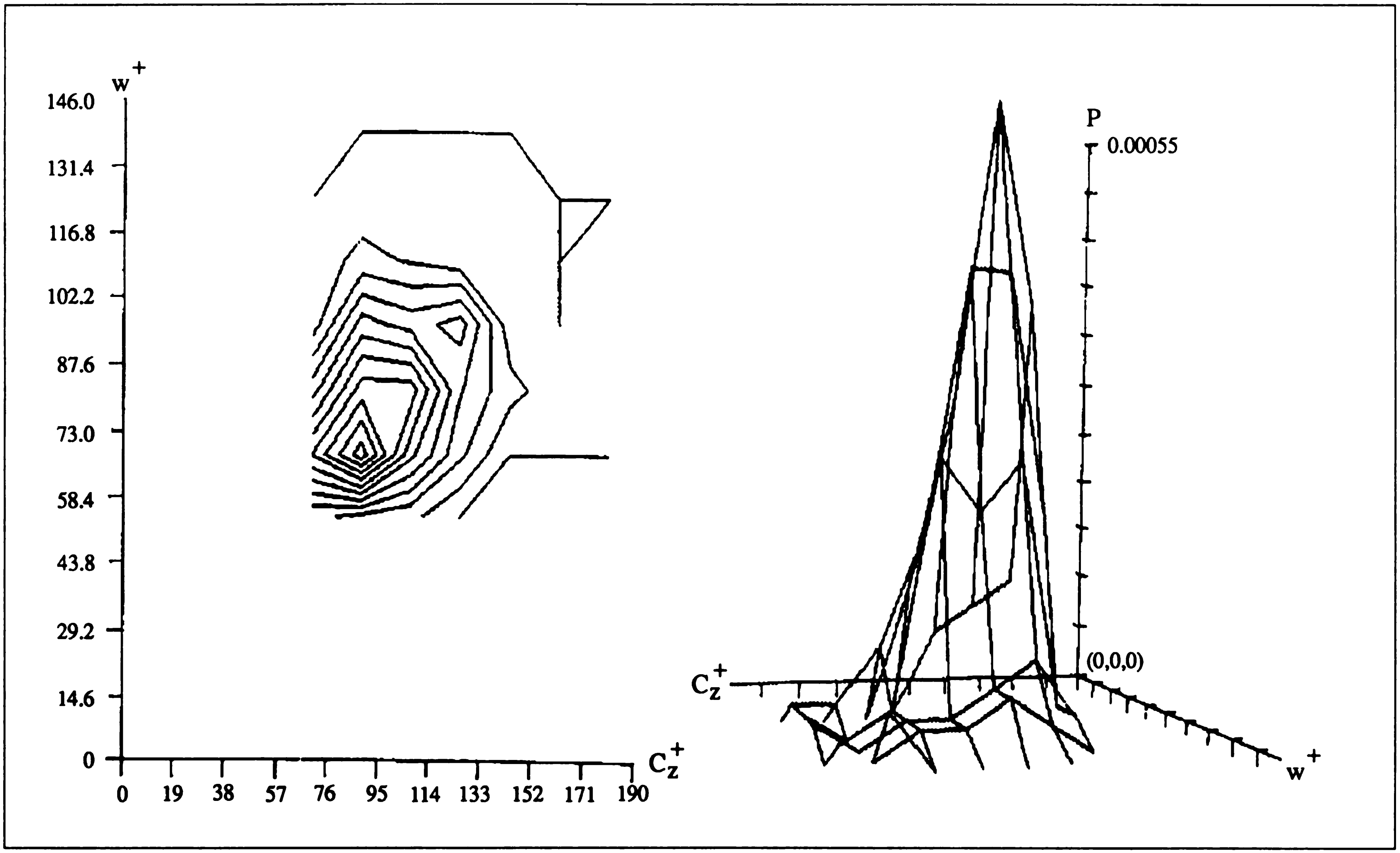

Figure 3.27 2-D probability contour map and 3-D probability density distribution of random variables, C_z^+ and w^+.

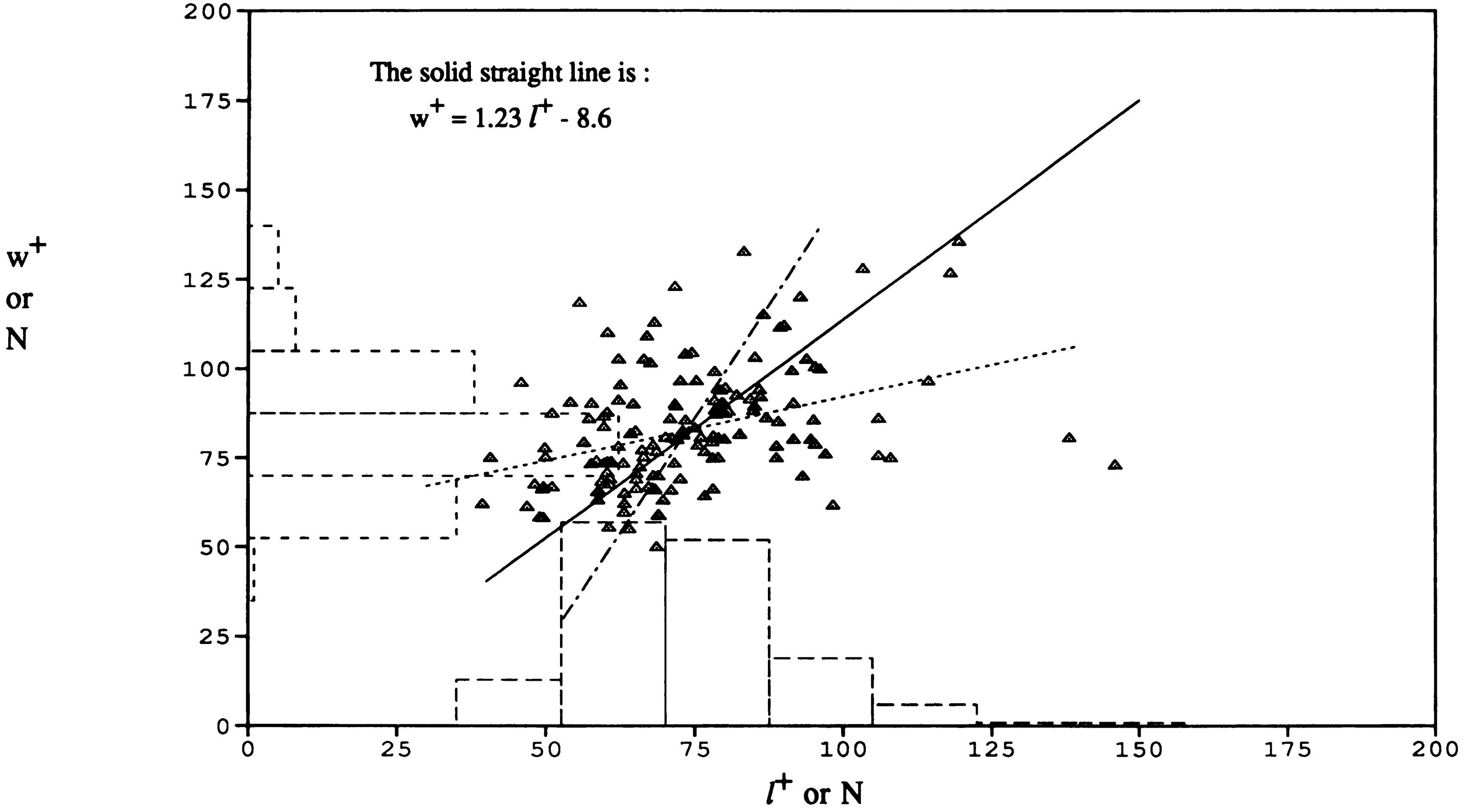

Figure 3.28 The correlation of spanwise dimensions of pockets and sublayer streak pairs under the condition that a typical eddy is observed to propagate over the wall. Histograms of both dimensions are also shown. The solid straight line is obtained using their individual linear relationships with typical eddy. The dashed straight lines are the first order least square fits using either scale as the independent variable (the one with greater slope using w^+ as the independent variable).

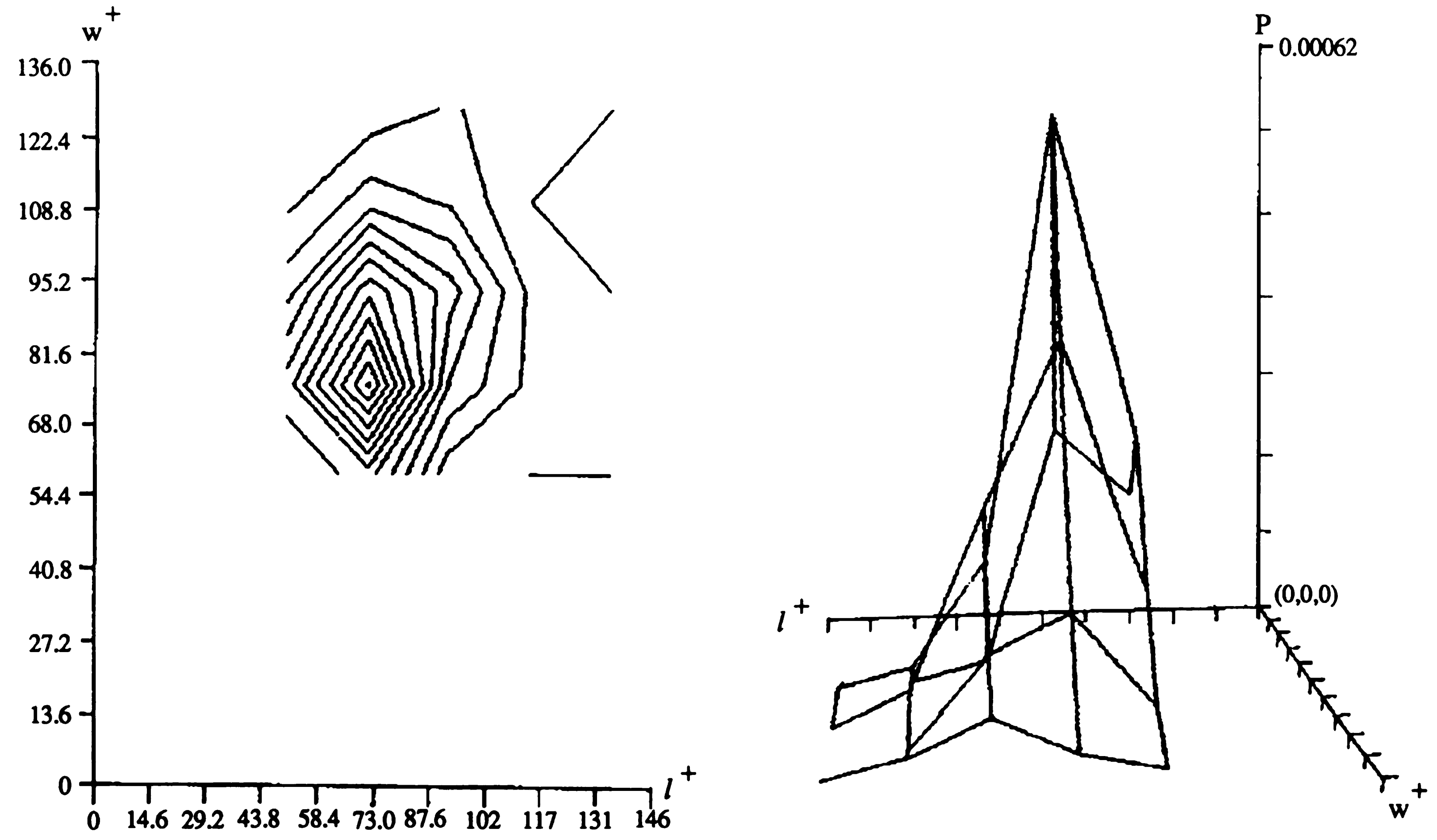

Figure 3.29 2-D probability contour map and 3-D probability density distribution of random variables, l^+ and w^+.

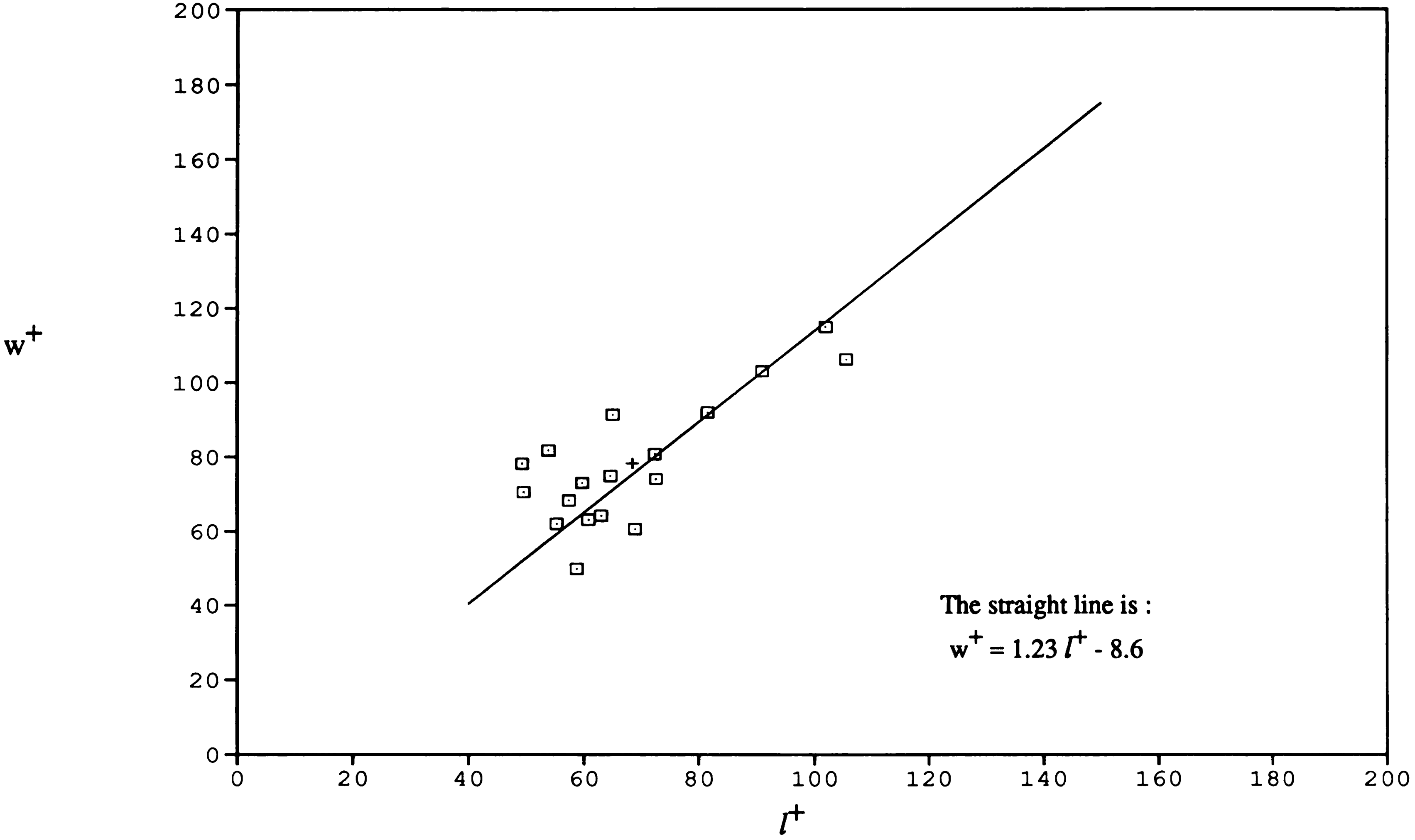

Figure 3.30 The correlation of spanwise dimensions of pockets and sublayer streak pairs in the absence of typical eddy convecting over the wall. The straight line is same to the solid line shown in the previous figure. Mean value of the data is marked as a plus (+). Sample size is 18.

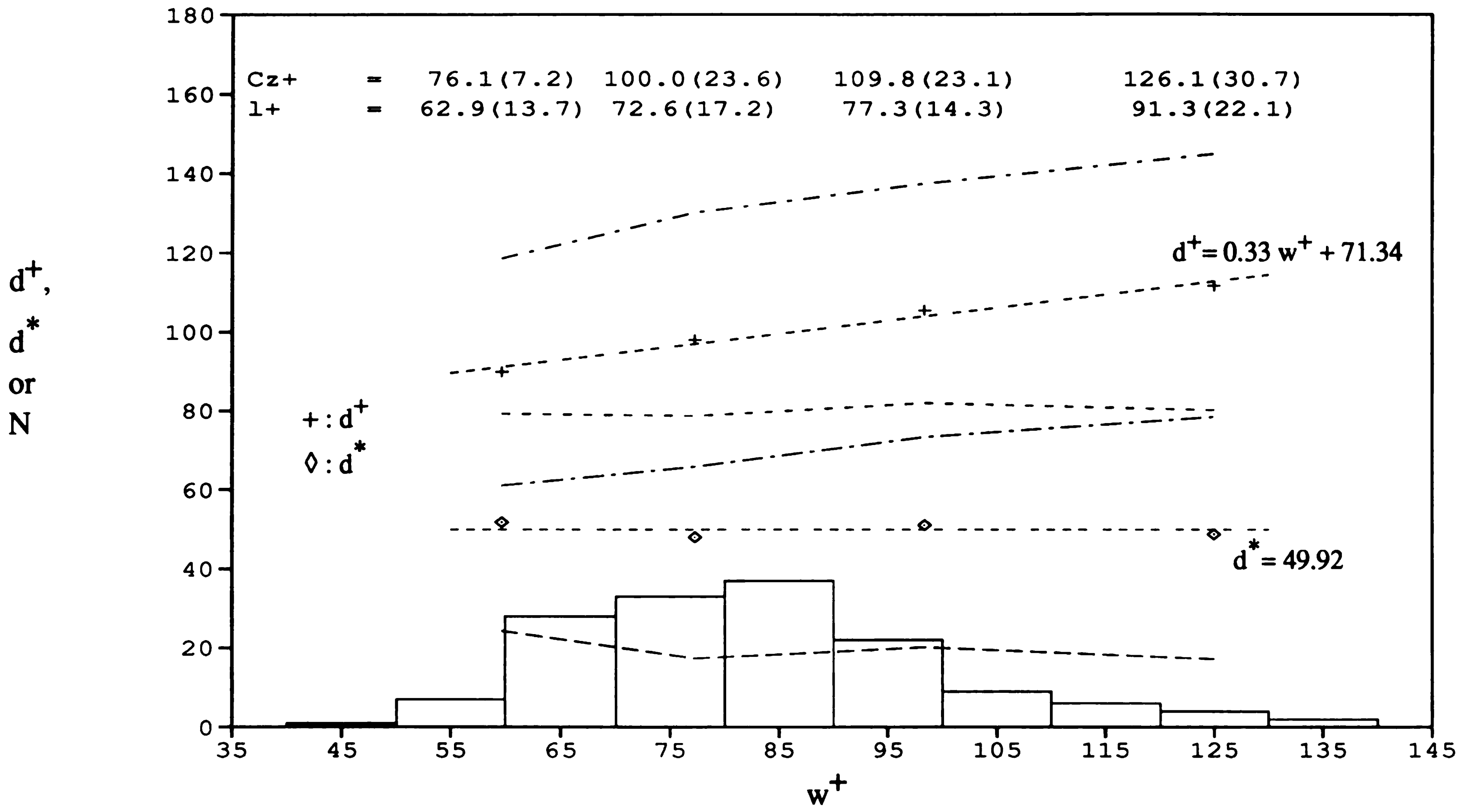

Figure 3.31 The overall length-scale correlation between typical eddies, pockets, and sublayer streak pairs. The dependence of pocket size on the distance or normalized distance of typical eddy from the wall is shown by the data points. The dispersion of the data is indicated by the upper/lower bounds of standard deviation as shown in dashed lines. The histogram of pocket size is also given. The average spanwise dimensions of the corresponding typical eddies and streak pairs for each data point are listed near the top of the figure (standard deviation in brackets). The sample sizes of data points are 16, 91, 34, and 8 (from left to right). Total sample size is 149.

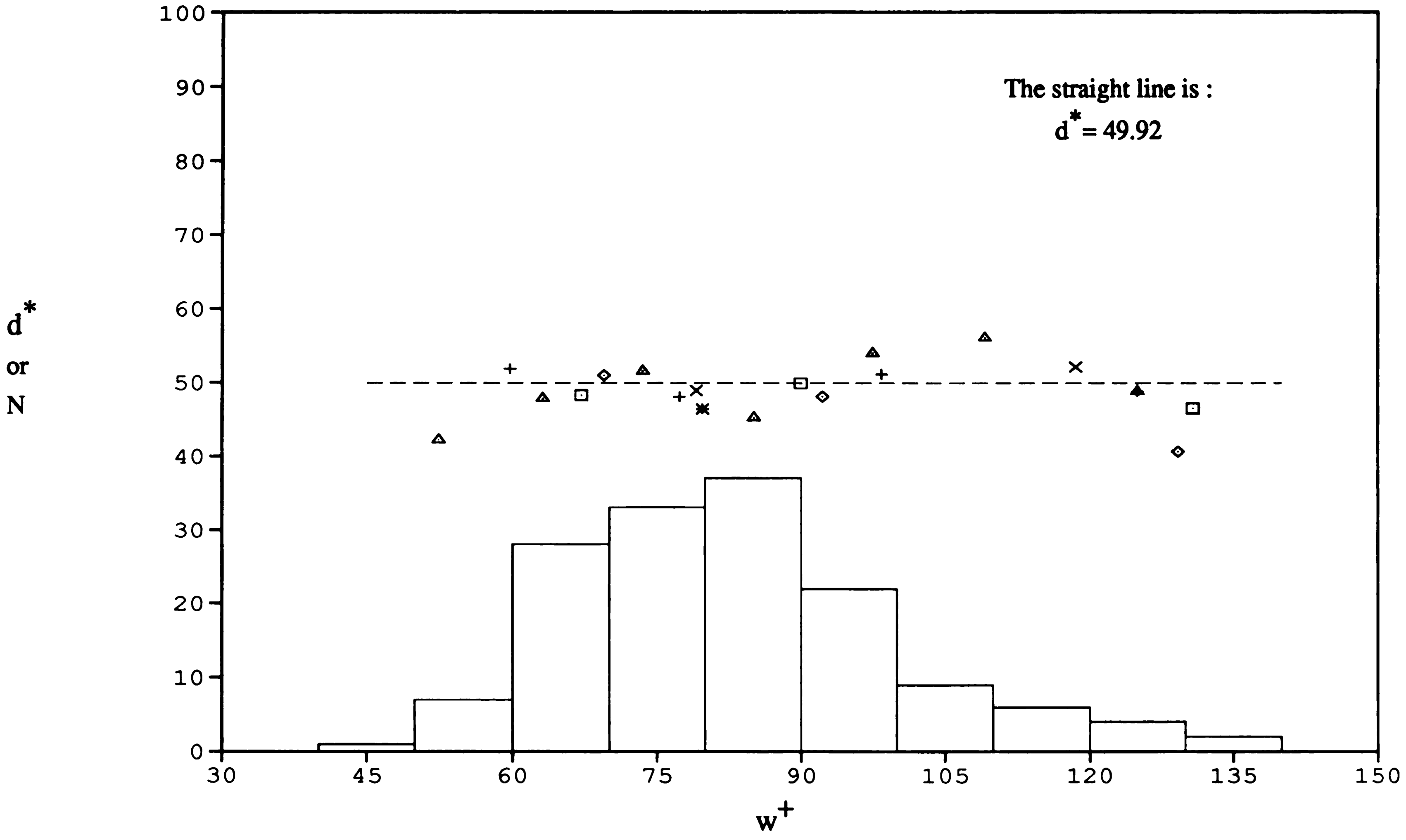

Figure 3.32 The correlation of pocket size (w^+) and normalized distance (d^*) of typical eddies. The histogram of the pocket size is presented as well. Sample size is 149. The mean value for the events in which only pocket was formed is also shown as a star (sample size is 24).

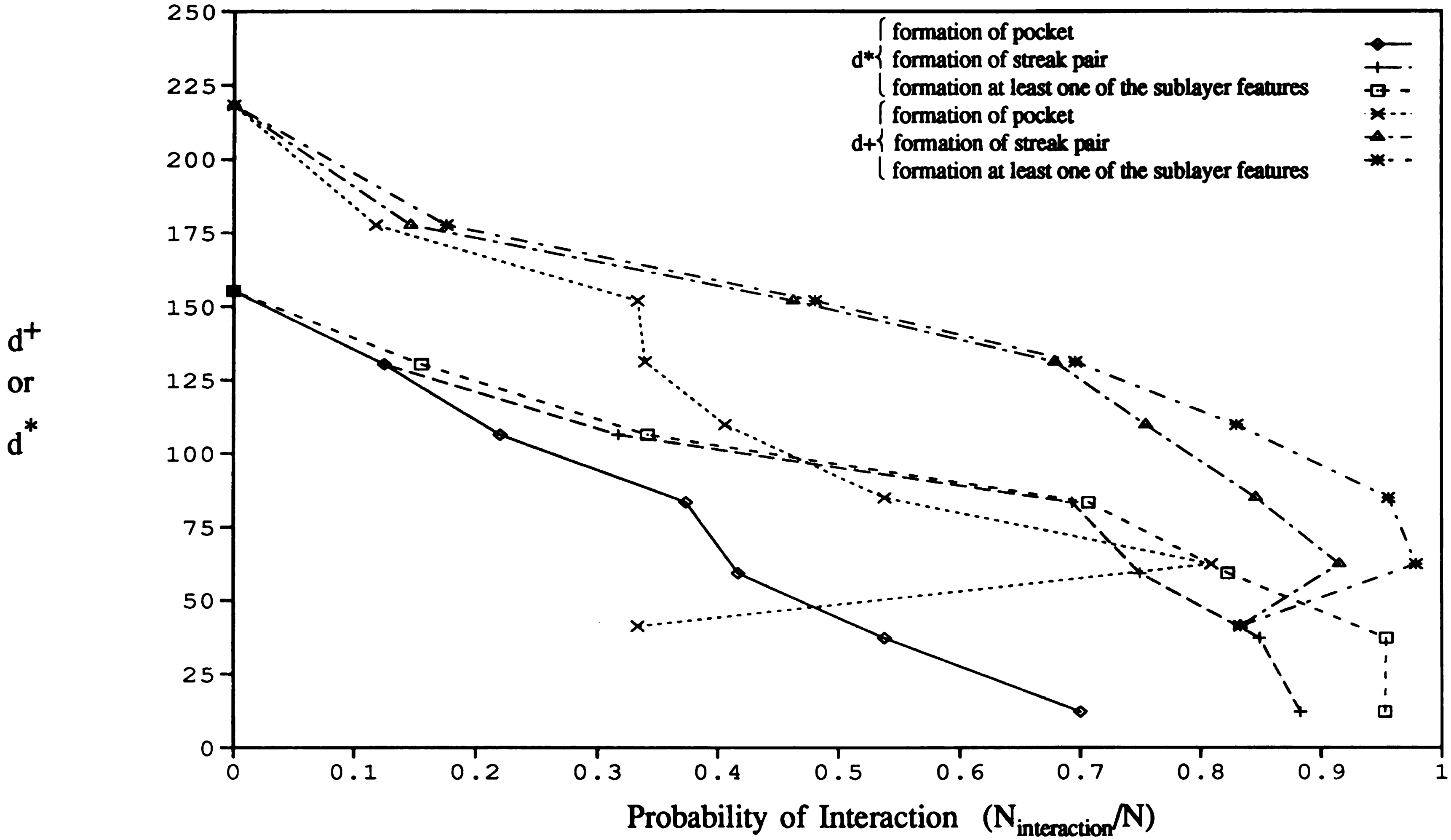

Figure 3.33 The probability of initiating an interaction with the sublayer for typical eddy, based on its distance or normalized distance from the wall. The probability functions based on d^* increase monotonically as d^* decreases. However, the probabilities based on d^+ are not ascending functions for d^+ less than about 70 wall layer units. The intersections of the functions and the vertical axis are approximately 218 and 155 wall layer units for d^+ and d^* respectively. Total sample size is 417.

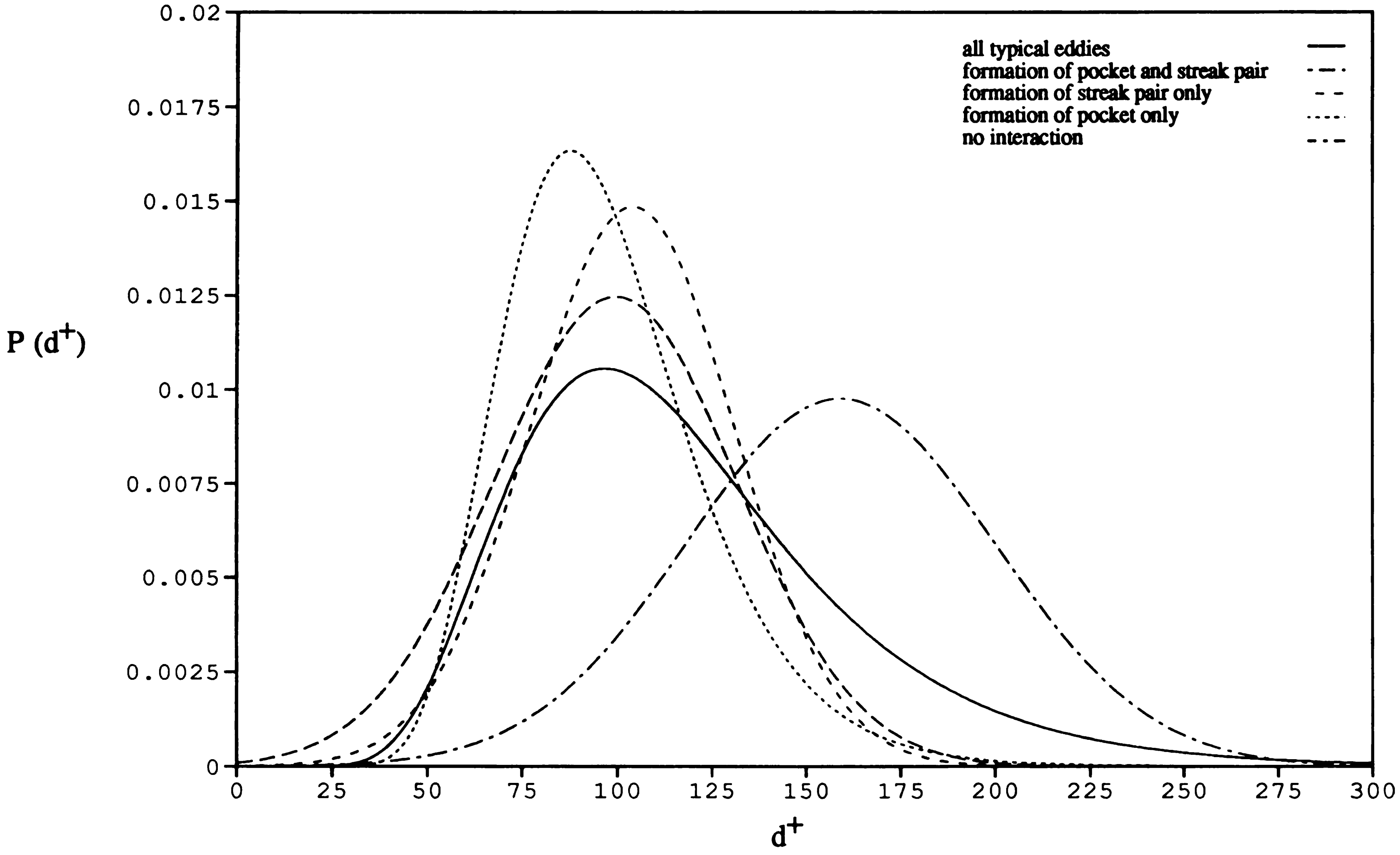

Figure 3.34 The probability density functions for various classes of interactions based upon the distance of typical eddy from the wall.

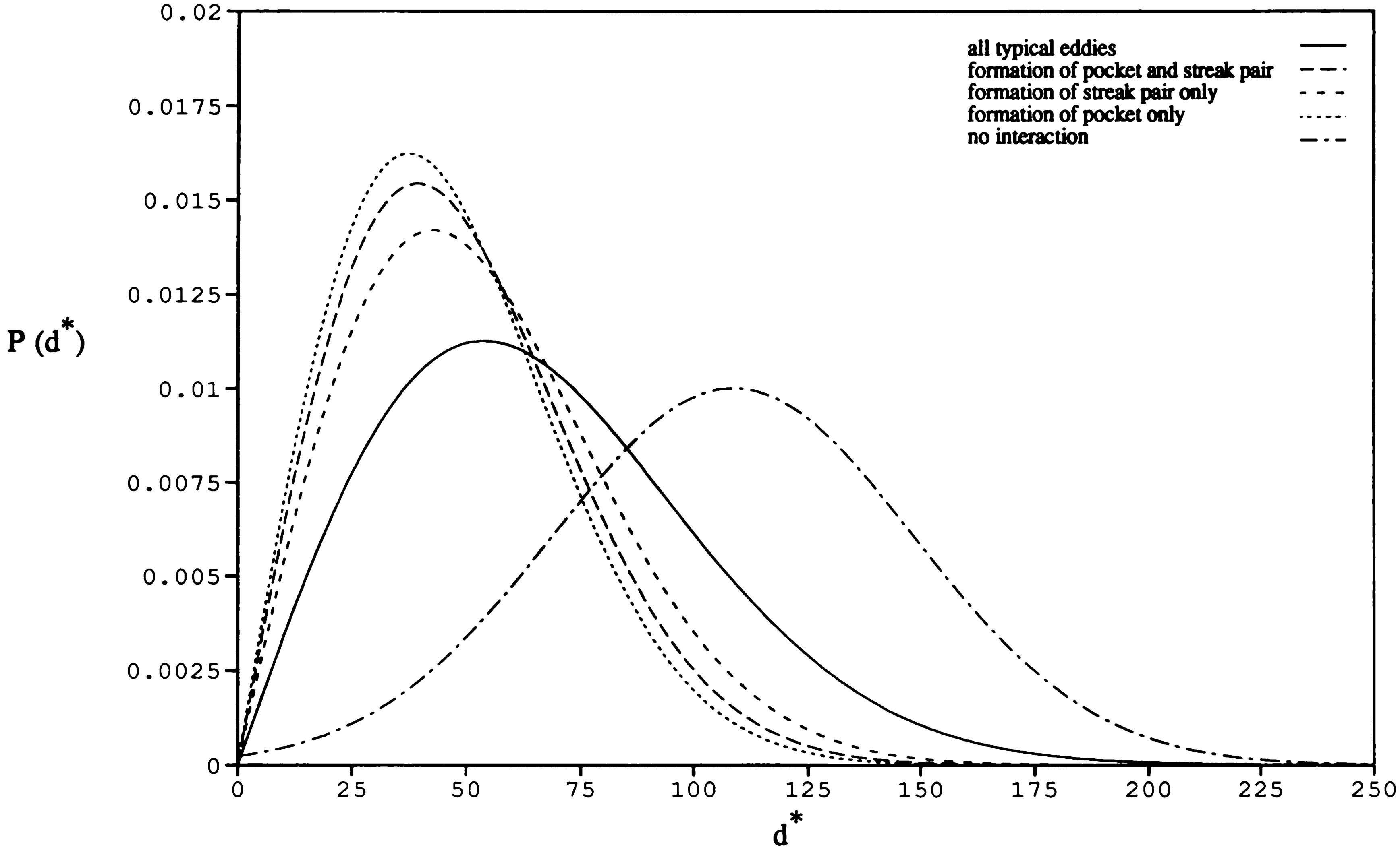

Figure 3.35 The probability density functions for various classes of interactions based upon the normalized distance of typical eddy from the wall.

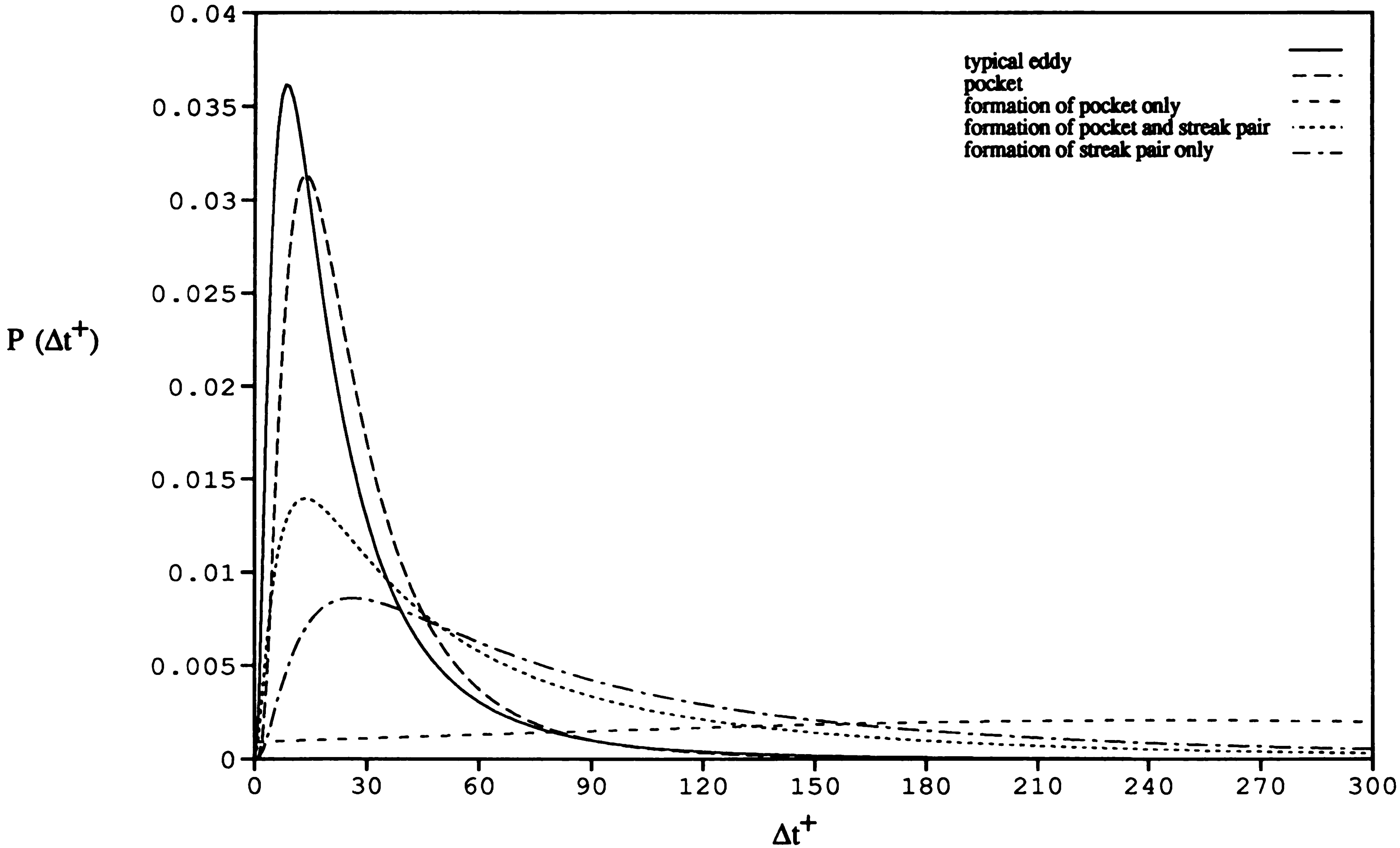

Figure 3.36 The probability density representations of the period between occurrences for various classes of interaction events.

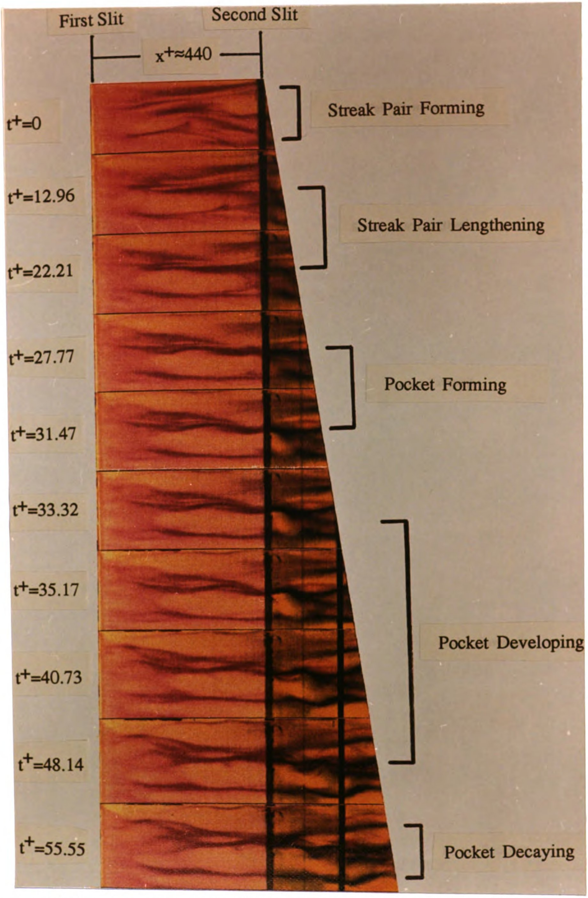

Figure 3.37 Formation of a streak pair and the downstream development of a pocket. Flow is from left to right (similar picture was also present in Falco, Klewicki, and Pan 1989a).

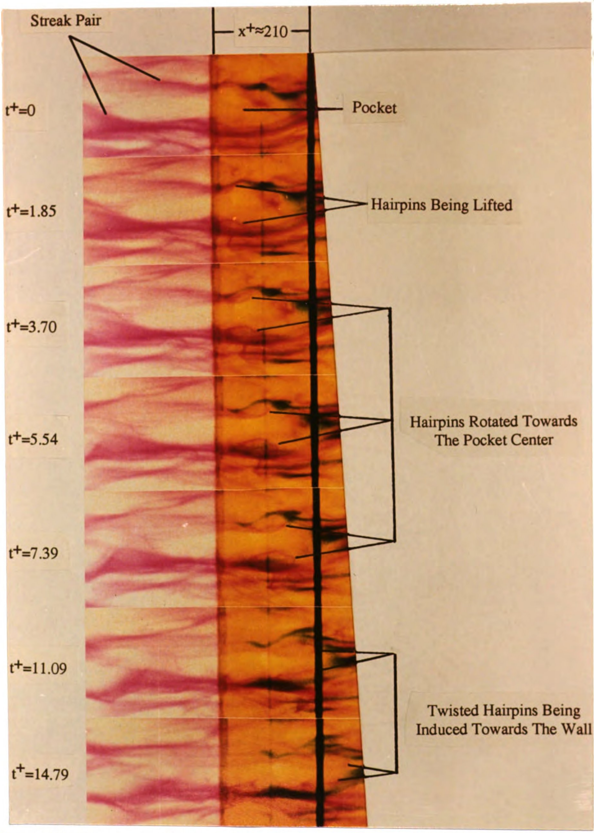

Figure 3.38 Pocket evolution resulting in the engulfment of secondary hairpins that have developed over the streaks. Flow is from left to right (similar picture was also present in Falco, Klewicki, and Pan 1989a).

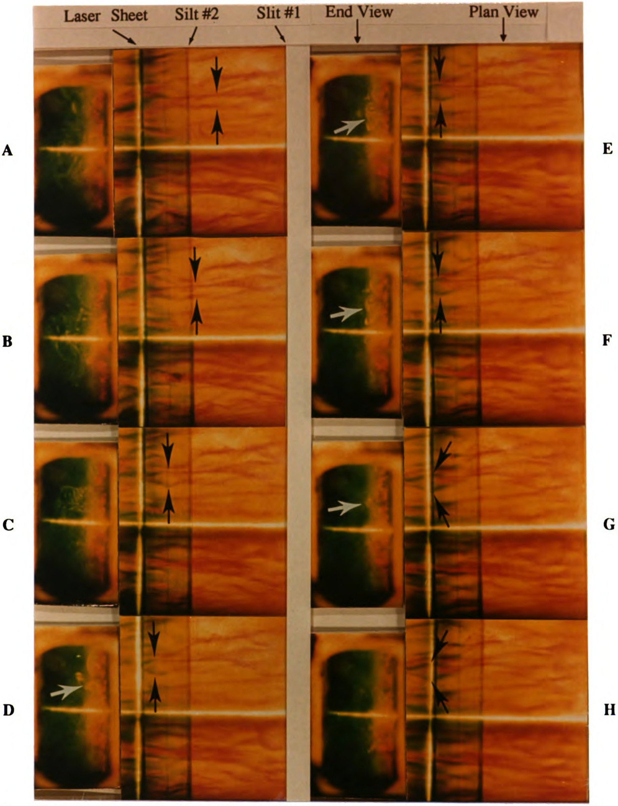

Figure 3.39 A sequence of simultaneous plan and cross-stream views illustrating a typical eddy/wall layer interaction that results in the formation of a pair of long streaks and a pocket near its downstream end. Flow is from right to left for the plan view and into the paper for the cross-stream view. The evolution of the sublayer features is indicated by the black arrows, whereas the appearance of the typical eddy is indicated by the white arrow.

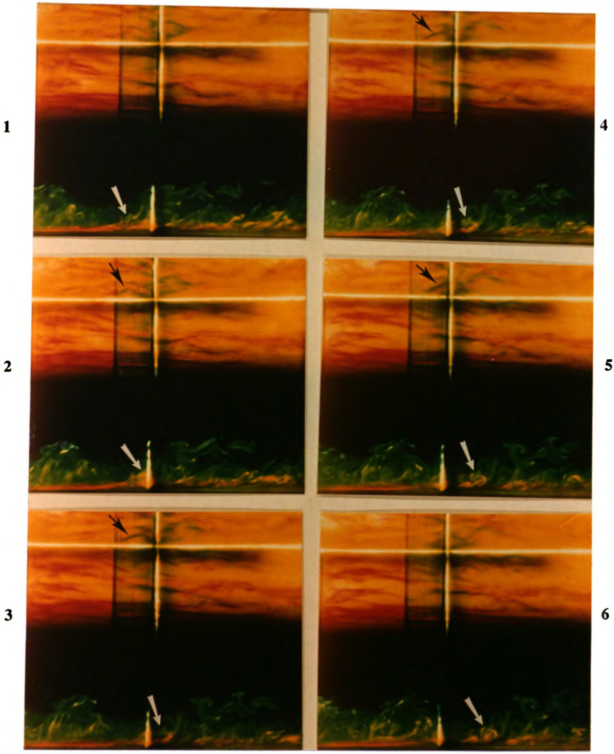

Figure 3.40 A sequence of simultaneous plan and side views illustrating the formation of a pocket by a typical eddy, as well as the subsequent interaction between the typical eddy and the lifted sublayer fluid near the downstream end of the pocket. Flow is from left to right. The evolution of the pocket is indicated by the black arrows, whereas the appearance of the typical eddy is indicated by the white arrow.

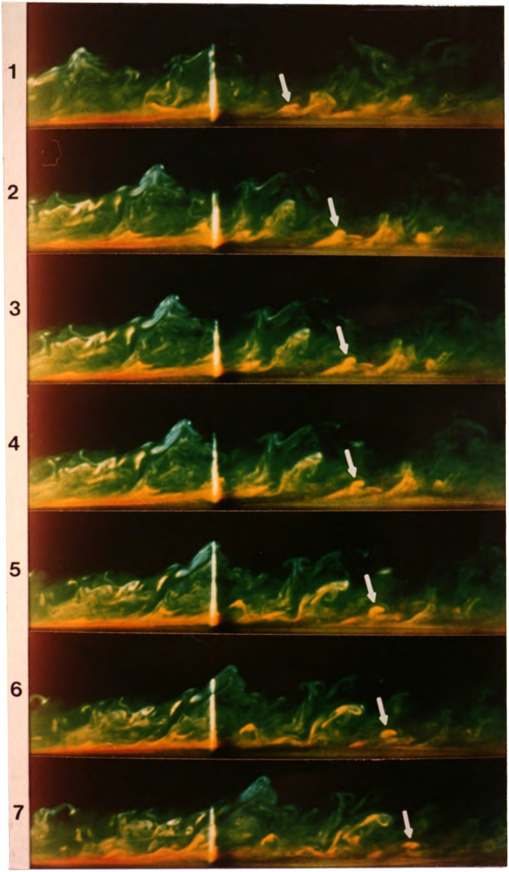

Figure 3.41 A sequential side-view pictures showing the formation of a new typical eddy from the pinch-off of a lifted hairpin (as indicated by the white arrows). The hairpin is called "primary hairpin" (see Chapter 1) which initially formed near the downstream end of the pocket in Figure 3.40. Flow is from left to right.

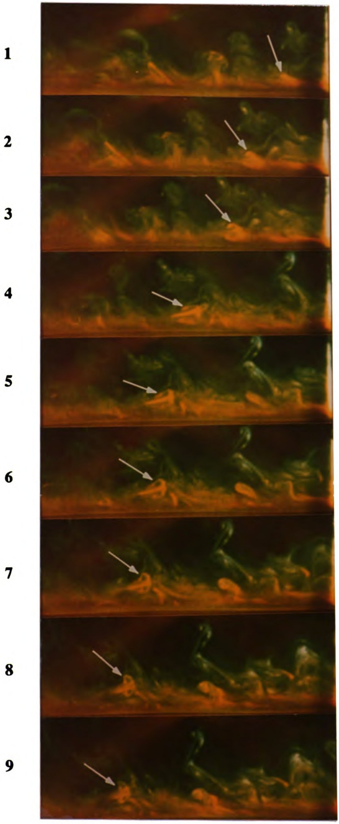

Figure 3.42 An example illustrating the evolution of a hairpin into a new typical eddy (as indicated by the white arrows). Flow is from right to left. Note that, in frames 5 to 9, an upstream typical eddy can also be seen to move into the streamwise laser sheet.

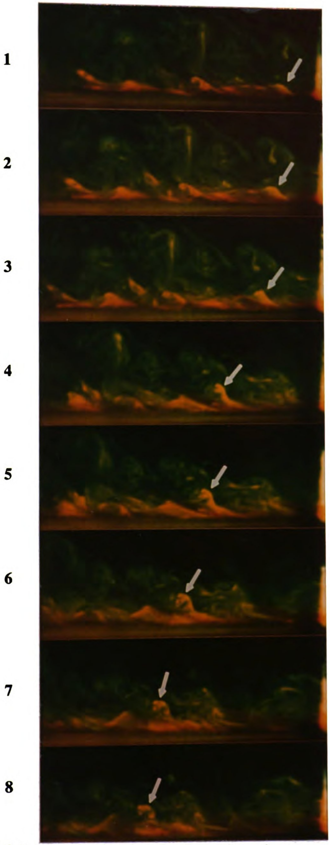

Figure 3.43 Another example showing the formation of a new typical eddy emerging from the wall layer fluid through a pinch-off of lifted hairpin (as indicated by the white arrows). Flow is from right to left.

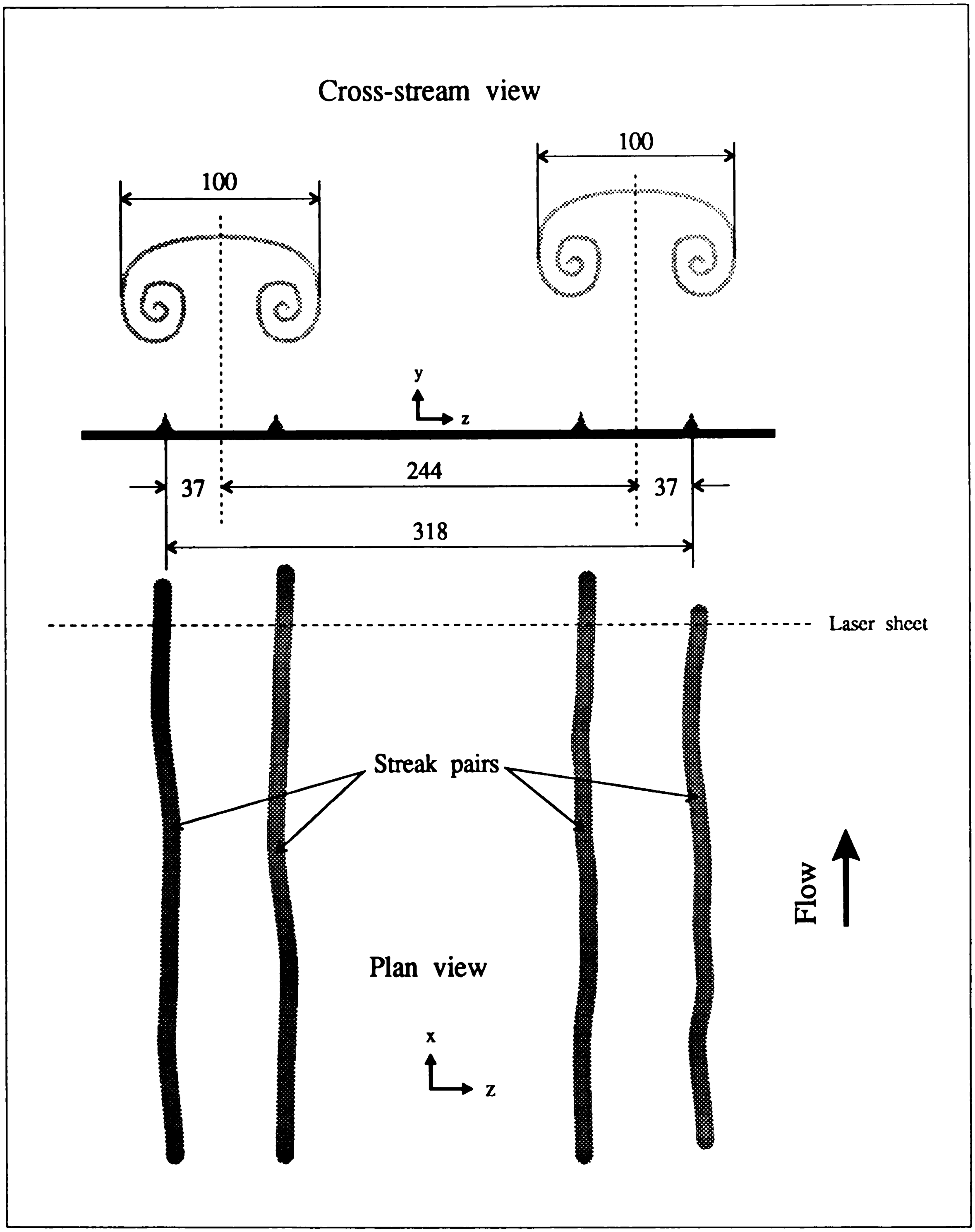

Figure 4.1 An illustration of plan and cross-stream views showing the spanwise phase relationship of typical eddies and the corresponding sublayer streak pairs. Mean value (in wall layer units) is used to represent each characteristic length.

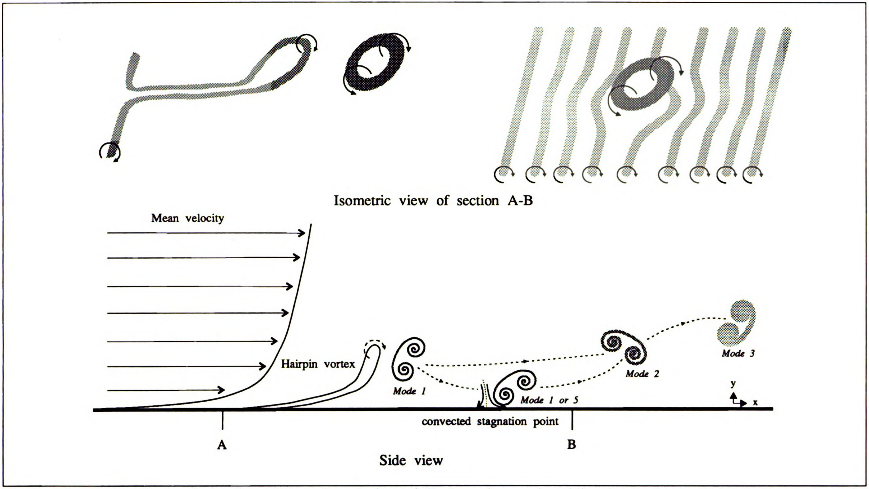

Figure 4.2 A hypothesis of the formation and evolution of Taylor micro-scale eddies in the log and the lower portion of the outer regions, suggesting that a typical eddy is created out of a lifted hairpin vortex through pinch-off mechanism. The subsequent evolution of the typical eddy is governed by the mean shear layer, instantaneous flow fileld of LSMs, and diffusion process. The isometric view shows the mechanism responsible for pocket formation is a stagnation point (for an observer moving with the speed of pocket center) created by a typical eddy in the vicinity of the wall (in side view, the streamwise distance between the stagnation point and typical eddy is exaggerated).

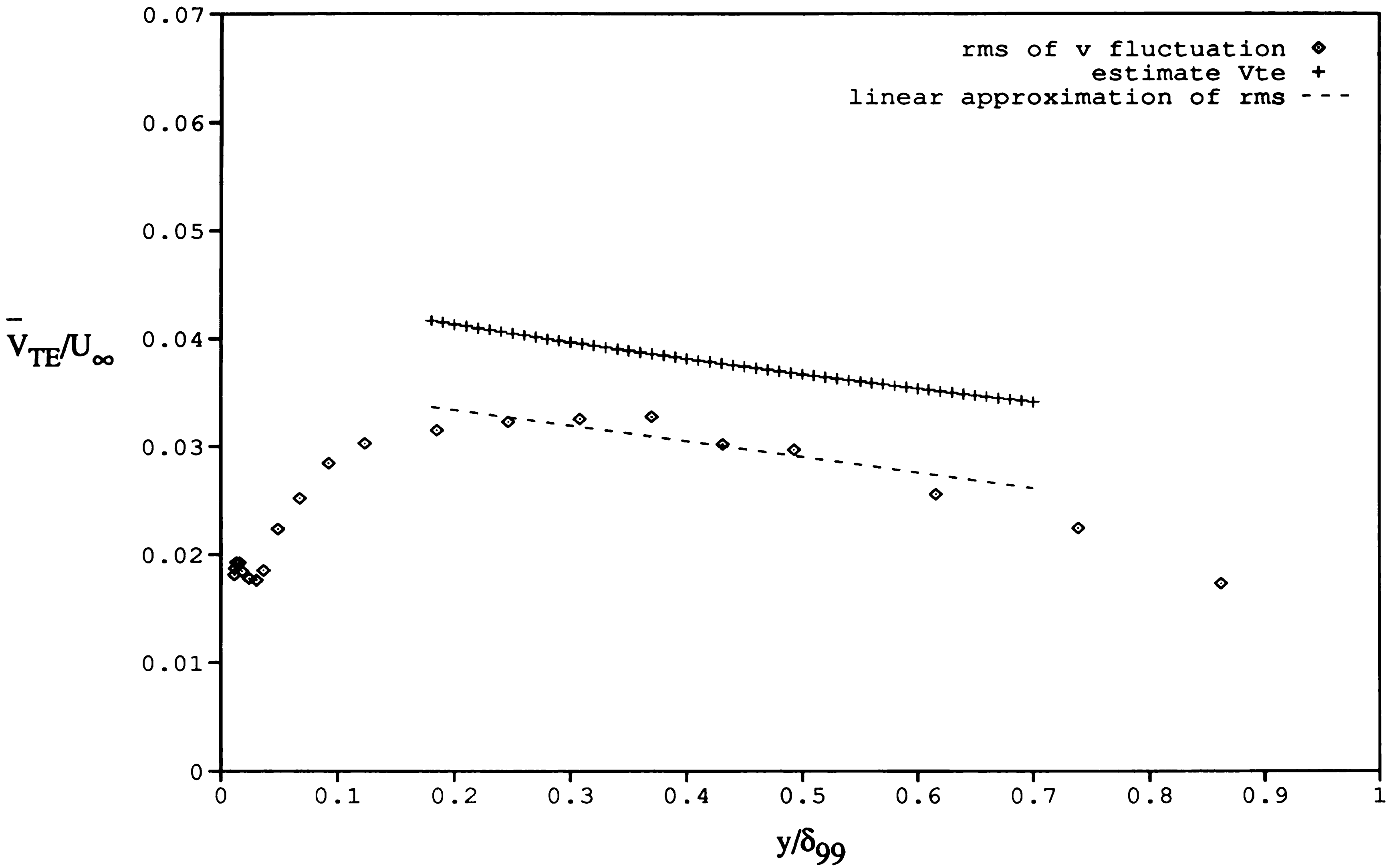

Figure 4.3 The estimate vertical convection velocity of typical eddies as a function of the distance from the wall. The *rms* of y-component velocity fluctuation at a comparable flow is also provided for comparison (see Klewicki 1989). The dashed line is an approximation of *rms* data in its maximum region.

APPENDICES

APPENDIX A : The Accuracy of the Pressure Measurements Based Upon the Free Stream Velocity

The data obtained using surface float technique are listed in Table A.1. The measurements for positions beyond δ_{99} using pressure probes are tabulated in Table A.2. They are shown as follows.

Table A.1 Measurements using surface floats at y=4.375 inches. The length scale (*s*) between two measuring stations is 4 feet.

Data #	Elapsed time (sec)
1	5.40
2	5.64
3	5.43
4	5.64
5	5.46
6	5.56
7	5.47
8	5.51
9	5.64
10	5.53
11	5.30
12	5.25
13	5.55
14	5.58
15	5.49
Average	5.497

Table A.2 Measurements using pressure probes for $y>\delta_{99}=1.85$ inches.

y (inch)	Velocity (ft/sec)
1.918	0.67141
2.097	0.69691
2.275	0.69498
2.632	0.69494
2.990	0.69691
3.347	0.70266
Average	0.693

The mean free stream velocity based on the float measurements can be found as

$$U_{\text{float}} = s/t_{\text{avg}} \cong 0.728 \text{ ft/sec} \qquad \text{(A1)}$$

The relative difference between the result of equation (A1) and the average value of Table A.2 is defined as follow (based upon the pressure measurements).

$$\text{Difference (\%)} = [(U_{\text{float}} - U_{\text{pressure}}) / U_{\text{pressure}}] \times 100\% \tag{A2}$$

which results in ~5.1% for the difference.

APPENDIX B : The Derivation of the Mean Vertical Velocity of Typical Eddies (v_{TE}) as a Function of the Distance from the Wall (d)

The function of the linearity between C_z and d, as well as the governing equation of the diffusion process of a vortex core are

$$C_z{}^+ = 88.6 + 0.1d^+, \quad \text{for } 55<y^+<280 \tag{B1}$$

$$r^2 = r_o{}^2 + 4\nu t \tag{B2}$$

,where r is equivalent to $C_z/2$, and r_o is the initial radius as typical eddy is formed. Equation (B1) can be rewritten in a dimensional form as

$$r = 0.0168 + 0.05d \tag{B3}$$

If we differentiate equations (B3) and (B2), they become

$$\Delta r = 0.05(\Delta d) \tag{B4}$$

$$2r(\Delta r) = 4\nu(\Delta t) \tag{B5}$$

Substituting Δr and r by equations (B4) and (B3) respectively, equation (B5) becomes

$$(0.00168 + 0.005d)(\Delta d) = 4\nu(\Delta t) \tag{B6}$$

By rearranging the equation, the relationship between v_{TE} and d is equated as follow.

$$v_{TE} = \Delta d/\Delta t = 4\nu/(0.00168 + 0.005d) = \nu/(0.00042 + 0.00125d) \tag{B7}$$

Now we can normalize v_{TE} and d using the free stream velocity, U_∞, and boundary layer thickness, δ_{99}, respectively. As a result, equation (B7) becomes

$$v_{TE}/U_\infty = [22.16 + 10.17(d/\delta_{99})]^{-1} \qquad \text{(B8)}$$

Note that the properties ν, U_∞, and δ_{99} of equation (B8) have been substituted by their nominal values at R_θ=805 (see Table 3.1). Equation (B8) can also be expanded into a binomial series as follow (see, for example, Abramowitz and Stegun 1964)

$$v_{TE}/U_\infty = 0.045/[1 + 0.459(d/\delta_{99})]^{-1} = 0.045(1 - X + X^2 - X^3 + X^4 - \ldots), \qquad X<1 \quad \text{(B9)}$$

,where $X = 0.459(d/\delta_{99})$. Note that function (B8) is shown in Figure 4.3.

APPENDIX C : Relative Uncertainty and Sensitivity of Mean Velocity Measurements

The mean velocity profile in the water tunnel was determined from pressure measurements and a formula derived from the Bernoulli equation as

$$\bar{u} = \sqrt{2gh} \qquad \text{(C1)}$$

where

u = velocity in feet per second

g = 32.2 feet per second, and

h = observed velocity head on the Pitot tube, in feet.

We recorded h by subtracting the static pressure from the total pressure. Since the ruler used to measure the pressure differential was 100 divisions per inch, the uncertainty (error bar) of h (i.e. Δh) can be estimated as ± 0.005 inches of H_2O. The central question is : "Given the Δh estimate, what is the resulting uncertainty in u?" For the answer, we recognize that equation (C1) can be differentiated as

$$\frac{d\bar{u}}{dh} = \sqrt{\frac{g}{2h}} \qquad \text{(C2)}$$

The derivative is also known as the sensitivity coefficient. In our setup, $h = l\sin\beta$, $\beta = 30$ degrees. We now can rewrite equation (C2) as

$$\frac{d\bar{u}}{dl} = \sqrt{\frac{g\mathrm{Sin}\beta}{2l}} \qquad \text{(C3)}$$

The sensitivity changed due to the rearrangement of the readout device is represented by the ratio, (C3)/(C2), as

$$\frac{\frac{d\bar{u}}{dl}}{\frac{d\bar{u}}{dh}} = \sqrt{\frac{h\text{Sin}\beta}{l}} = \text{Sin}\beta = \frac{1}{2} \tag{C4}$$

This means that the sensitivity was reduced by a factor of two.

To evaluate the relative uncertainty of u, we take the natural log on both sides of equation (C1) and differentiate them with respect to u and h. This results in an expression as follow.

$$\frac{d\bar{u}}{\bar{u}} = \frac{dh}{2h} \tag{C5}$$

The derivative is the relative uncertainty of u. Similarly, we can rewrite equation (C5) in terms of l as

$$\frac{d\bar{u}}{\bar{u}} = \frac{dl}{2l} \tag{C6}$$

By simple mathematical manipulations, it is found that the right hand sides of equations (C5) and (C6) are equal. This means that the relative uncertainty of u was unchanged by the rearrangement of the readout setup. The maximum and minimum of possible error for our measurements can be determined by either equation (C5) or (C6). The maximum error might occur at the measuring point closest to the wall as

$$\left(\frac{\Delta\bar{u}}{\bar{u}}\right)_{\max} \cong 0.5 \times \frac{\pm 0.005}{0.025} = \pm 0.1 = \pm 10\% \tag{C7}$$

Typically, the relative uncertainty is represented as an "I" bar, whose height is the representative of the numerical value of equation (C7). The minimum of relative uncertainty was possessed by the data measured beyond the boundary layer thickness, δ_{99}, as

$$\left(\frac{\Delta\bar{u}}{\bar{u}}\right)_{\min} \cong 0.5\times\frac{\pm0.005}{0.09} = \pm0.028 = \pm2.8\% \tag{C8}$$

APPENDIX D : The Probability Density Functions of Discrete Data

In the current study, the probability density functions representing the characteristics of events are formulated from discrete sample sets. Three probability densities are involved in our data analysis. They are the Normal (Gaussian), Logarithmic Normal, and the Rayleigh distributions, which are given as follows.

Normal Distribution :

$$P(r) = \frac{1}{\sqrt{2\pi}\sigma} \mathrm{Exp}\left[\frac{-(r-\bar{r})^2}{2\sigma^2}\right] \tag{D1}$$

where $\bar{r} = \frac{\sum_{i=1}^{N} r_i}{N}$ (i.e. mean value),

$$\sigma = \sqrt{\frac{\sum_{i=1}^{N}(r_i-\bar{r})^2}{N-1}} \text{ (i.e. standard deviation)}$$

In the above equation, P is the probability density, r is a random variable and N is the sample size.

Logarithmic Normal Distribution :

$$P(r) = \frac{1}{\sqrt{2\pi}\sigma r} \mathrm{Exp}\left\{\frac{-\left[\ln(r) - \overline{\ln(r)}\right]^2}{2\sigma^2}\right\}, \quad r>0 \tag{D2}$$

where $\overline{\ln(r)} = \dfrac{\sum_{i=1}^{N} \ln(r_i)}{N}$,

$$\sigma = \sqrt{\frac{\sum_{i=1}^{N}\left[\ln(r_i) - \overline{\ln(r)}\right]^2}{N-1}}$$

Rayleigh Distribution :

$$P(r) = \frac{r}{R}\mathrm{Exp}\left(\frac{-r^2}{2R}\right), \quad r>0 \qquad \text{(D3)}$$

where $\bar{r} = \dfrac{\sum_{i=1}^{N} r_i}{N}$,

$$R = \frac{2\bar{r}^2}{\pi}.$$

LIST OF REFERENCES

LIST OF REFERENCES

Abramowitz, M.; and Stegun, I. A. : Handbook of mathematical functions. 9th Edition, p. 15, 1970

Acarlar, M. S.; and Smith, C. R. : An experimental study of hairpin-type vortices as a potential flow structure of turbulent boundary layers. Report FM-5, Dept. of Mech. Engr./Mech., Lehigh University, 1984

Acarlar, M. S.; and Smith, C. R. : A study of hairpin vortices in a laminar boundary layer. Part 1. Hairpin vortices generated by a hemisphere protuberance. Journal of Fluid Mechanics, Vol. 175, pp. 1-41, 1987a

Acarlar, M. S.; and Smith, C. R. : A study of hairpin vortices in a laminar boundary layer. Part 2. Hairpin vortices generated by fluid injection. Journal of Fluid Mechanics, Vol. 175, pp. 43-83, 1987b

Aitchison, J.; and Brown, J. A. C. : The log-normal distribution. Cambridge University Press, 1957

Bakewell, H. P.; and Lumley, J. L. : Viscous sublayer and adjacent wall region in turbulent pipe flow. Physics of Fluids, Vol. 10, p.1880, 1967

Bessem, J. M.; Nieuwvelt, C.; Stouthart, J. C.; and Zeegers, J. C. H. : A turbulence wall layer visualization system using a dense fog and a scanning laser beam. Advance in Turbulence 2, pp. 244-250, 1989

Blackwelder, R. F.; and Kovasznay, L. S. G. : Large scale motion of a turbulent boundary layer with a zero and a favorable pressure gradient. Interim Technical Report, Dept. of Mechanics, The Johns Hopkins University, 1970

Blackwelder, R. F.; and Eckelmann, H. : Streamwise vortices associated with the bursting phenomenon. Journal of Fluid Mechanics, Vol. 94, p. 577, 1979

Brown, G. L.; and Rosko, A. : On density effects and large structures in turbulent mixing layers. Journal of Fluid Mechanics, Vol. 64, p. 775, 1974

Chu, C. C. : A study of turbulence production and modification in boundary layers using a new photochromic visualization technique. Ph.D Dissertation, Dept. of Mech. Engr., Michigan State University, 1987

Chu, C. C.; and Falco, R. E. : Vortex ring/viscous wall layer interaction model of the turbulence production process near walls. Experiments in Fluids, Vol. 6, pp. 305-315, 1988

Corino, E. R.; and Brodkey, R. S. : A visual investigation of the wall region in turbulent flow. Journal of Fluid Mechanics, Vol. 37, part 1, pp. 1-30, 1969

Eckelmann, H.; Nychas, S. G.; Brodkey, R. S.; and Wallace, J. M. : Vorticity and turbulence production in pattern recognized turbulent flow structures. Physics of Fluids, Vol. 20, Part II, pp. S225-S231, 1977

Falco, R. E. : Some comments on turbulent boundary layer structure inferred from the movements of a passive contaminant, AIAA paper, No. 74-99, 1974

Falco, R. E. : Coherent motions in the outer region of turbulent boundary layers. Physics of Fluids, Vol. 20, No. 10, Part II, pp. S124-S132, 1977

Falco, R. E. : The role of outer flow coherent motions in the production of turbulence near a wall. "Coherent structure of turbulent boundary layers", an AFOSR/Lehigh University Workshop, ed. by C. R. Smith and D. E. Abbott, pp. 448-461, 1978a

Falco, R. E. : Wall layer structure of turbulent boundary layers. Bulletin Am. Physical Society, Series II, Vol. 23, p. 1000, 1978b

Falco, R. E. : Structural aspects of turbulence in boundary layer flows. "Turbulence in Liquids", ed. by G. K. Patterson and J. L. Zakin, pp. 1-14, 1979

Falco, R. E. : The production of turbulence near a wall. AIAA paper, No. 80-1356, 1980

Falco, R. E. : A synthesis and model of wall region turbulence structure. The structure of turbulence, heat and mass transfer. ed. Zoric, Z., pp. 124-135, Washington: Hemisphere, 1982

Falco, R. E.; and Signor, D. B. : Evidence for the existence of vortex rings vs. hairpin eddies in turbulent boundary layers. Bull. Am. Phys. Society, Series II, Vol. 27, p. 1203, 1982

Falco, R. E. : New results, a review and synthesis of the mechanism of turbulence production in boundary layer and its modification. AIAA paper, No. 83-0377, 1983

Falco, R. E.; and Rashidnia, N. : What happens to the large eddies when net drag reduction is achieved by outer flow manipulators? In Proc. Inter. Conf. on turbulent Drag Reduction by Passive Means, Royal Aero Society, London, England, Sept. 15-17, 1987

Falco, R. E. : Correlation of outer and passive wall region manipulation with boundary layer coherent structure dynamics and suggestions for improved devices. AIAA paper, No. 89-1026, 1989

Falco, R. E.; Klewicki, J. C.; and Pan, K. : Production of turbulence in boundary layers and potential for modification of the near wall region. IUTAM Symposium on Structure of Turbulence and Drag Reduction, ed. by A. Gyr, ETH Zurich, 1989a

Falco, R. E.; Klewicki, J. C.; Pan, K.; and Gendrich, C. P. : Production of turbulence in boundary layers. 7th Symposium on Turbulent Shear Flows at Stanford University, Aug. 21-23, 1989b

Falco, R. E. : A coherent structure model of the turbulent boundary layer and its ability to predict Reynolds number dependence. Philosophical Transactions of the Royal Society of London, series A, Vol. 336, pp. 103-129, 1991

Head, M. R.; and Bandyopadhyay, P. : New aspects of turbulent boundary-layer structure. Journal of Fluid Mechanics, Vol. 107, pp. 297-338, 1981

Hoyez-Delaliaux, M. C. : Etude des caracteristiques instationnaires d'une couche limite turbulente de plaque plane sans gradient de pression. Ph.D Dissertation of Mech. Engr., University of Sciences and Techniques at Lille Flandres-Artois, France, 1990

Jiménez, J.; Moin, P.; Moser, R.; and Keefe, L. : Ejection Mechanisms in the sublayer of a turbulent channel. Physics of Fluids, Vol. 31, p. 1311, 1988

Kim, H. T.; Kline, S. J.; and Reynolds, W. C. : The production of turbulence near a smooth wall in a turbulent boundary layer. Journal of Fluid Mechanics, Vol. 50, part 1, pp. 133-160, 1971

Kim, J. : Investigation of turbulent shear flows by numerical simulations. 10th Congress of Applied Mechanics, Austin TX, 1986

Kim, J.; Moin, P.; and Moser, R. : Turbulence statistics in fully developed channel flow at low Reynolds number. Journal of Fluid Mechanics, Vol. 177, pp. 133-166, 1987

Klewicki, J. C. : On the interactions between the inner and outer region motions in turbulent boundary layers. Ph.D Dissertation, Dept. of Mech. Engr., Michigan State University, 1989

Klewicki, J. C.; Gendrich, C. P.; Foss, J. F.; and Falco, R. E. : On the sign of the instantaneous spanwise vorticity component in the near-wall region of turbulent boundary layers. Phys. Fluids A, Vol. 2, No. 8, pp. 1497-1500, 1990

Kline, S. J.; Reynolds, W. C.; Schraub, F. A.; and Runstadler, P. W. : The structure of turbulent boundary layers. Journal of Fluid Mechanics, Vol. 30, pp. 741-774, 1967

Kline, S. J. : Quasi-coherent structures in the turbulent boundary layer. Part I, Zoran P. Zaric Memorial International Seminar on Near-Wall Turbulence at Dubrovnik, Yugoslavia, 16-20 May, 1988

Kovasnay, L. S. G.; Kibens, V.; and Blackwelder, R. F. : Large-scale motion in the intermittent region of a turbulent boundary layer. Journal of Fluid Mechanics, Vol. 41, pp. 283-387, 1970

Laufer, J. : The structure of turbulence in fully developed pipe flow. NACA report 1174, 1954

Laufer, J. : New trends in experimental turbulence research. Annual Review of Fluid Mechanics, ed. by M. Van Dyke, W. G. Vincenti, and J. V. Wehausen, Vol. 7, pp. 307-326, 1975

Lee, M. K.; Eckelman, L. D.; and Hanratty, T. J. : Identification of turbulent wall eddies through the phase relation of the components of the fluctuating velocity gradient. Journal of Fluid Mechanics, Vol. 66, p. 17, 1974

Lemay, J.; Delville, J.; and Bonnet, J. P. : Turbulent kinetic energy balance in a LEBU modified turbulent boundary layer. Proc. 11th Symposium on Turbulence, Missouri-Rolla, pp. 7-1 to 7-8, 1988

Liang, S.; Falco, R. E.; and Bartholomew, R. W. : Vortex ring/moving wall interactions : experiments and numerical modelling. Bull. Am. Phys. Soc. Series II, Vol. 28, p. 1397, 1983

Lovett, J. A. : The flow fields responsible for the generation of turbulence near the wall in turbulent shear flows. M.S. thesis, Dept. of Mech. Engr., Michigan State University, 1982

Lu, L. J.; and Smith, C. R. : Report FM-14, Dept. of Mech. Engr. and Mech., Lehigh University, Bethlehem, PA., 1988

Moin, P.; Kim, J.; and Choi, H. : On the active control of wall-bounded turbulent flows. AIAA paper, No. 89-0960, 1989

Moin, P.; Leonard, A.; and Kim, J. : Evolution of a curved vortex filament into a vortex ring. Physics of Fluids, Vol. 29, pp. 955-963, 1986

Moser, R. D.; and Moin, P. : Direct numerical simulation of curved turbulent channel flow. Rep. TF-20, Dept. of Mech. Engr., Stanford University, 1984

Nishino, K.; Kasagi, N.; and Hirata, M. : Study of streamwise vortical structures in a two-dimensional turbulent channel flow by digital image processing. 2nd International Symposium on Transport Phenomena in Turbulent Flows, ed. by M. Hirata and N. Kasagi, pp. 157-170, Oct. 1987

Nychas, S. G.; Hershey, H. C.; and Brodkey, R. S. : A visual study of turbulent shear flow. Journal of Fluid Mechanics, Vol. 61, pp. 513-525, 1973

Offen, G. R.; and Kline, S. J. : Combined dye-streak and hydrogen-bubble visual observations of a turbulent boundary layer. Journal of Fluid Mechanics, Vol. 62, part 2, pp. 223-239, 1974

Offen, G. R.; and Kline, S. J. : A proposed model of the bursting process in turbulent boundary layers. Journal of Fluid Mechanics, Vol. 70, pp. 209-228, 1975

Oldaker, D. K.; and Tiederman, W. G. : Spatial structure of the viscous sublayer in drag reducing channel flow. Physics of Fluids, Vol. 20, pp. S133-S144, 1977

Praturi, A. K.; and Brodkey, R. S. : A stereoscopic visual study of coherent structure in turbulent shear flow. Journal of Fluid Mechanics, Vol. 89, pp. 251-272, 1978

Robinson, S. K.; Kline, S. J.; and Spalart, P. R. : A review of quasi-coherent structures in a numerically simulated turbulent boundary layer. NASA TM 102191, 1989

Smith, C. R. : Application of high speed videography for study of complex, three-dimensional water flows. SPIE 348, High Speed Photography (San Diego), pp. 345-352, 1982

Smith, C. R.; and Metzler, S. P. : The characteristics of low-speed streaks in the near-wall region of a turbulent boundary layer. Journal of Fluid Mechanics, Vol. 129, p. 27, 1983

Spalart, P. R. : Numerical simulations of boundary layers. NASA TM 88220-88222, 1985

Stanislas, M.; and Hoyez, M. C. : Analysis of the structure of a turbulent boundary layer, with and without a "LEBU" using light sheet smoke visualization and hot wire measurements. Structure of Turbulence and Drag Reduction, ed. by A. Gyr, Springer-Verlag, pp. 507-515, 1990

Townsend, A. A. : The structure of turbulent shear flows. Cambridge University Press, Cambridge, U. K. 2nd edition, 1976

Van Dyke, M. : An album of fluid motion. The Parabolic Press, p. 65, 1982

Walsh, M. J. : Turbulent boundary layer drag reduction using riblets. AIAA paper, No. 82-0161, 1982

White, F. M. : Fluid Mechanics. 2nd edition, McGraw-Hill, pp. 398-409, 1986

Wilkinson, S. P.; and Balasubramanian, R. : Turbulent burst control through phase-locked travelling surface depressions. AIAA paper, No. 85-0536, 1985

Willmarth, W. W.; and Tu, B. J. : Structure of turbulence in the boundary layer near the wall. Physics of Fluids, Supplement to Vol. 10, pp. S134-S137, 1967

Yoda, H. : Effects of dilute polymer additives on the turbulence structure near a wall. M.S. thesis, Dept. of Mech. Engr., Michigan State University, 1981

Yoo, S. C. : Turbulence drag reduction by wall modification. M.S. report (unpublished), Dept. of Mech. Engr., Michigan State University, 1990

Zang, T. A.; Krist, S. E.; and Hussaini, M. Y. : Resolution requirements for numerical simulations of transition. J. Sci. Computing, Vol. 4, pp. 197-217, 1989

Zang, T. A. : Numerical simulation of the dynamics of turbulent boundary layers : perspectives of a transition simulator. Philosophical Transactions of the Royal Society of London, series A, Vol. 336, pp. 95-102, 1991